國立台灣大學電機資訊學院電子工程研究所

博士論文

Graduate Institute of Electronics Engineering

College of Electrical Engineering and Computer Science

National Taiwan University

Doctoral Dissertation

鍺/矽化學氣相沉積磊晶異質成長與參雜

Heteroepitaxy Ge/Si and Dopant Incorporation by Chemical Vapor Deposition

杜文仙

Wen-Hsien Tu

指導教授: 劉致為 博士

Advisor: Chee Wee Liu, Ph.D.

中華民國 103 年 7 月

July, 2014

國立臺灣大學博士學位論文
口試委員會審定書

鍺/矽化學氣相沉積異質磊晶成長與參雜

Heteroepitaxy Ge/Si and Dopant Incorporation by Chemical Vapor Deposition

本論文係杜文仙君（D98943020）在國立臺灣大學電子工程學研究所完成之博士學位論文，於民國 103 年 07 月 05 日承下列考試委員審查通過及口試及格，特此證明

口試委員：

（指導教授）

系主任、所長

Heteroepitaxy Ge/Si and Dopant Incorporation by Chemical Vapor Deposition

By

Wen-Hsien Tu

Dissertation

Submitted in partial fulfillment of the requirement
for the degree of Doctor of Philosophy
in Electronics Engineering
at National Taiwan University
Taipei, Taiwan, R.O.C.

July 2014

Approved by：

Advised by：

Approved by Director：

致謝

由衷感謝我的指導教授 劉致為 教授給我這個成長機會，使我能踏入磊晶這一塊領域，更在研究上指導我嚴謹認真的態度，以及謙卑學習態度。並給予我許多機會讓我能與同學或在國家奈米實驗室的傑出的研究員合作的機會，使我能在求學過程中做人處事各方面更加成熟。我更要感謝任職於在國家奈米實驗室的羅廣禮博士以及許舒涵博士在實驗上的意見以及鼓勵。更感謝研究室裡的博士班學長以及同學，包括李承翰、藍偟翔、 林政明、何偉碩、許文瑋、張弘志、陳彥瑜、陳彥廷、陳藏龍、黃仕賢、翁翊軒、黃智雄、顏智洋、陳品翔，給予我在求學生涯中有淚有像美好的回憶，如果沒有大家的支持與幫助我很難度過這博士班嚴峻的考驗。更要感謝阿肥(陳彥廷)，博士博(陳彥瑜)以及阿賢(黃仕賢)一直給我打氣，一同去華盛頓、柏克萊以及新加坡的時光是博士班中難得的經驗。除此之外在研究或在行政上給我許多幫助的學弟及助理們，包括秦曉麗小姐、李淑珍小姐、陳鈺升、謝岱澄、白君彥、陳慶麒、黃偉倫、黃奕中、林子堯、賴德全。此外我更要感激一直為我禱告的台北基督徒禮拜堂以及福音會永和教會青年團契的弟兄姊妹為我禱告，謝謝大家在我最低潮的時間陪伴我安慰我並用 神的話給我支持使我真相信”你的日子如何，你的力量也必如何。”也感謝我的口試委員包括，台積電王錦坤處長、楊育佳處長、潘正聖處長、清大洪銘輝教授、張廖貴術教授、交大林鴻志教授以及台大李峻霣教授給予我論文寶貴的意見。

最後我要感謝永遠愛我的爸爸、媽媽、哥哥、大嫂、蜜思還有我的丈夫-李道。博士班雖然辛苦，但因你們用無私的愛幫助我使我能堅持走完這旅程，我會用一輩子的人生愛你們回饋你們。

杜文仙 2014/07/25

Publication List

A: Journal Paper (學術期刊論文)

1. **Wen-Hsien Tu,** Shu-Han Hsu, and C. W. Liu, "The PN Junctions of Epitaxial Germanium on Silicon by Solid Phase Doping" accepted by IEEE Trans. Electron Device, 2014.

2. **Wen-Hsien Tu,** C.-H. Lee, H. T. Chang, B.-H. Lin, C.-H. Hsu, S. W. Lee, and C. W. Liu, "A transition of three to two dimensional Si growth on Ge (100) substrate," J. Appl. Phy.s, Vol. 112, 126101, 2012.

3. **Wen-Hsien Tu,** S.-H. Huang, and C.W. Liu, "Ge out diffusion effect on SiGe nanoring formation," J. Appl. Phys, Vol. 111, 076103, 2012.

B: Conference Paper (國際研討會論文)

1. I-Hsieh Wong, Yen-Ting Chen, Shih-Hsien Huang, **Wen-Hsien Tu**, Chih-Hsiung Huang, Yu-Sheng Chen, Chun-Liu Chu, Shu-Han Hsu and C. W. Liu, "High Performance Junctionless In-situ Doped Ge Gate-all-around PFETs on Si" International Semiconductor Device Research Symposium, 2013.

2. C. W. Liu, Hung-Chih Chang, Yen-Ting Chen, **Wen-Hsien Tu**, I-Hsieh Wong, Shu-Han Hsu, and Chun-Lin Chu, "3D Ge transistors," IEEE Nanotechnology Materials and Devices Conference (IEEE-NMDC), Tainan, Taiwan, Oct. 2013.

3. Shu-Han Hsu, Hung-Chih Chang, Chun-Lin Chu, Yen-Ting Chen, **Wen-Hsien Tu,** Fu Ju Hou, Chih Hung Lo, Po-Jung Sung, Bo-Yuan Chen, Guo-Wei Huang, Guang-Li Luo, C. W. Liu, Chenming Hu, and Fu-Liang Yang, "Triangular-channel Ge NFETs on Si with (111) Sidewall-Enhanced Ion and Nearly Defect-free Channels," p.525-528, International Electron Devices Meeting (IEDM), 2012.

4. **Wen-Hsien Tu,** S.-H. Huang, and C. W. Liu, "SiGe Nanoring Formation," 6th International SiGe Technology and Device Meeting (ISTDM), Berkeley, California, June 4-6, 2012.

5. Shu-Han Hsu, Chun-Lin Chu, **Wen-Hsien Tu,** Yen-Chun Fu, Po-Jung Sung, Hung-Chih Chang, Yen-Ting Chen, Li-Yaw Cho, Guang-Li Luo, William Hsu, C. W. Liu, Chenming Hu, and Fu-Liang Yang, Chenming Hu, and Fu-Liang Yang, " Nearly Defect-free Ge Gate-All-Around FETs on Si Substrates," International

Electron Devices Meeting (IEDM), 2011.

6. **Wen.-Hsien Tu,** C.-H Lee, and C.W.Liu, "Strained GeSi Layer Grown on (110) Silicon-On-Insulator" 7th International Conference on Silicon Epitaxy and Heterostructures (ICSI-7), Leuven, Belgium, August 28th -Sweptemper 1th, 2011.

7. C. -H. Lee, **Wen-Hsien Tu,** C. M. Lin, H. T. Chang, S. W. Lee, and C. W. Liu, "Surface Orientation Effects on SiGe Quantum Dots and Nanorings Formation" 218th Meeting of Electrochemical Society, Las Vegas, Nevada, Oct. 10-15, 2010.

C. Conference paper (國內研討會論文)

1. **Wen-Hsien Tu**, and C. W. Liu, "A Transition of Three to Two Dimensional Si Growth on Ge (100) substrate," *20th Symposium on Nano Device Technology (SNDT),* Mat 1-2, Hsinchu, Taiwan, 2013.

摘要

為因應尺寸不斷的縮小的互補式金氧半電晶體元件，鍺製程除了有與當前矽製程兼容的優勢外，鍺通道更具有比 III-V 族高的電洞遷移率。此外藉由成長矽鍺的汲極和源極使通道產生應變可用以提高鍺通道的電子和電洞遷移率，使鍺同時具有高電子以及電洞遷移率，故藉由產業界所使用的化學氣相沉積系統，來成長高品質的矽鍺及鍺材料在未來的互補式金氧半電晶體元件是必要的。

於本論文的第一部份，藉由鍺原子從被覆蓋的矽鍺量子點外擴散的現象來形成矽鍺量子環的生長機制將被再次討論，研究發現在不同的載流氣體環境之下會影響此種矽鍺量子環的生長。當氫原子較少覆蓋矽鍺量子點導致較多的矽成長覆蓋在量子點上，此覆蓋會阻礙鍺原子經由外擴散形成矽鍺量子環結構。除此之外，為了想在鍺基板型成此奈米微結構，我們討論了在鍺基板上成長矽的生長機制。一個與一般在矽基板上生長鍺狀況不同，從三維生長回歸到二維生長的機制，被第一次在鍺基板上成長矽的情形中發現。首先，矽量子點會先出現在鍺基板表面。在持續的矽沉積後，整個矽表面將會變平，會由原先的三維生長回歸到二維生長當中。我們發現由於在矽量子點的濕層的表面鍺濃度較高處會有較快的成長速率，而矽量子點的頂端表面鍺濃度較低有較慢的成長速率，最後導致原先三維生長形成的量子點最後變平回歸的二維生長的模式當中。

由於之前我們發現載流氣體以及鍺濃度會影響矽鍺生長模式，故本論文的第二部份會探討利用矽甲烷或二氯矽烷加鍺甲烷，在不同載流氣體以及不同鍺濃度之下，來研究影響矽鍺薄膜或甚至鍺薄膜成長速率以及光激發光特性的因素。研究結果發現:第一、提高矽鍺薄膜中鍺濃度確實會提高其成長速率。第二、在氮氣

的環境中，鍺薄膜的成長速率以及利用矽甲烷和鍺甲烷形成的矽鍺薄膜成長速率增加，但若利用二氯甲矽烷及鍺甲烷形程矽鍺薄膜的成長速率卻會降低。成長速率增加原因在於較高的鍺濃度以及在充滿氮氣的環境中會使得薄膜表面氫氣較少，有利於矽或鍺原子的吸附來提高成長速率。但對於利用二氯矽烷形程矽鍺薄膜時，由於二氯矽烷不易脫附阻礙矽或鍺原子的吸附使得成長速率降低。

為了應用在汲極和源極對通道產生應變的技術或成長高濃度的無接面電晶體元件通道，在此外本論文最後研究有關鍺參雜的技術，藉由形成一高硼參雜或磷參雜的固態層，其參雜藉由擴散在鍺內形成淺接面。此技術避免因離子佈值型成的缺陷而造成的暫態擴散提升效應，此部分一開始會利用固態參雜擴散技術來形成接面，此技術為形成一高硼或磷濃度的固態層做為形成鍺參雜的來源，證實由於沒有因離子佈值型成的缺陷，此技術所製成的二極體具有較低的漏電流。但由參雜在鍺的固態溶解度很低，加上在活化時會因快速擴散而降低濃度，不利於型成鍺的淺接面，所以本研究利用在氣相沉積鍺薄膜時的直接參雜的技術來形成高濃度的參雜鍺，並利用不同的後續熱製成來活化，研究結果得到利用氣相沉積直接參雜加直接加熱技術可以得到 $3x10^{20}$ cm^{-3} 的 p 型參雜鍺，利用氣相沉積直接參雜加雷射活化技術所可以得到 $2x10^{20}$ cm^{-3} 的 n 型參雜鍺。

關鍵字： 化學氣象沉積/ 奈米環狀結構 / 應變 /三維生長回歸到二維生長/ 載氣效應/矽鍺成長速率/三維生長回歸到二維生長 /固態參雜 /直接參雜/雷射活化

Abstract

To scale down the CMOS devices in the future, Ge not only the compatible with current Si industry, but also the higher carrier mobility than Si channel. For hole mobility, Ge has the highest hole mobility even compared with group III-V materials. Using the SiGe stressor at source and drain, which is called strain technology, the Ge channel can have both higher electron and hole mobility. Base on its wide use of future CMOS device in the future industry, it is needed to grow high quality SiGe or even Ge material using chemical vapor deposition (CVD) system.

In the first part of this thesis, the SiGe nanoring formation mechanism by Ge out-diffusion from the capped SiGe dot in the ultra-high vacuum CVD (UHV/CVD) is discussed. It is found that the formation of SiGe nanoring can be affected in different carrier gas environment. Less H passivation on the SiGe dot can result more Si cover on the top of dot and retard the Ge out-diffusion to form the nanoring. To grow the nanoring structures on the Ge substrate, the growth mechanism of the Si on Ge growth is studied. The transition from 3-dimensional (3D) to 2-dimensional (2D) growth for Si on Ge, which is different from the Ge on Si case, was observed for the first time. The Si quantum dots can be observed in the initial Si growth on Ge. With the increasing Si deposition, the surface can be flatten without any nanostructures above. At the wetting layer of SiGe dot, more Ge coverage on the surface leads to higher growth rate than the peak of the dot. This different Si growth rate at the SiGe dots region leads to the growth transition from 3D to 2D of Si growth on Ge.

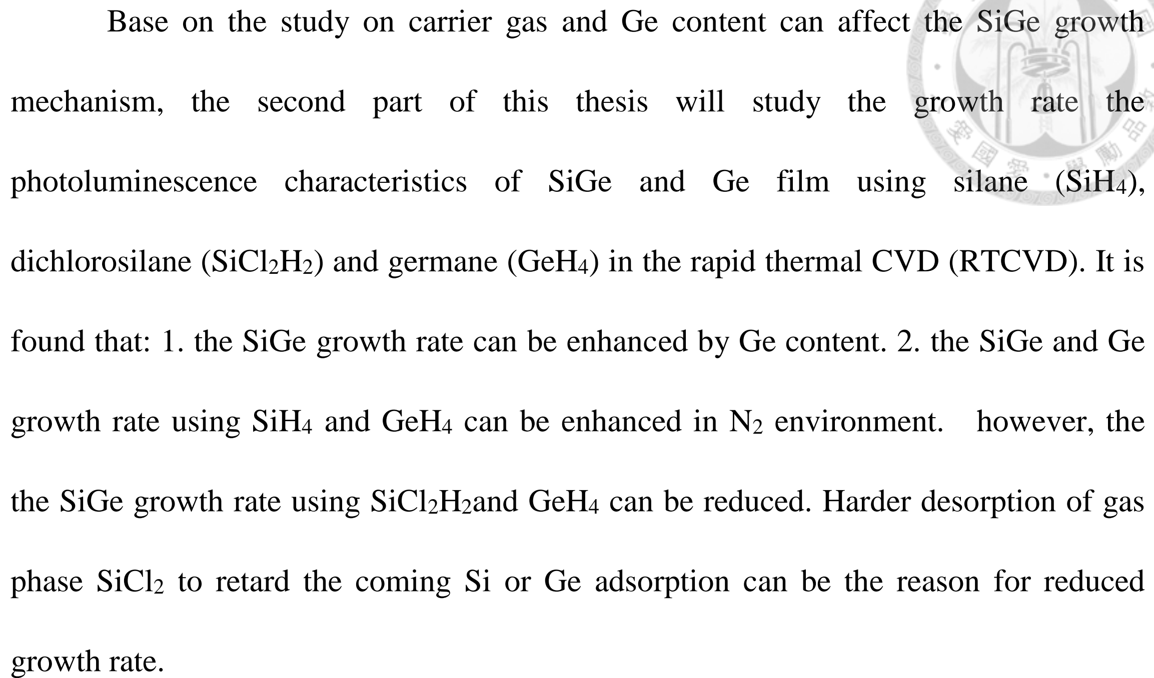

Base on the study on carrier gas and Ge content can affect the SiGe growth mechanism, the second part of this thesis will study the growth rate the photoluminescence characteristics of SiGe and Ge film using silane (SiH_4), dichlorosilane ($SiCl_2H_2$) and germane (GeH_4) in the rapid thermal CVD (RTCVD). It is found that: 1. the SiGe growth rate can be enhanced by Ge content. 2. the SiGe and Ge growth rate using SiH_4 and GeH_4 can be enhanced in N_2 environment. however, the the SiGe growth rate using $SiCl_2H_2$and GeH_4 can be reduced. Harder desorption of gas phase $SiCl_2$ to retard the coming Si or Ge adsorption can be the reason for reduced growth rate.

For the application of source/drain stressor or the channel of junction less device, the doping technology of Ge is studied in the third part in this thesis. The first technology is the solid phase doping for shallow junction. The solid layers, which have high boron or phosphorous dopants, can diffusion to Ge for shallow junctions. Due to the ion implantation damage free, the diodes doped by solid phase doping have low leakage. However, the dopant solid solubility in Ge is low and diffusion is high during the following activation. So the *in situ* doping by CVD with different post activation is used to grow high doped Ge. The $3x10^{20}$ cm^{-3} p-type Ge can be reach directly by *in situ* doping and *in situ* H_2 anneal. Due to the fast phosphorous diffusion, the rapid thermal anneal (RTA) and laser anneal are used to activate n-type dopant. The $2x10^{20}$ cm^{-3} n-type Ge can be reach directly by *in situ* doping and laser anneal.

Keywords: chemical vapor deposition, nanoring, strain, 3D to 2D growth, carrier gas effects, SiGe growth rate, solid phase doping, *in- situ* doping, laser annealing.

Contents

致謝 III

Publication List.......... IV

摘要.......... VI

Abstract.......... VIII

Contents X

List of Figures.......... XIV

List of Tables.......... XXIII

Chapter 1 Introduction 1

1.1 Motivation.......... 1

1.2 Unaxis UHV/CVD and ASM Epsilon RTCVD 2

1.3 Channel Material Engineering 4

1.4 Source/Drain Engineering 7

1.5 Dissertation Organization 9

Reference.......... 12

Chapter 2 Growth and Control of SiGe Nanoring Formation.......... 15

2.1 Introduction.......... 15

2.2 Experiments 16

2.3 Carrier Gas Effects on Si Cap for Nanoring Formation 17

2.4 Carrier Gas Effects on Annealing for Nanoring Formation..........................31

2.5 Summary 35

Reference 36

Chapter 3 A Transition from Three to Two Dimensional Si Growth on Ge(001) Substrate 38

3.1 Introduction..38

3.2 Experiments 39

3.3 Transition from 3D to 2D Si Growth on Ge(001) 42

3.4 Growth Model of Si growth on Ge(001) 45

3.5 Summary 54

Reference 55

Chapter 4 Growth Rate of SiGe and Ge on Si(001) 58

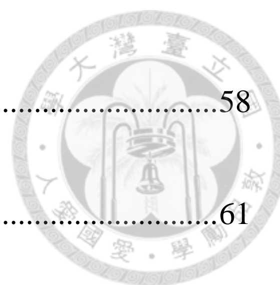

4.1 Growth model by Chemical Vapor Deposition 58

4.2 SiGe on Si(001) Growth and Chracteristics 61

4.3 Carrier Gas Effects on SiGe Growth Rate on Si(001) 69

4.4 Ge Growth on Si(001) 71

4.5 Summary 77

Reference 78

Chapter 5 Solid Phase Doping Ge by Chemical Vapor Depostion 81

5.1 Introduction 81

5.2 Experiments 82

5.3 Boron and Phosphorous layer doping of Ge by Chemical Vapor Deposition. 84

5.4 P^+N or N^+P Ge Diodes by Solid Phase Layer Doping 88

5.5 Summary 91

Reference 93

Chapter 6 *In-situ* Doped Ge by Chemical Vapor Deposition 98

6.1 Introduction..98

6.2 Experiments..99

6.3 *In-situ* Boron doped Ge by Chemical Vapor Deposition. 100

6.4 *In-situ* Phosphorous doped Ge by Chemical Vapor Deposition. 103

6.5 Laser Annealing of *In-situ* Phosphorous doped Ge 108

6.6 Summary..116

Reference…………………………………………………………………...117

Chapter 7 Summary and Future Work 120

7.1 Summary..120

7.2 Future Work..122

List Of Figures

Fig.1-1 The schematics of UHV/CVD 2

Fig.1-2 The schematics of ASM Epsilon 2000 RTCVD 3

Fig.1-3 (a) Drain current characteristics of the SiGe QW device and bulk Si device. (b) The hole mobility of SiGe QW device and bulk Si device from the split C-V 5

Fig.1-4 Substrate orientation effects on electron mobility in our planar devices compared to Si universal mobility. The peak mobility on Ge(111) is about 2200 cm^2/V.s at RT, which is 2 times enhancement compared to that of Ge(100). 6

Fig.1-5 A TEM image of the 500nm $Si_{0.5}Ge_{0.5}$ on $Si_{1-x}Ge_x$ relaxed buffer layer. Note that the strain is gradually relax by the relaxed buffer layer to make $Si_{0.5}Ge_{0.5}$ be defect free 6

Fig.1-6 TEMs of the PMOS channel in the S/D region showing the SiGe epitaxy in the S/D region. 7

Fig.1-7 TEM images of $Si_{0.6}Ge_{0.4}$ layer grown on FinFET structures defined on (100) Si: (a) fin oriented along <110> direction, (b) fin oriented along <100> 8

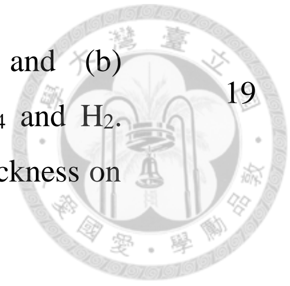

Fig.2-1 (a) High resolution cross-sectional TEM images and (b) HAADF-TEM images of the uncapped QD using SiH_4 and H_2. Note that the QDs is only partially capped and the Si thickness on wetting layer is only ~5nm. 19

Fig.2-2 (a) High resolution cross-sectional TEM images and (b) HAADF-TEM images of the capped QD using SiH_4 and He. Note that the QDs is totally capped and the Si thickness on wetting layer is ~7nm which is thicker than its using SiH_4 and H_2. 20

Fig.2-3 (a) The AFM images (5 μm x 5 μm) of (a) nanorings transformed from uncapped QDs after 1h *in situ* vacuum annealing at 500°C and. (b) The schematics of corresponding growth model of nanoring formation transformed from uncapped QDs. Note H passivation can prevent Si growth on top of the QD and enhance the Ge outdiffusion for nanoring formation 21

Fig.2-4 (a) The AFM images (5 μm x 5 μm) of (a) capped QDs after 1 h *in situ* annealing in vacuum at 500°C and (b) The schematics of corresponding growth model for no nanoring formed from capped QDs. Note that Si can be grown on top of QD with no H passivation and retard Ge out-diffusion to form nanorings 22

Fig.2-5 (a) The 3D AFM images of uncapped QDs. (b) The 3D AFM images of uncapped QDs after 1 h annealing in vacuum at 500°C to form nanoring. Note that the width of nanoring is larger than QDs due to Ge out-diffusion. 23

Fig.2-6 The high resolution TEM images and corresponding EDS measurement of nanorings. 24

Fig.2-7 The nanoring density as a function of *in situ* annealing time in vacuum for uncapped QDs. 26

Fig.2-8 The nanoring density as a function of *in situ* annealing time in vacuum for capped QDs. The inset images are the corresponding AFM images of nanorings from capped QDs. 26

Fig.2-9 Ge–Ge LO phonon wave number positions for capped and uncapped QDs. 28

Fig.2-10 Ge–Ge LO phonon wave number positions as a function of *in situ* annealing time in vacuum for uncapped QDs. Note the larger wave number shift positively as soon as the nanorings formed 29

Fig.2-11 Ge–Ge LO phonon wave number positions as a function of *in situ* annealing time in vacuum for capped QDs. Note the larger wave number of capped QDs and the positive shift as soon as the nanorings formed 30

Fig.2-12 The AFM images (5 μm x 5 μm) of capped QDs with *in situ* anneal at 500°C in vacuum, in He ambient and in H2 ambient. 31

Fig.2-13 The AFM images (5 μm x 5 μm) of uncapped QDs with at in situ anneal 500°C in vacuum, in He ambient and in H_2 ambient. Note no nanoring can be formed with *in situ* anneal in H_2 even from uncapped QDs. 32

Fig.2-14 The models for annealing effects on nanoring formation. Even for the uncapped QDs, the nanoring cannot be formed with H_2 annealing by H passivation 33

Fig.2-15 Raman spectra as a function of *in situ* annealing time in H2 for uncapped QDs 34

Fig.3-1 The AFM images (5μm × 5μm) of Si QDs grown on Ge substrate. Two types Si QDs (indicated by white dash circles) can be observed. 41

Fig.3-2	The 3D AFM images and line profile of the type-I and type-II Si QDs shown in Fig.3-1.	41
Fig.3-3	The cross-sectional TEM image of a Si dot with the wetting layer of ~5 nm and the dot height of ~3 nm.	42
Fig.3-4	The cross-sectional TEM image of the ~11 nm Si on Ge. Note the dislocation appears to relax strain.	44
Fig.3-5	The AFM image of the ~11 nm Si film with ring-like structures on the surface.	44
Fig.3-6	The 3D AFM images and line profile of the ring-like structure. The average width and depth is ~129.4 nm and ~1nm, respectively.	45
Fig.3-7	The AFM SiGe pyramid images on (a) Si(001) (b) Si(110), and (c) Si(111).	47
Fig.3-8	The EDS measurement for a Si dot on Ge.	48
Fig.3-9	The growth model of Ge segregation effects of Si grown on Ge. Higher growth rate due to the more open sites on the wetting layer than on the dot leads to the smooth surface.	49
Fig.3-10	The cross-sectional TEM images of ~15 nm Si grown on Ge and Ge content by EDS measurement.	50
Fig.3-11	The AFM image of the ~15 nm Si grown on Ge. Note the surface roughness (~0.26 nm) is similar to bulk Ge.	51
Fig.3-12	The Si-Si Raman spectroscopy of Si dots, 11 nm and 15 nm Si film grown on Ge.	52
Fig.3-13	The (400) XRD in-plane radial scans of Si dots and 15 nm Si on Ge. Note the tensile strain is almost relaxed for 15 nm Si on Ge.	53

Fig.4-1 The side view of silane adsorption reaction on a (2 x 1) reconstructed silicon surface. The dashed triangle underneath the silicon surface represents the reconstruction of the surface silicon atoms in/out of the plane of the figure 59

Fig.4-2 Top view of the adsorption process of silane onto a Si:H (100) (2x1) reconstructed surface based on references [1],[3]. Red circles indicate the change, and a red line indicates an open surface site. 60

Fig.4-3 The rocking curve XRD of SiGe on Si(001). Note the Ge content is 27% under the fully strain fitting. 64

Fig.4-4 The PL spectrum of SiGe on Si with EHP fitting. The bandgap extracted from the cut-off of NP peak is 907meV. (b) The bandgap of fully strained and relaxed Ge_xSi_{1-x} on Si (001) and the Ge% of our SiGe is 28%. Note the Ge% is determined from the extracted bandgap of 907meV from (a). 64

Fig.4-5 (a) The high resolution TEM of Si(7.4nm)/$Si_{0.73}Ge_{0.27}$ (24.8nm)/Si buffer on Si(001). No dislocation is found. (b) From the STEM images, abrupt interface shows no interdiffusion between SiGe and Si. 65

Fig.4-6 The AFM image of Si/$Si_{0.73}Ge_{0.27}$/Si. The RMS roughness is only 0.1nm, which is close to substrate surface. Note that no cross-hatch is found on surface. 66

Fig.4-7 (a) The XRD and (b) the PL spectrum of SiGe on Si. Note the Ge% extraction from both XRD and PL is close to 50%. 67

Fig.4-8 The AFM image of Si/$Si_{0.5}Ge_{0.5}$/Si. The RMS roughness is only 0.21nm. Note that no cross-hatch is found on surface. 67

Fig.4-9 The high resolution TEM of Si(5nm)/$Si_{0.5}Ge_{0.5}$ (17nm)/Si buffer 68

on Si(001). No dislocation is found and interface is abrupt.

Fig.4-10 The SiGe growth rate of $Si_{1-x}Ge_x$ with 0.27<x<0.5. Note the SiGe growth rate increases with increasing Ge content. 68

Fig.4-11 The PL spectra of SiGe using DCS/GeH_4 or SiH4/GeH_4. Note higher Ge content and stronger SiGe PL can have by DCS/GeH_4 69

Fig.4-12 (a) The SiGe growth rate using SiH_4/GeH_4 and DCS/GeH_4 with H_2 and N_2 as carrier gas composition (b) The Ge content using SiH_4/GeH_4 and DCS/GeH_4 with H_2 and N_2 as carrier gas composition. 71

Fig.4-13 The high resolution TEM of 4.1mm Ge on Si(001). The inset is the Nomarski micrograph of Ge with Shimmel etching for etching pits observation 74

Fig.4-14 The XRD of 4.1 mm Ge on Si(001). Note the 0.16% tensile strain in Ge film. 74

Fig.4-15 The PL spectra of the bulk Ge and epitaxial Ge on Si at room temperature. The integrated PL intensity ratios of the direct to indirect band gap transition of the bulk n-Ge and Ge-on-Si sample are 0.05 and 2.5, respectively. The bulk Ge is ~15 times the integrated intensity of PL of the epitaxial Ge sample. 75

Fig.4-16 (a) The Ge growth rate using GeH_4/H_2 and GeH_4/N_2 as composition. Growth rate can be 3 times enhanced using GeH_4/N_2 and (b) smoother surface with surface RMS roughness of 2nm. 76

Fig.5-1 The TEM cross-sectional images of epitaxial Ge (a) as grown and (b) after anneal. Note the threading dislocation density in Ge film with post annealing is ~$5x10^8$ cm-2. 84

Fig.5-2 The TEM cross-sectional images of (a) a ~5nm boron layer and (b) less than monolayer phosphorous layer on epitaxial Ge growth at 85

450°C for 2 hrs.

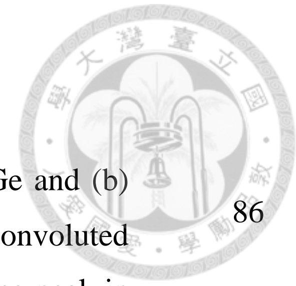

Fig.5-3 X-ray photoelectron spectra of (a) the boron layer on Ge and (b) the phosphorous layer on Ge. The peak in (a) can be deconvoluted into B-B peak (186.5eV) and (B-Ge) peak (187.6eV). The peak in (b) can be deconvoluted into P-P peak (130.3eV), P-Ge peak (129.2eV), and Ge 3p (126eV). 86

Fig.5-4 The SIMS profiles of (a) boron dopants in Ge and (b) phosphorous dopants in Ge. 87

Fig.5-5 (a) Current density vs. voltage (J–V) characteristics of p^+/n Ge diodes by *in situ* boron layer at the room temperature. The on/off ratio is about ~$1x10^5$, ideality factor is about 1.1, and the reverse saturation current is ~$1x10^{-4}A/cm^2$. (b) The Arrhenius plot of the reverse saturation currents with the J-V curves at different temperatures in the inset. 89

Fig.5-6 (a) J–V characteristics of n^+/p Ge diodes by *in situ* phosphorous layer at the room temperature. The on/off ratio is ~$1.5x10^5$, ideality factor is about 1.2, and the reverse saturation current is $4x10^{-5}A/cm^2$. (b) The Arrhenius plot of the reverse saturation currents with the J-V curves at different temperatures in the inset. 90

Fig.6-1 (a)SIMS of in situ boron doped Ge with and without 825°C post H_2 annealing, and (b) SIMS depth profile comparing with SRP and hole concentration at ~$5x10^{18}cm^{-3}$ by van der pawu measurment of *in situ* boron doped Ge with 825°C post H_2 annealing. 100

Fig.6-2 (a) The cross-sectional TEM images of 105nm *in situ* boron doped Ge. Defect region within ~40nm defect region near the Ge/Si interface causes low activation region in Fig.6-1(b). (b) The misfit dislocation defects found at Ge/Si interface. 101

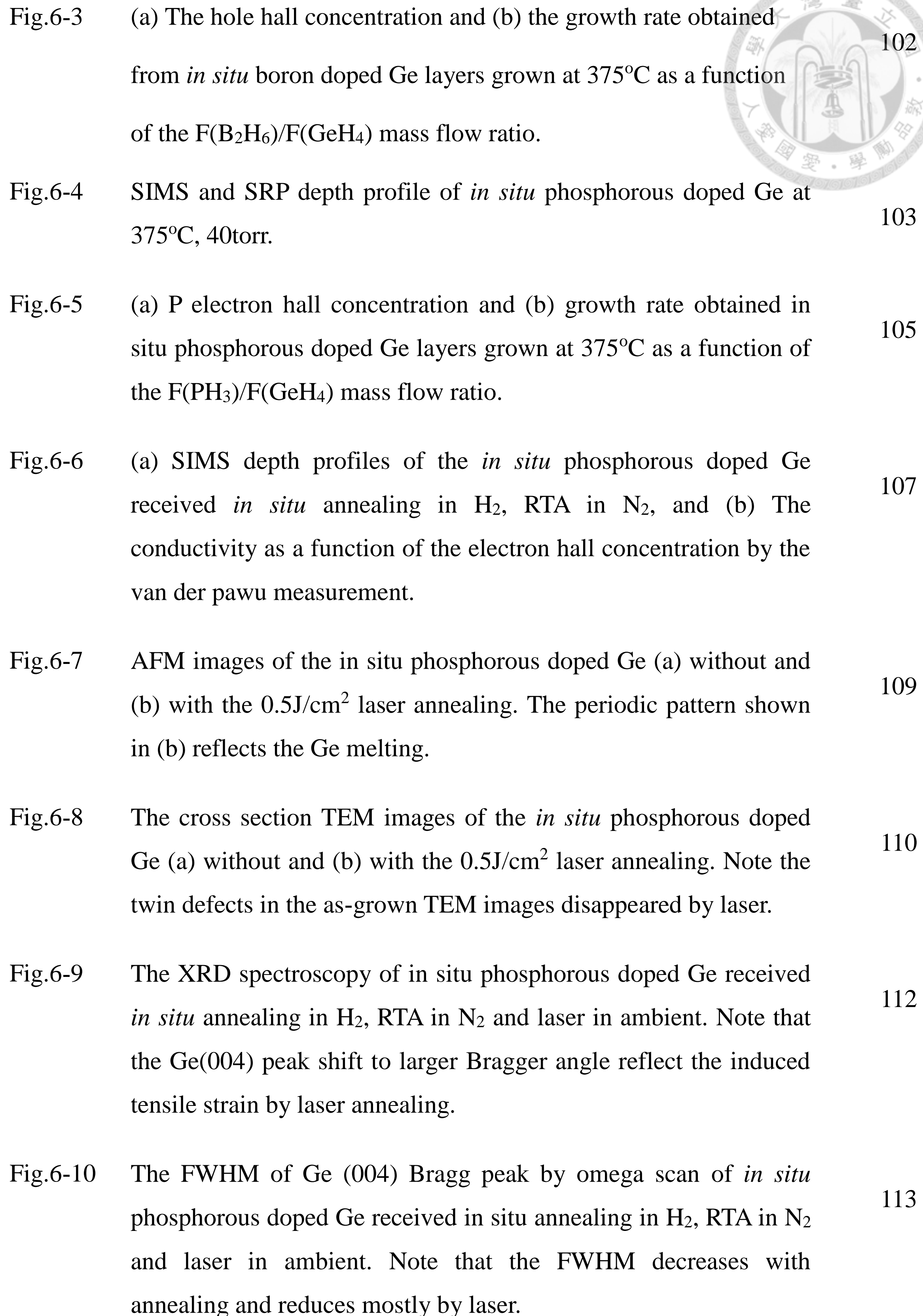

Fig.6-3 (a) The hole hall concentration and (b) the growth rate obtained from *in situ* boron doped Ge layers grown at 375°C as a function of the $F(B_2H_6)/F(GeH_4)$ mass flow ratio. 102

Fig.6-4 SIMS and SRP depth profile of *in situ* phosphorous doped Ge at 375°C, 40torr. 103

Fig.6-5 (a) P electron hall concentration and (b) growth rate obtained in situ phosphorous doped Ge layers grown at 375°C as a function of the $F(PH_3)/F(GeH_4)$ mass flow ratio. 105

Fig.6-6 (a) SIMS depth profiles of the *in situ* phosphorous doped Ge received *in situ* annealing in H_2, RTA in N_2, and (b) The conductivity as a function of the electron hall concentration by the van der pawu measurement. 107

Fig.6-7 AFM images of the in situ phosphorous doped Ge (a) without and (b) with the 0.5J/cm^2 laser annealing. The periodic pattern shown in (b) reflects the Ge melting. 109

Fig.6-8 The cross section TEM images of the *in situ* phosphorous doped Ge (a) without and (b) with the 0.5J/cm^2 laser annealing. Note the twin defects in the as-grown TEM images disappeared by laser. 110

Fig.6-9 The XRD spectroscopy of in situ phosphorous doped Ge received *in situ* annealing in H_2, RTA in N_2 and laser in ambient. Note that the Ge(004) peak shift to larger Bragger angle reflect the induced tensile strain by laser annealing. 112

Fig.6-10 The FWHM of Ge (004) Bragg peak by omega scan of *in situ* phosphorous doped Ge received in situ annealing in H_2, RTA in N_2 and laser in ambient. Note that the FWHM decreases with annealing and reduces mostly by laser. 113

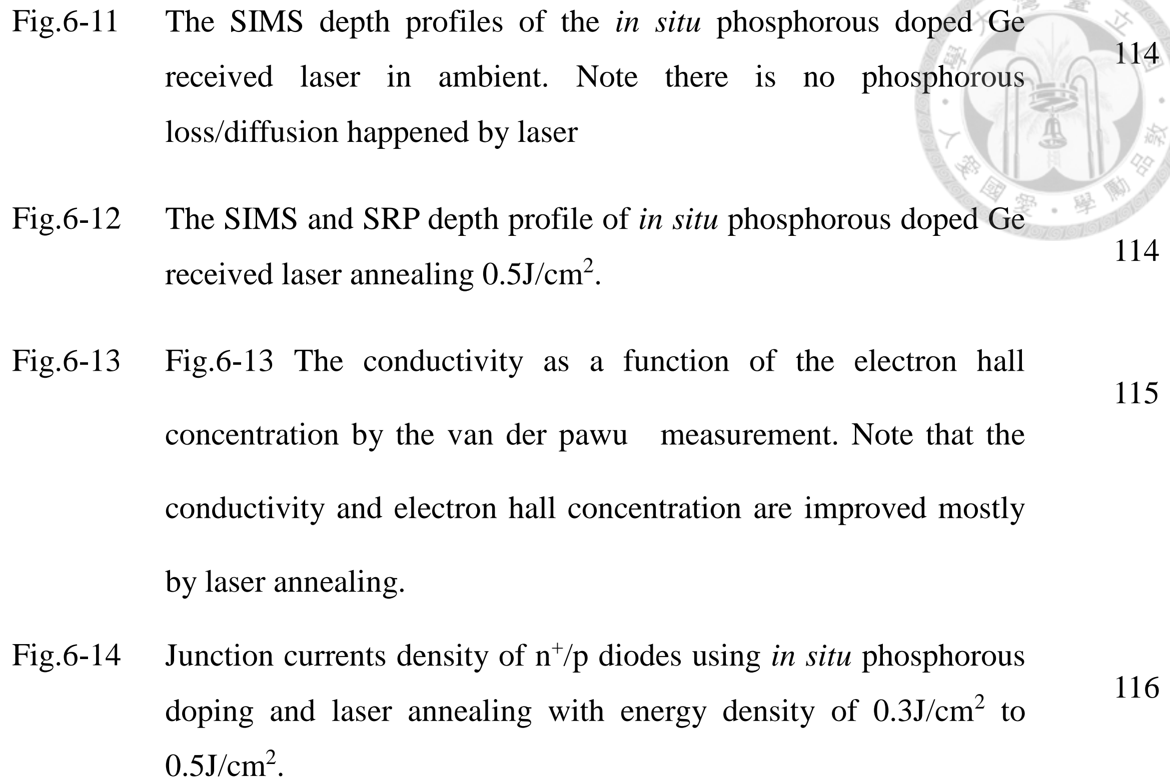

Fig.6-11 The SIMS depth profiles of the *in situ* phosphorous doped Ge received laser in ambient. Note there is no phosphorous loss/diffusion happened by laser 114

Fig.6-12 The SIMS and SRP depth profile of *in situ* phosphorous doped Ge received laser annealing 0.5J/cm^2. 114

Fig.6-13 Fig.6-13 The conductivity as a function of the electron hall concentration by the van der pawu measurement. Note that the conductivity and electron hall concentration are improved mostly by laser annealing. 115

Fig.6-14 Junction currents density of n$^+$/p diodes using *in situ* phosphorous doping and laser annealing with energy density of 0.3J/cm^2 to 0.5J/cm^2. 116

List of Tables

Table 2-1	The summary conditional for nanoraing formation at 500°C	35
Table 5-1	Comparison of the p^{+}/n Ge diodes by *in situ* boron layer doping and other methods from precious works. Our diodes shows superior on/off ratio and I_{off}.	91
Table 5-2.	Comparison of the n^{+}/p Ge diodes by *in situ* phosphorous layer doping and other methods from precious works. Our diodes shows superior I_{off} .	92

Chapter 1
Introduction

1.1 Motivation

There were 10^9 transistors in a CPU such as Intel Core i7 [1]. Following the Moore's law, several critical issues such as gate leakage, junction leakage, low transconductance, interconnect capacitance, and subthreshold conduction [2] must be solved. In 2011, the 22 nm node FinFETs is released [3], the 30 nm L_g of FinFETs is used for the 22nm node, but other dimensional shrinking of the FinFETs is the fin width of top gate at only ~8nm. With reduction of these dimensions, the performance limitation of Si channel will appear gradually even with strain technology, and the incorporation of new channel materials is emerging as an important way to continue the device performance even when facing the physical limitation of device scaling. The high mobility gives high source injection velocity into the quasi-ballistic transport channel of the advanced devices [4, 5]. For large devices, the mobility itself has more impact on the drive current [6]. To great success in the future Complementary Metal-Oxide-Semiconductor devices with, growing high quality of SiGe or Ge material by chemical vapor deposition epitaxy has been attracting much attention in the application of future electrical areas.

1.2 Unaxis UHV/CVD and ASM Epsilon RTCVD

The Unaxis ultra-high vacuum chemical vapor deposition (UHV/CVD) is used to observe the atomic behavior when growing SiGe nanostructures. In contrast to the reduced pressure (RP) or atmosphere pressure (AP) CVD, the residual gas pressure is well controlled to ensure low levels of contamination in the UHV/CVD

Base on the theory of Ghiddini and Smith [7], in order to conduct epitaxy at temperatures significantly lower than 700ºC, one must maintain the partial pressure of H_2O at ultra-high vacuum levels. A similar requirement can be found in the case of oxygen [8]. The ultra-high vacuum system can provide a "window" for the low temperature Si/Ge/SiGe epitaxial growth with oxide-free Si surface. Due to the ability to have clean surface at low temperature, the atomistic behavior, like surface diffusion, can be observed in the UHV/CVD (Fig.1-1). The system includes a hot-wall quartz reaction chamber. The hot-wall system can prevent the process environment from the out-gasing of the chamber wall. The background impurity can be reduced, and the film quality would thus be improved. Duro dry pump is used to reduce the base pressure at $\sim 10^{-9}$ torr and 10^{-3} torr at process.

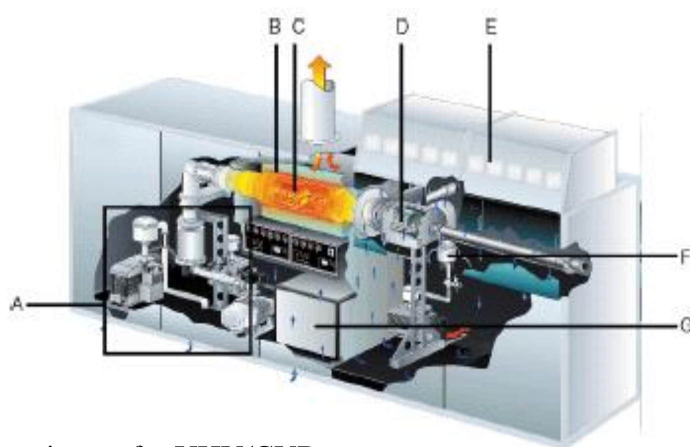

Fig.1-1 The schematics of UHV/CVD

However. the low growth rate restricts the development of the UHV/CVD is the industry. ASM Epsilon 2000 rapid thermal CVD (RTCVD) in Fig.1-2 is used to develop the SiGe or Ge films for device application in this thesis. The chamber is quarts tube mounted to a steel chamber in cold-wall system and heated by tungsten halogen lamp. The chamber is pumped with a two-stage rotary vane pump. The temperature control is conducted by quartz-sheet thermocouple. A separated load-lock with gate valve is used to minimize the undesirable introduction of unwanted moisture or contamination into the chamber when transferring wafers. Purifier for H_2, N_2 and HCl to make the contamination or vapor less than 100ppt are used separately for clean surface and high quality epitaxial film.

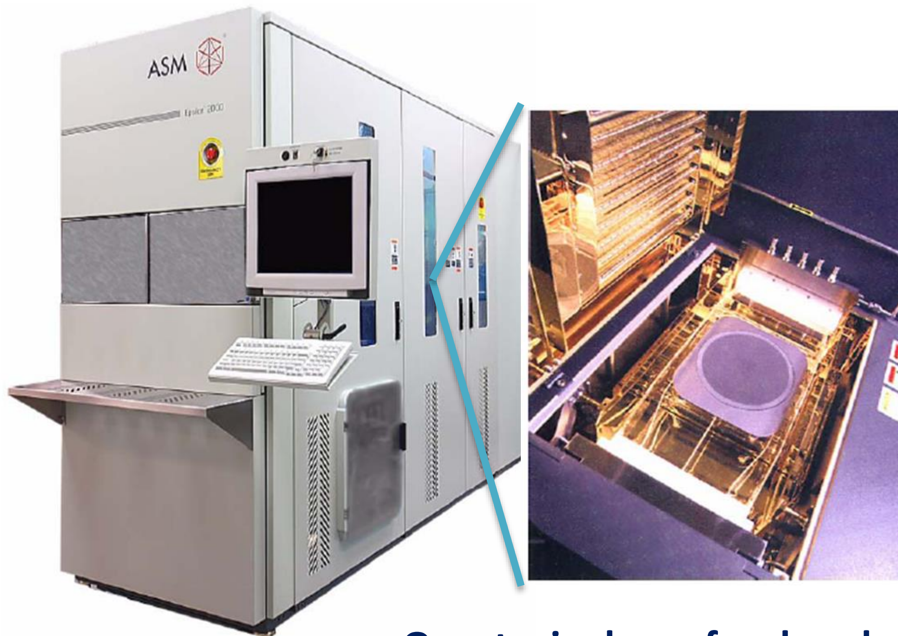

Fig.1-2 The schematics of ASM Epsilon 2000 RTCVD

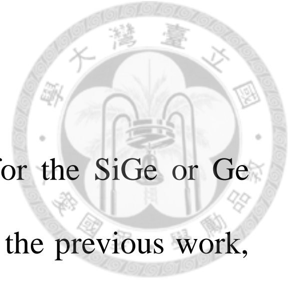

1.3 Channel Material Engineering

The channel material engineering is one of most applications for the SiGe or Ge epitaxial growth. The SiGe channel pMOSFET was investigated in the previous work, and the enhancement of the hole mobility and the driven current are at least 3 times to the bulk Si device, as shown in Fig. 1-3 [9]. Due to the highest hole mobility of Ge among group III-V and IV materials [10]. The Ge pMOSFETs with high hole mobility and high drive current have already been reported [11, 12]. The Ge (111) nMOSFETs with record high electron mobility (2200 cm2/V s) exceeding Si universal mobility proved in 2012 [13], as shown in Fig. 1-4. However, the high cost of Ge wafers limits the application of Ge MOSFET in CMOS technology. The high quality, defect free of SiGe or Ge epitaxial growth directly on Si substrate has drawn lots of attention in the last decade.

However, the heteroepitaxy of Ge and SiGe on Si have the fundamental limit from the high lattice mismatch (up to 4.2%) between Si and Ge. Therefore, the misfit dislocation network at interface to relax strain is needed for SiGe or Ge growth on Si. These dislocation can degraded the crystalline quality and consequently compensate the electron and hole mobility advantage expected from the SiGe or Ge channel. One of conventional solution is to grown a gradually but eventually fully relaxed $Si_{1-x}Ge_x$ (x ramps from 0 to 1) buffer layer on the Si substrate, serving as the so-called virtual substrate. In the Fig. 1-5, the defect free $Si_{0.5}Ge_{0.5}$ can be grown on the virtual substrate, which is graded buffer layer with $Si_{1-x}Ge_x$ ($0<x<0.5$). In order to reduce the density of threading dislocations, these technologies typically require the thick growth (typically > 1 μm) to gradually ramps up Ge fraction to relax strain, is not appreciated in practical industry applications. Therefore, it is highly interested and demanded if one can have

some innovative ideas to produce thinner and dislocation-free virtual substrate layers, or even direct growth of high quality Ge structures on Si. Several approaches proposed in the represent project proposal are thus attempts to find a practical solution to make defect-free Ge layer growth for heterogeneous integration of high mobility channel.

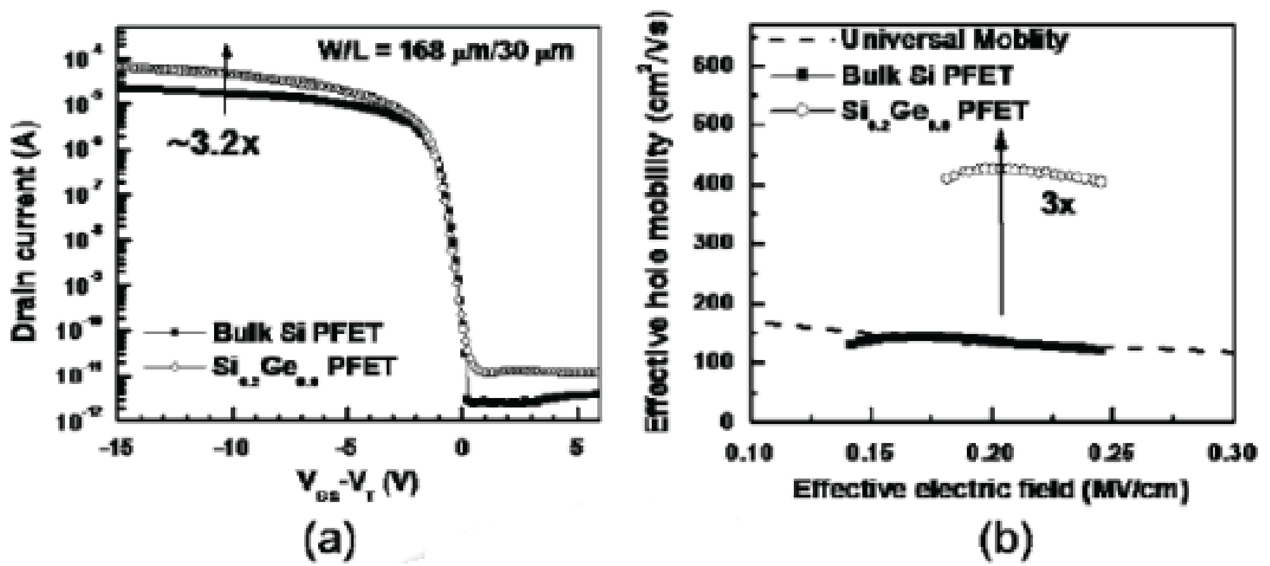

Fig.1-3 (a) Drain current characteristics of the SiGe QW device and bulk Si device. (b) The hole mobility of SiGe QW device and bulk Si device from the split C-V measurement [9].

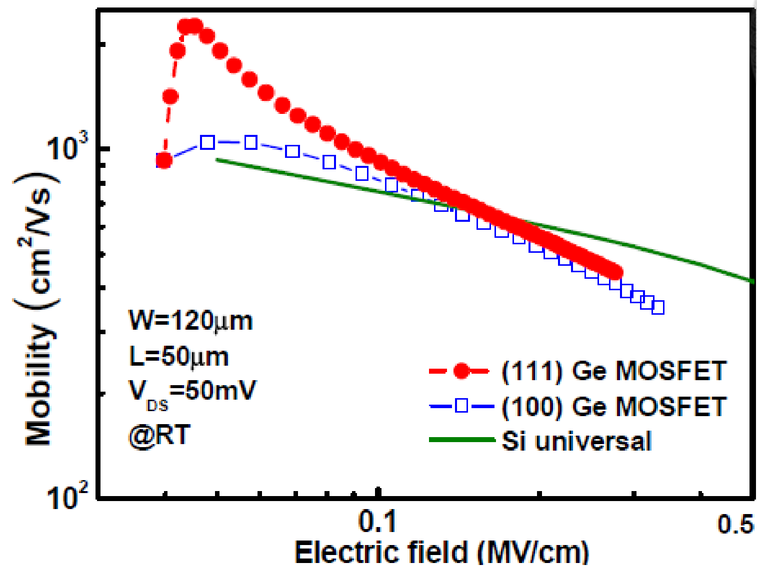

Fig.1-4 Substrate orientation effects on electron mobility in our planar devices compared to Si universal mobility. The peak mobility on Ge(111) is about 2200 $cm^2/V.s$ at RT, which is 2 times enhancement compared to that of Ge(100) [13].

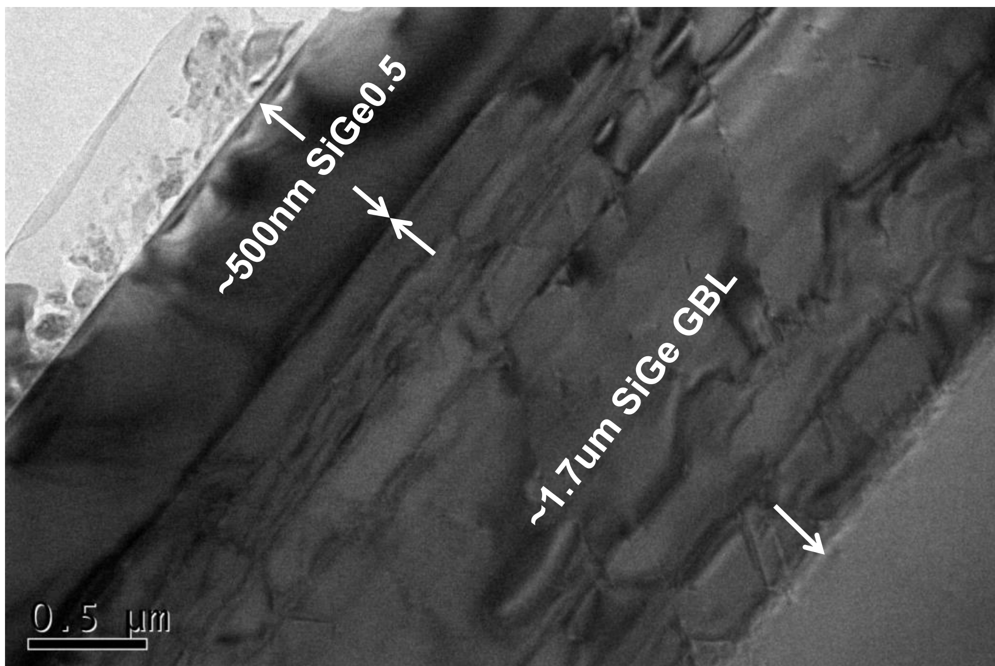

Fig.1-5 The TEM image of the 500nm $Si_{0.5}Ge_{0.5}$ on $Si_{1-x}Ge_x$ relaxed buffer layer. Note that the strain is gradually relaxed by the relaxed buffer layer to make $Si_{0.5}Ge_{0.5}$ be defect free.

1.4 Source/Drain Material Engineering

Due to the good gate control of FinFETs, the strain technology is more important than the EOT scaling. $Si_{1-x}Ge_x$ source/drain stressor [14]-[16] is one of the most successful strain techniques for pMOS performance. Besides, the Si1-xGex S/D reduces the resistance of S/D substantially [17]. The SiGe S/D has been used in the Intel 22 nm node FinFETs [18]. The shape stressor along the <110> FinFETs channel direction changes from rectangular to diamond (Fig. 1-6), but is conformal along the <100> channel direction. The reason for the diamond shape could be the fin orientation and the orientation dependent growth rate difference (Fig. 1-7) [19].

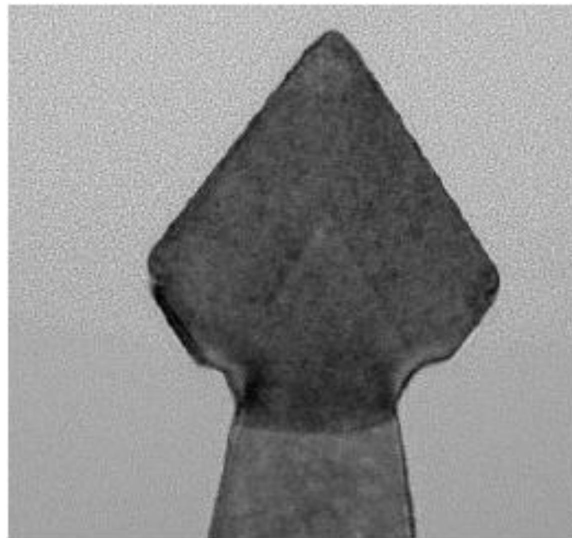

Fig.1-6 The TEM of the PMOS channel in the S/D region showing the SiGe epitaxy in the S/D region [18].

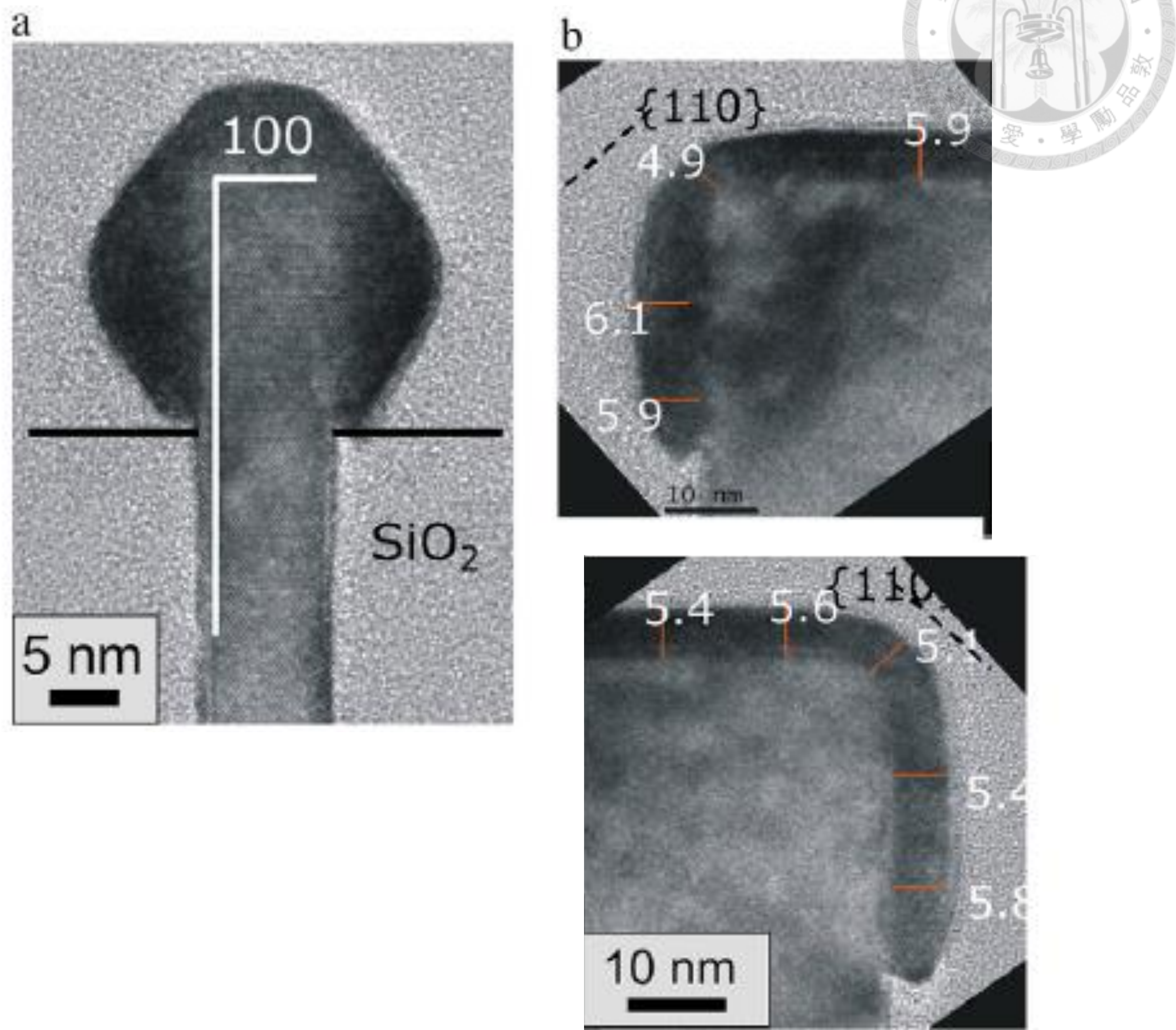

Fig.1-7 TEM images of $Si_{60}Ge_{40}$ layer grown on FinFET structures defined on (100) Si: (a) fin oriented along <110> direction, (b) fin oriented along <100> direction [19].

1.5 Dissertation Organization

The motivation of the SiGe and Ge epitaxial growth for advanced device applications are given in the previous sections of this chapter. The importance of the SiGe or Ge epitaxial growth for high mobility channel and S/D stressor are emphasized.

In chapter 2, using Unaxis UHV/CVD, where the growth temperature and unexpected contamination is low, the Si and Ge atoms surface diffusion and selective growth for the SiGe nanoring formed by Ge out-diffusion mechanism in different ambient are discussed in this chapter. When the central area of quantum dot is passivated by H, the epitaxial Si capping layer cannot cover the whole quantum dots and formed uncapped quantum dot. SiGe nanoring can be formed by 500°C *in situ* annealing in 1hr. When the epitaxial Si capping layer covers the whole quantum dots grown in He ambient, more than 4hrs *in situ* annealing is needed to form SiGe nanorings. Si capping layer grown in less H ambient can retard the SiGe nanoring formation is demonstrated.

In chapter 3, a transition from three- to two-dimensional growth for Si grown on Ge(100) is first observed in this chapter. With the increasing Si deposition, the Si growth changes from three- to two-dimensional growth mode and the dots disappear gradually. Finally, the surface is smooth with the roughness of 0.26nm, similar to the original Ge substrate, when 15 nm Si is deposited. More Ge segregation on the wetting layer leads to more open sites to increase the subsequent Si growth rate on the wetting layer than on the Si dots. The in-plane x-ray diffraction by synchrotron radiation is used to observe the evolution of tensile strain in the Si layer grown on Ge (100) substrate.

Growth rate enhancement with more Ge content leads to the morphology change for Si growth on Ge.

In chapter 4, basic theory and mechanism factors of epitaxial SiGe growth mechanism is discussed previously. Open sites creation and precursor adsorption are the main causes affect the SiGe growth rate. Using ASM Epsilon RTCVD, the SiGe growth rate is studied in different conditions, including growth ambient, Ge content, and gas precursors. Base on the previous observation of SiGe growth, the SiGe growth rate can be enhanced by having more open sites on surface. Due to easier H desorption from Ge than from Si, more Ge content surface can enhance SiGe growth rate by having more open sites than its with less Ge content. Besides, when using silane (SiH_4) in N_2 ambient instead of H_2 can enhance both the SiGe and Ge growth rate by 2x~3x. But, harder gas phase $SiCl_2$ desorption in N_2 ambient when using dichlorosilane (SiH_2Cl_2) as Si source can retard the Si and Ge adsorption and reduce the SiGe growth rate. X-ray diffraction and photoluminescence are used to determine the Ge content. And higher growth rate results to lower Ge content of SiGe is found.

From the chapter 5 to chapter 6, the two doping technologies for Ge using CVD are studied. Conventional doping technology, like ion implantation, can create defects even after implant anneal. For n-type dopant, the point defects such as Ge vacancies are the main root cause of fast diffusion of dopants and low activation fraction. For p-type dopant, stable defects by implantation-induced crystal disorder remain after long time annealing. All of these defects degrade the Ge diode performance to have non-ideal forward current, low on/off ratio, and high reverse saturation current. In chapter 5, the

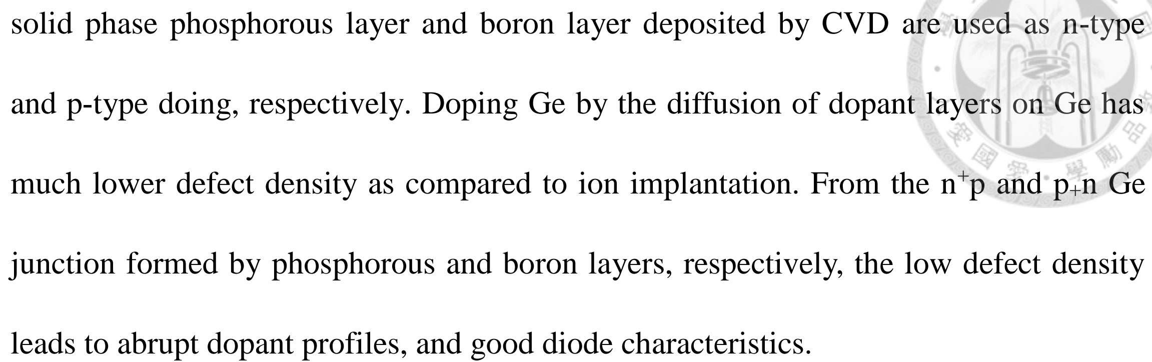

solid phase phosphorous layer and boron layer deposited by CVD are used as n-type and p-type doing, respectively. Doping Ge by the diffusion of dopant layers on Ge has much lower defect density as compared to ion implantation. From the n^+p and p_+n Ge junction formed by phosphorous and boron layers, respectively, the low defect density leads to abrupt dopant profiles, and good diode characteristics.

In chapter 6, *in situ* doping technology which is also free from implantation damage is studied. To reduce the dopant desorption during *in situ* doping, low temperature growth with post activation annealing is used to have high activated carrier density. For phosphorous doped Ge, limited dopant diffusion due to the nanosecond duration of the laser annealing is used. Higher and steeper dopant distribution can have that it with rapid thermal annealing and *in situ* H_2 annealing. $2x10^{20}$ cm^{-3} n-type Ge can have using *in situ* phosphorous doped Ge activated by laser. For boron doped Ge, laser anneal could introduce interstitial defects. These defects can result to dopant diffusion or even inactivation by boron-interstitial-cluster. $3x10^{20}$ cm^{-3} p-type Ge can have using *in situ* boron doped Ge activated by *in situ* annealing.

In the chapter 7, the important contribution and conclusion of SiGe and Ge epitaxy growth and doping are summarized. Besides, the future works on CVD epitaxy which can used in the improved device application is discussed in the last part of this thesis.

Reference:

[1] http://en.wikipedia.org/wiki/Transistor_count.

[2] Y. Taur and T. H. Ning, Fundamentals of Modern VLSI Devices, Cambridge, (2002).

[3] The website of Intel Corp: http://newsroom.intel.com/docs/DOC-2032.

[4] M. Lundstrom, *International Electron Devices Meeting (IEDM)*, Technical Digest, 789 (2003).

[5] C. Jungemann and B. Meinerzhagen, *International Electron Devices Meeting (IEDM)*, Technical Digest, 191 (2003).

[6] A. G. O'neill and A. D. Antoniadis, *IEEE Trans. Electron Devices*, **43**, 911 (1996).

[7] B. S. Meyerson, *IBM J. Res. Develop.*, **44**, 132 (2000)

[8] F. W. Smith and G. Ghiddini, *Journal of the Electrochemical Society*, **133**, 1300 (1984)

[9] C. -Y. Peng, F. Yuan, C. -Y. Yu, P. -S. Kuo, M. H. Lee, S. Maikap, C. -H. Hsu, and C. W. Liu, *Appl. Phys Lett*, **90**, 012114 (2007)

[10] R.Pillarisetty, "Academic and Industry research progress in Germanium Nanodevices", Nature, vol. 479,17 (2011).

[11] S. -H. Lee, J. Huang, P. Majhi, P. D. Kirsch, B. -G. Min, C. -S. Park, J. Oh, W. -Y. Loh, C. -Y. Kang, B. Sassman, P. Y. Hung, S. McCoy, J. Chen, B. Wu, G. Moon, D. Heh, C. Young, G. Bersuker, H. -H. Tseng, S. K. Banerjee, and R. Jammy,

Symposium on VLSI Technology Digest of Technical Papers, 74 (2009).

[12] N. Taoka, W. Mizubayashi, Y. Morita, S. Migita, H. Ota, and S. Takagi, *Symposium on VLSI Technology Digest of Technical Papers*, 80 (2009).

[13] Shu-Han Hsu, Hung-Chih Chang, Chun-Lin Chu, Yen-Ting Chen,Wen-Hsien Tu, Fu Ju Hou, Chih, Hung Lo, Po-Jung Sung, Bo-Yuan Chen,Guo-Wei Huang, Guang-Li Luo, C.W.Liu, Chenming Hu,and Fu-Liang Yang, *International Electron Devices Meeting (IEDM)*, Technical Digest, 23.6 (2012).

[14] M.D.Giles, M.Armstrong, C.Auth, S.M.Cea, T.Ghani, T.Hoffmann, R.Kotlyar, P.Matagne, K.Mistry, R.Nagisetty, B.Obradovic, R.Shaheed, L.Shifren, M.Stettler, S.Tyagi, X.Wang, C.Weher, K.Zawadzki, *Symposium on VLSl Technology Digest of Technical Papers*, pp. 118-119, (2004).

[15] Z. Luo, Y. Chong, J. Kim, N. Rovedo, B. Greene, S. Panda, T. Sato, J. Holt, D. Chidambarrao, J. Li, R. Davis, A. Madan, A. Turansky, O. Gluschenkov, R. Lindsay, Ajmera, J. Lee, S. Mishra, R. Amos, D. Schepis, H. Ng, and K. Rim, *IEDM Tech. Dig*., pp. 495–498, (2005).

[16] F. Nouri, P. Verheyen, L. Washington, V. Moroz, I. De Wolf, M. Kawaguchi, S. Biesemans, R. Schreutelkamp, Y. Kim, M. Shen, X. Xu, R. Rooyackers, M. Jurczak, G. Eneman, K. De Meyer, L. Smith, D. Pramanik, H. Forstner, S. Thirupapuliyur, and G. Higashi, *IEDM Tech. Dig*., pp. 1055–1058, (2004).

[17] V. Moroz, G. Eneman, P. Verheyen, F. Nouri, L. Washington, L. Smith, M.

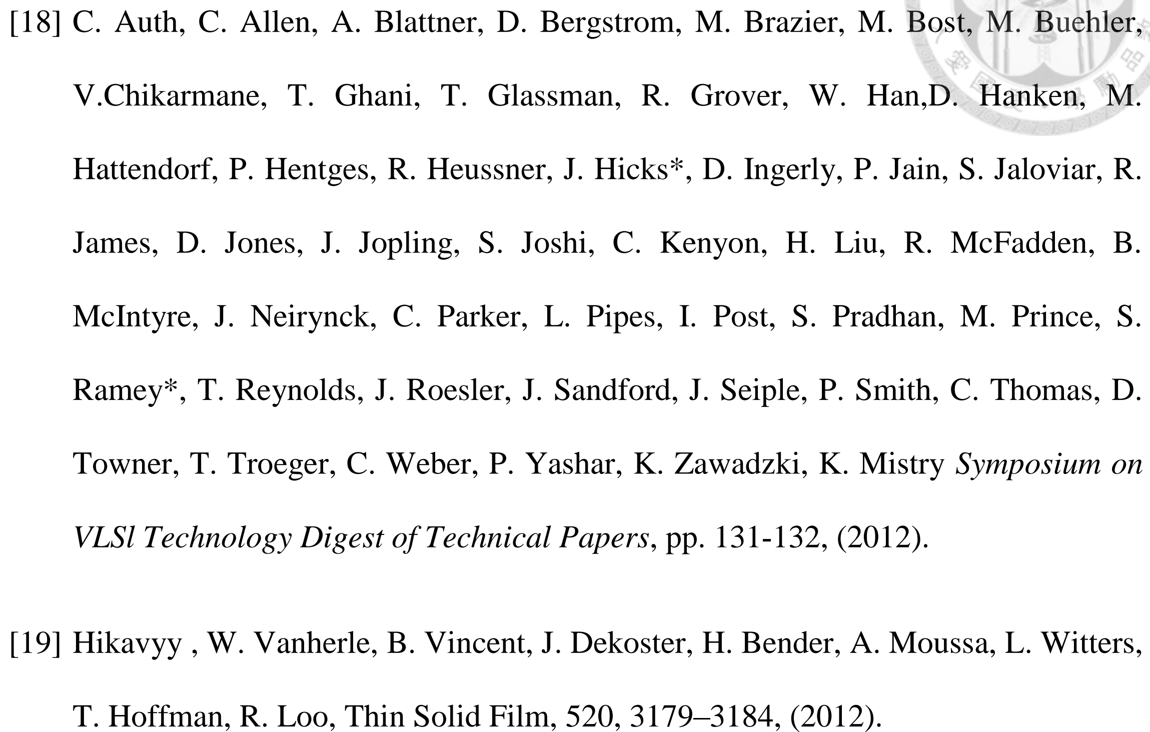

Jurczak, and D. Pramanik, *Proc. SISPAD*, pp. 143–146, (2005).

[18] C. Auth, C. Allen, A. Blattner, D. Bergstrom, M. Brazier, M. Bost, M. Buehler, V.Chikarmane, T. Ghani, T. Glassman, R. Grover, W. Han,D. Hanken, M. Hattendorf, P. Hentges, R. Heussner, J. Hicks*, D. Ingerly, P. Jain, S. Jaloviar, R. James, D. Jones, J. Jopling, S. Joshi, C. Kenyon, H. Liu, R. McFadden, B. McIntyre, J. Neirynck, C. Parker, L. Pipes, I. Post, S. Pradhan, M. Prince, S. Ramey*, T. Reynolds, J. Roesler, J. Sandford, J. Seiple, P. Smith, C. Thomas, D. Towner, T. Troeger, C. Weber, P. Yashar, K. Zawadzki, K. Mistry *Symposium on VLSl Technology Digest of Technical Papers*, pp. 131-132, (2012).

[19] Hikavyy , W. Vanherle, B. Vincent, J. Dekoster, H. Bender, A. Moussa, L. Witters, T. Hoffman, R. Loo, Thin Solid Film, 520, 3179–3184, (2012).

Chapter 2

Growth and Control of SiGe Nanoring Formation

2.1 Introduction

Self-assembled quantum dots (QDs) have attracted much interest for the potential applications of nanoelectronics [1–3]. Nanoring structures have also been widely observed in III-V system [4,5] and applied to optoelectronics [6]. SiGe nanorings on Si(100) grown both by molecular beam epitaxy [7] and ultrahigh vacuum chemical vapor deposition (UHV/CVD) [8] have been reported previously. The UHV/CVD growth of nanoring at 600 ^{o}C by Si surface diffusion can only be observed in very limit process window due to specific growth mechanism and this kind of SiGe nanorings can hardly meet the device requirements.

Both the increasingly Si cap growth and the high thermal budget can destroy this kind of nanoring structures [9]. The nanoring formed at 500°C by Ge out-diffusion under Si cap region was preferred to control the nanoring formation. For the blank growth of SiGe, carrier gas (H_2 or He) was well-known to change the growth kinetics [10]. The hydrogen passivation, which can influence the Ge concentration and the strain in the SiGe nanostructures, plays a crucial role in the SiGe quantum wells (QWs) and SiGe QDs growth. For QWs growth, The H_2 carrier gas increases Si segregation during the

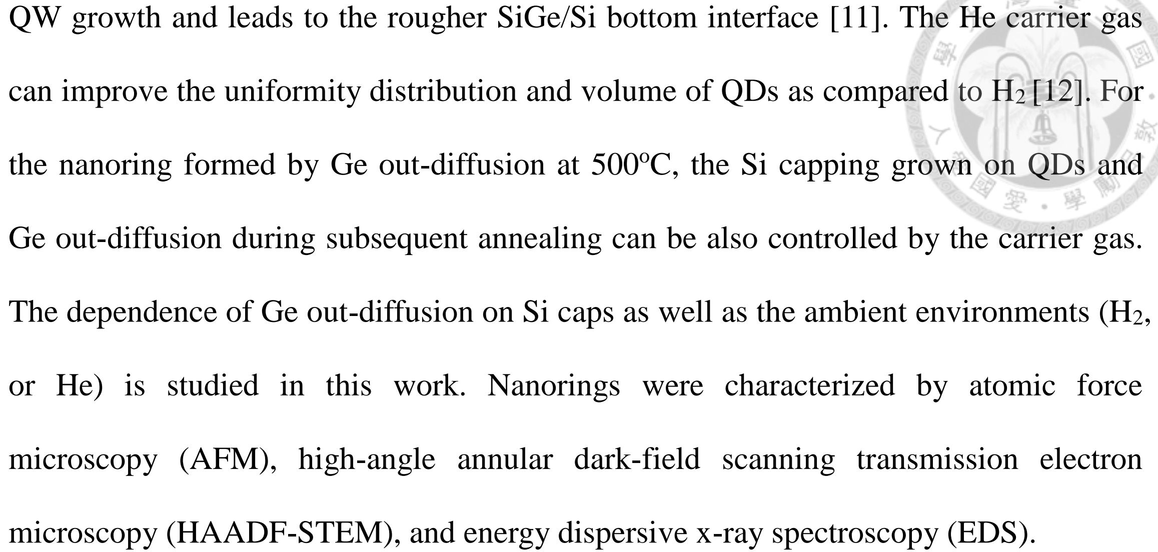

QW growth and leads to the rougher SiGe/Si bottom interface [11]. The He carrier gas can improve the uniformity distribution and volume of QDs as compared to H_2 [12]. For the nanoring formed by Ge out-diffusion at 500°C, the Si capping grown on QDs and Ge out-diffusion during subsequent annealing can be also controlled by the carrier gas. The dependence of Ge out-diffusion on Si caps as well as the ambient environments (H_2, or He) is studied in this work. Nanorings were characterized by atomic force microscopy (AFM), high-angle annular dark-field scanning transmission electron microscopy (HAADF-STEM), and energy dispersive x-ray spectroscopy (EDS).

2.2 Experiments

SiGe nanorings on Si(100) were grown by UHV/CVD at 500 °C. Pure silane (SiH_4) and germane (GeH_4) were used as reactant gases. Due to the hot-wall system, the growth temperature and temperature are fixed during the growth. The hot-wall system can prevent the process environment from the out-gasing of the chamber wall. The background impurity can be reduced, and the film quality would thus be improved. The base pressure of UHV/CVD system is ~10^{-9} torr and 10^{-3} torr during process. HF-dip last is used to have a hydrogen passivated wafer surface. After clean, the wafer is loaded into the load lock chamber directly. The process wafers will be put into the loader chamber first, and pump to ~10^{-6} torr. When the pressure inside the loader chamber matches the set point, the chamber door will open, and the wafer is transformed into the process chamber. After the transformation, the wafers would be baked in the process chamber with 300 sccm H_2 flow at the process temperature first to keep the Si surface hydrogen passivated. The ~3 nm Si buffer layer was grown first using SiH_4 after the HF

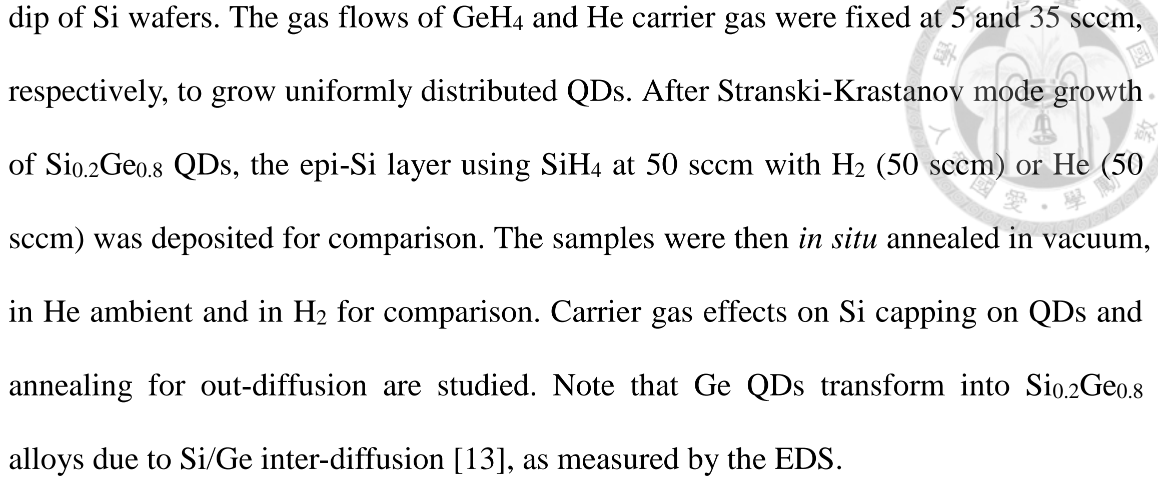

dip of Si wafers. The gas flows of GeH_4 and He carrier gas were fixed at 5 and 35 sccm, respectively, to grow uniformly distributed QDs. After Stranski-Krastanov mode growth of $Si_{0.2}Ge_{0.8}$ QDs, the epi-Si layer using SiH_4 at 50 sccm with H_2 (50 sccm) or He (50 sccm) was deposited for comparison. The samples were then *in situ* annealed in vacuum, in He ambient and in H_2 for comparison. Carrier gas effects on Si capping on QDs and annealing for out-diffusion are studied. Note that Ge QDs transform into $Si_{0.2}Ge_{0.8}$ alloys due to Si/Ge inter-diffusion [13], as measured by the EDS.

2.3 Carrier Gas Effects on Si cap for Nanoring Formation

To observe the carrier gas effects on Si capping on QDs, the high resolution cross-section TEM images at Fig. 2-1(a) and HAADFSTEM images of epi-Si layers using SiH_4/H_2 grown on QDs for contrast between Si and $Si_{0.2}Ge_{0.8}$ at Fig. 2-1(b). Since the H can passivate the open sites on the QD surface to reduce the silane adsorption at UHV/CVD growth pressure of 10^{-3} torr, the epi-Si layer deposited using SiH_4 and H_2 cannot form completely on the QDs, [Fig. 2-1(a) and (b)]. The tops of QDs are more relaxed [14] than the bottoms, and have a larger in-plane lattice constant than Si. If some Si atoms are accidentally deposited on the central area of the QDs, the tensile strain given by the tops of QDs can drive the diffusion of Si to the wetting layers [8]. For comparison, the TEM images at HAADF-STEM images of epi-Si layers using SiH_4/He can grow not only on the wetting layer but also on the QDs (Fig. 2-2(a) and (b)). Since the annular dark field image formed only by very high angle, incoherently scattered electrons — as opposed to Bragg scattered electrons for conventional TEM —

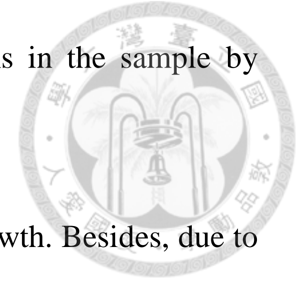

it is highly sensitive to variations in the atomic number of atoms in the sample by HAADF-STEM.

It is found that the QDs can be totally covered using SiH_4/He growth. Besides, due to the hydrogen passivation, the Si layer (~5 nm, Fig. 2-1) on the wetting layer for SiH_4/H_2 growth is also thinner than that for SiH_4/He growth (~7 nm, Fig. 2-2). Note the SiGe wetting layer is thinner than 1 nm for original QDs.

For 1 h annealing at 500°C in vacuum (10^{-9} torr) after SiH_4/H_2 growth for partially covered QDs, nanorings were observed [Fig. 2-3(a)]. These Ge atoms can out diffuse from the central area of uncapped QDs to form nanorings [Fig. 2-3(b)]. On the contrary, for the epi-Si layer deposited using SiH_4 and He, the H on the QDs surface was taken away by the He gas flow and left more surface open sites on QDs. The SiH_4 can be adsorbed and deposited on the whole QDs to form capped QDs [Fig. 2-4(b)]. Due to the Si cap, the Ge surface diffusion is relatively slow [15] No nanoring formation was observed after the same annealing condition (1 h at 500 ^{o}C) in vacuum[Fig. 2-4(a)].

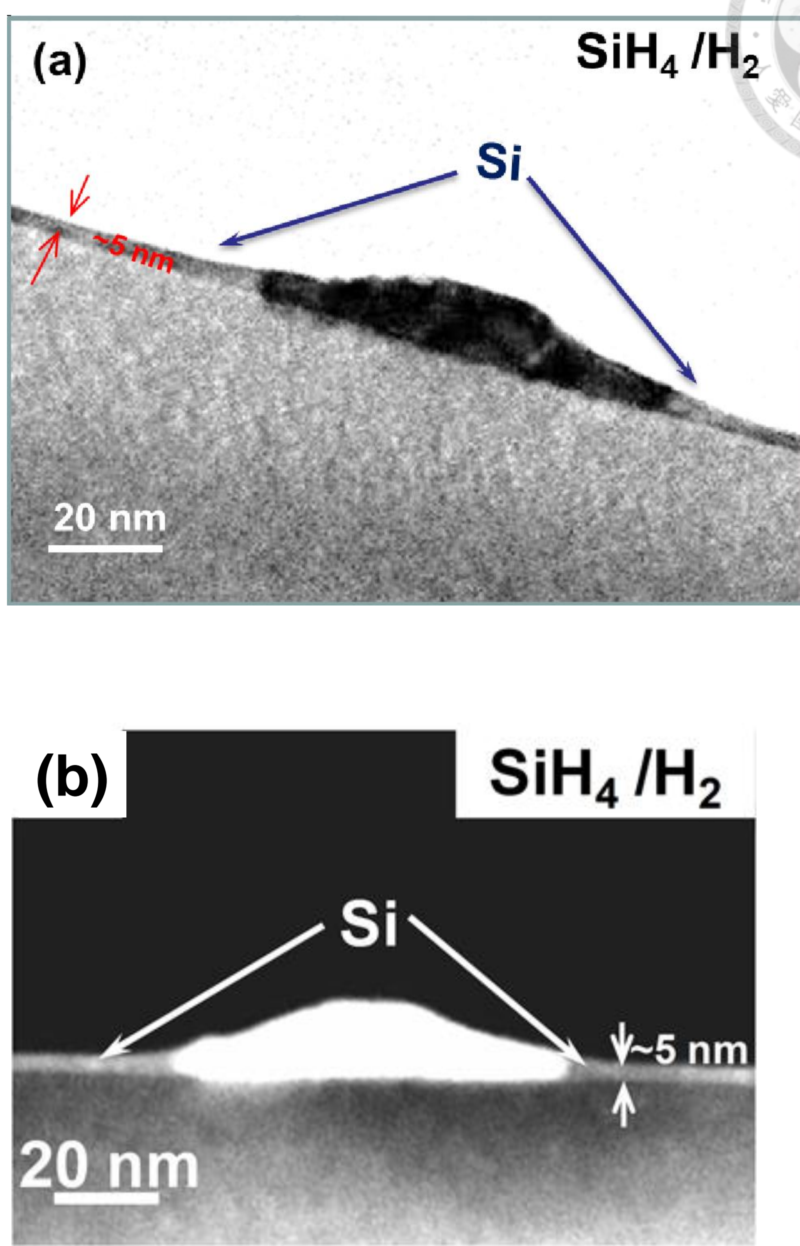

Fig.2-1 (a) High resolution cross-sectional TEM images and (b) HAADF-TEM images of the uncapped QD using SiH_4 and H_2. Note that the QDs is only partially capped and the Si thickness on wetting layer is only ~5nm.

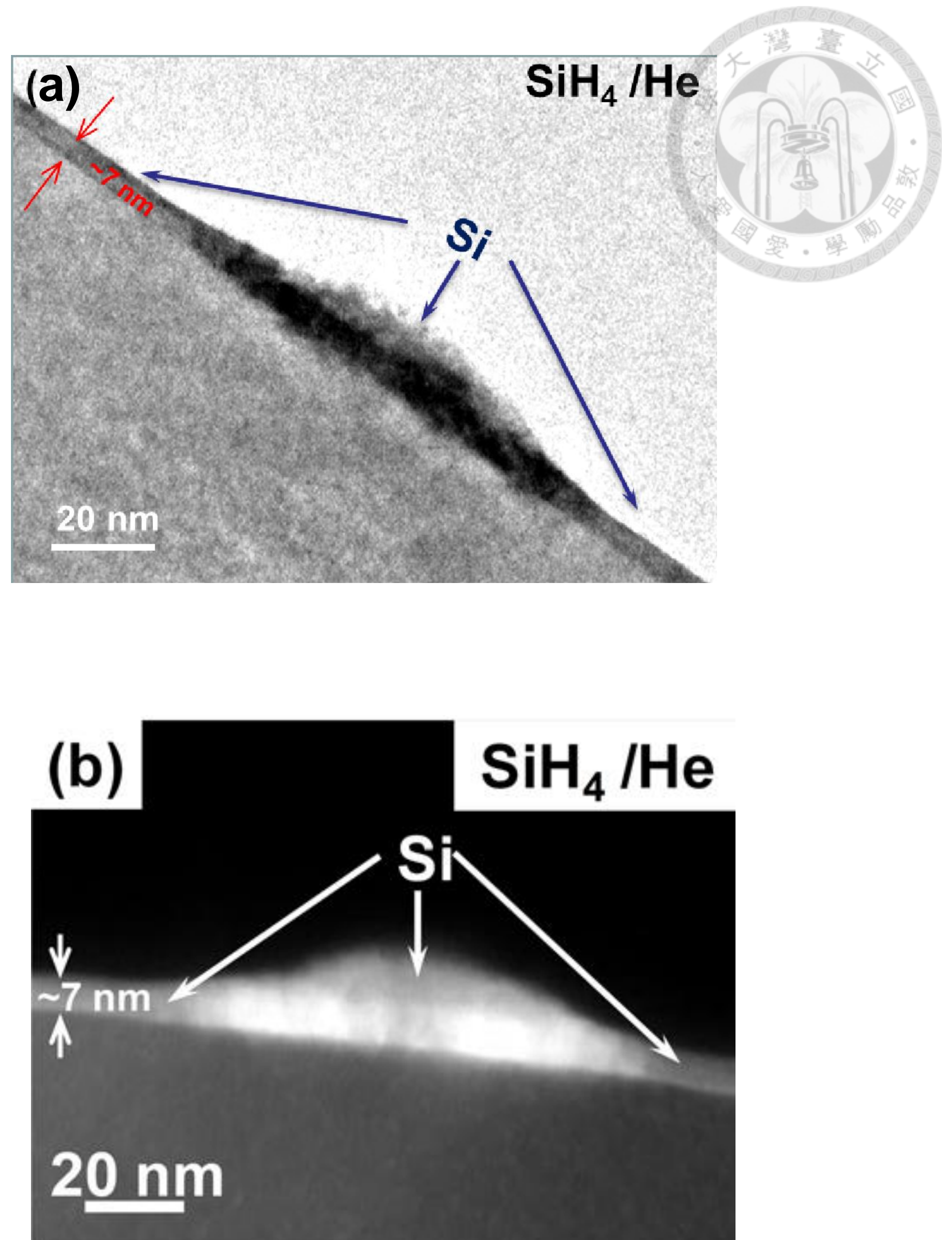

Fig.2-2 (a) High resolution cross-sectional TEM images and (b) HAADF-TEM images of the capped QD using SiH_4 and He. Note that the QDs is totally capped and the Si thickness on wetting layer is ~7nm which is thicker than its using SiH_4 and H_2.

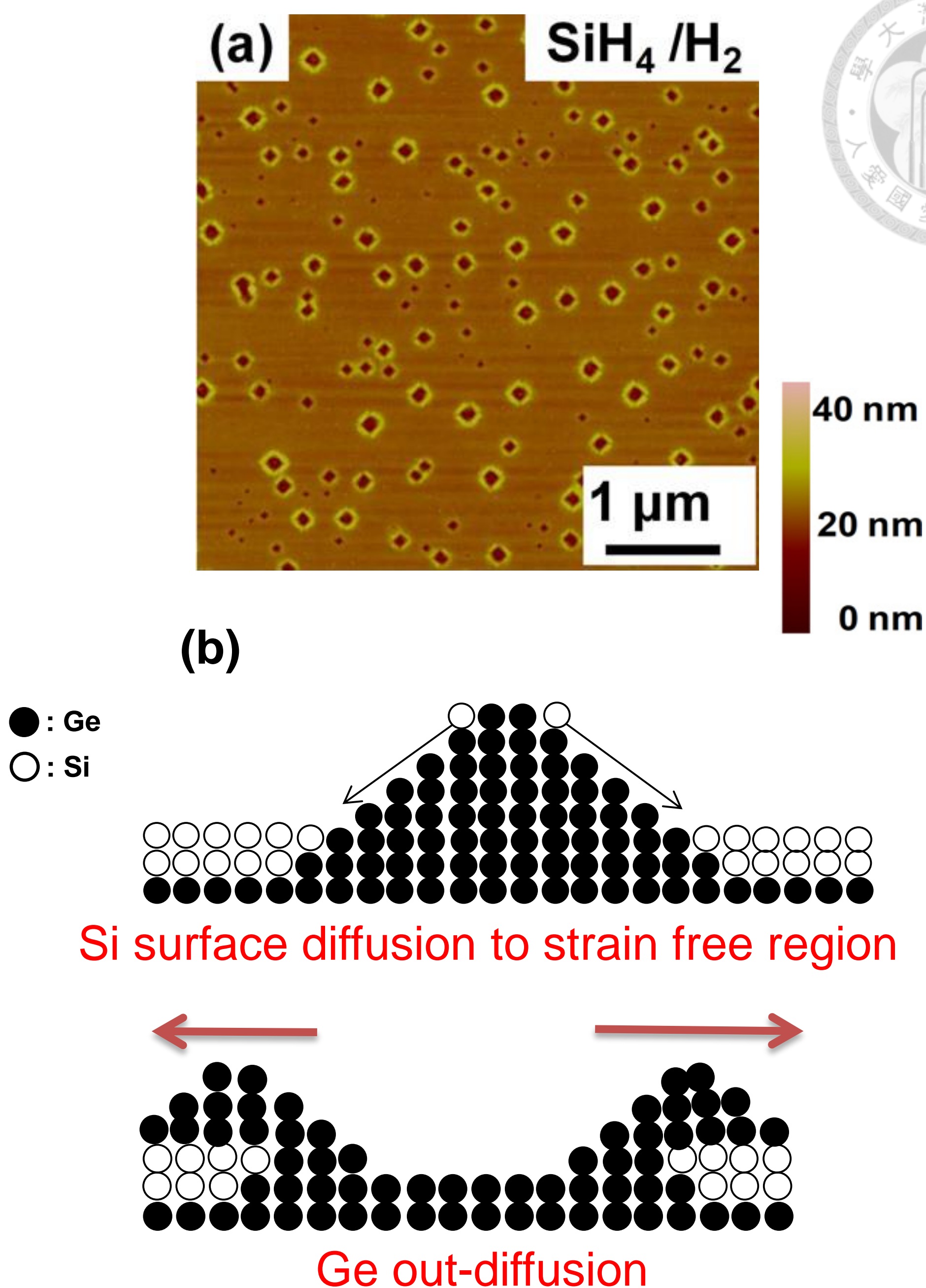

Fig.2-3 (a) The AFM images (5µm x 5µm) of nanorings transformed from uncapped QDs after 1h *in-situ* vacuum annealing and (b) The schematics of corresponding growth model of nanoring formation transformed from uncapped QDs. Note H passivation can prevent Si growth on top of the QD and enhance the Ge out-diffusion for nanoring formation

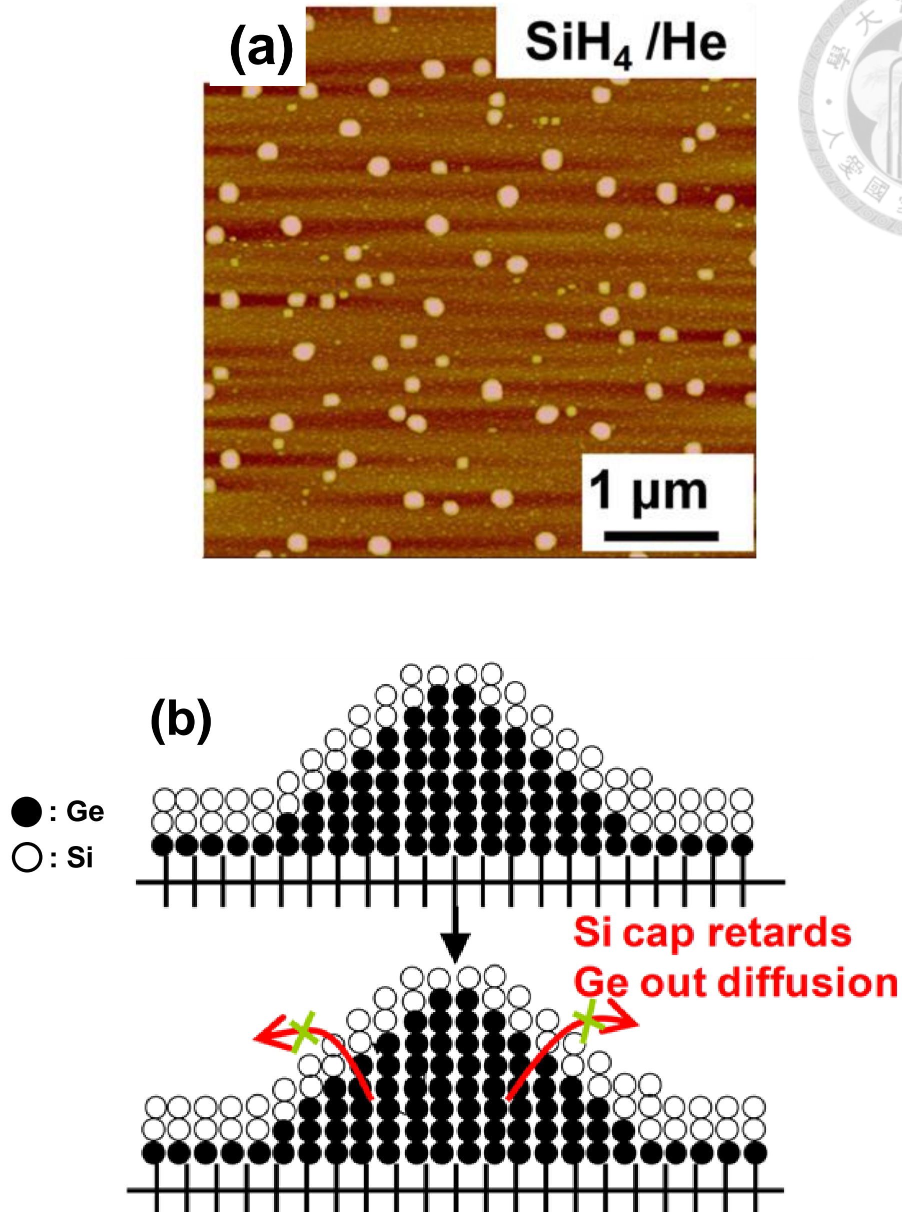

Fig.2-4 (a) The AFM images (5μm x 5μm) of capped QDs after 1 h *in-situ* annealing in vacuum at 500°C and (b) The schematics of corresponding growth model for no nanoring formed from capped QDs. Note that Si can be grown on top of QD with no H passivation and retard Ge out-diffusion to form nanorings

Fig. 2-5 is the three dimension AFM topography images of uncapped QDs and nanoring formed from uncapped QDs. The average width and height of uncapped QDs is 75nm and 25nm, respectively (Fig. 2-5(a)). And the average width and depth of nanorings is 130nm and 9nm, respectively (Fig. 2-5(b)). It is found that since Ge at the center of the uncapped QD diffuses outward to form nanoring, the width of the nanoring is larger than the uncapped QD. The Ge out-diffusion could be also observed from the high resolution TEM cross-section with dispersive x-ray spectroscopy (EDS) measurement of the nanoring (Fig.2-6). From the EDS, the Ge content at the ring edge is 27% higher than that at the center (11%). It is also an evidence of Ge out-diffusion to form nanorings. The result of higher Ge content at edge is different from molecular beam epitaxy (MBE) samples [16] because our growth temperature of 500°C is lower than the MBE temperature of 680 °C, and Si diffusion is not important in our work. Note that our early work [17] at higher growth temperature (600 °C) has similar results of MBE samples [16] grown at 680 °C.

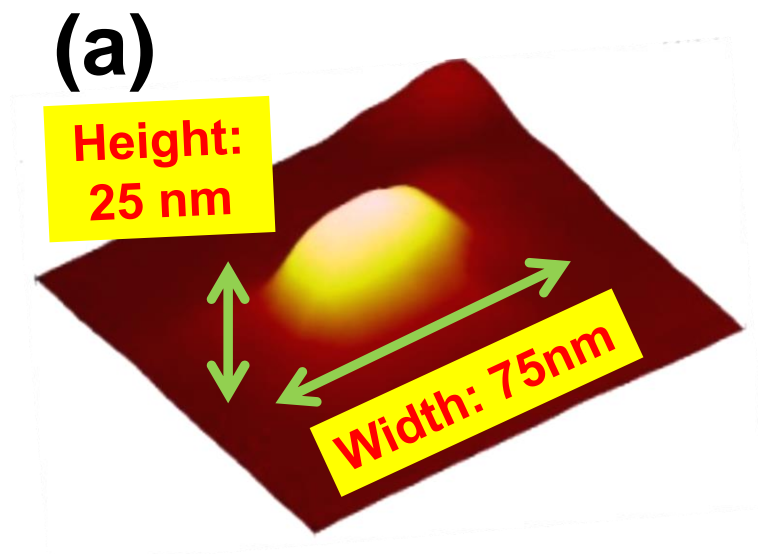

Fig.2-5 (a) The 3D AFM images of uncapped QDs

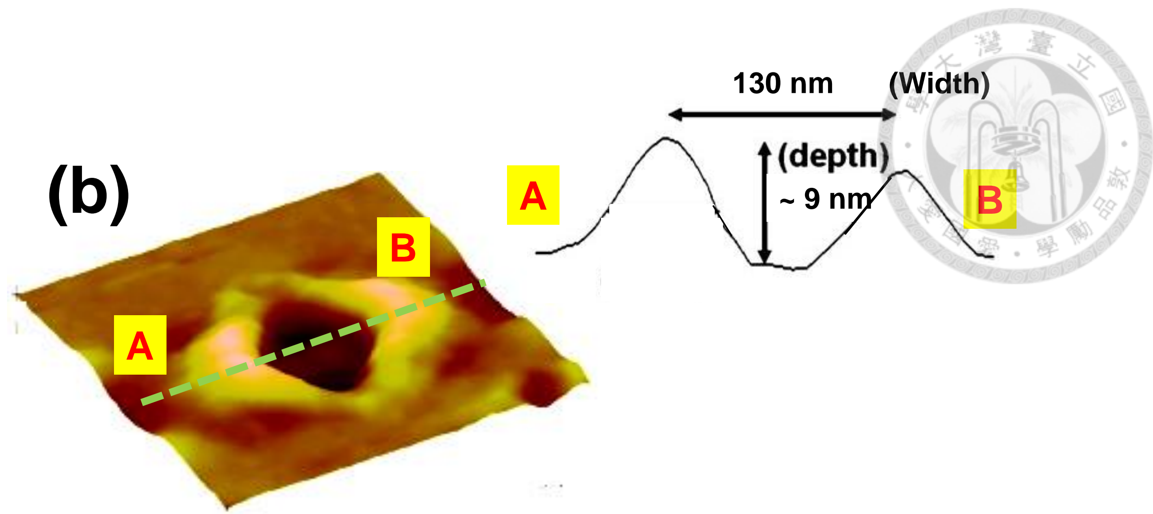

Fig.2-5 (b) The 3D AFM images of uncapped QDs after 1 h annealing in vacuum at 500ºC to form nanoring. Note that the width of nanoring is larger than QDs due to Ge out-diffusion.

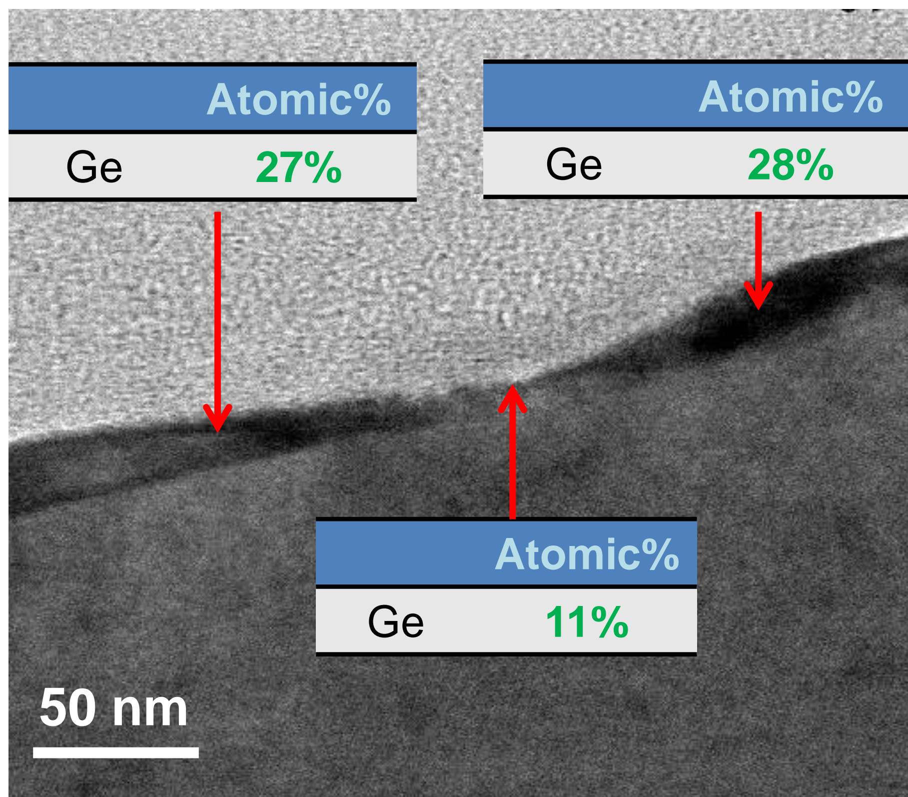

Fig.2-6 The high resolution TEM images and corresponding EDS measurement of the nanoring.

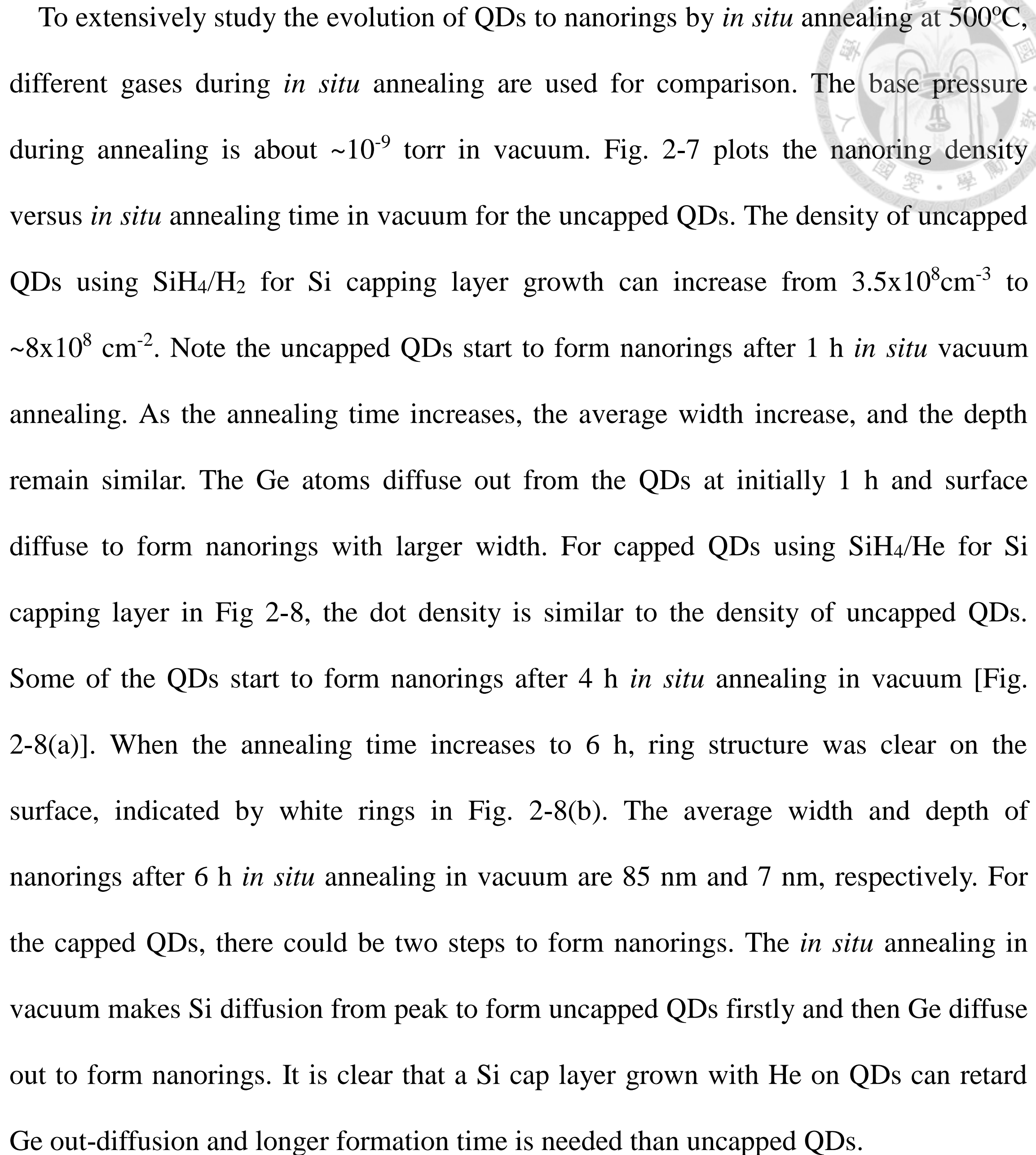

To extensively study the evolution of QDs to nanorings by *in situ* annealing at 500ºC, different gases during *in situ* annealing are used for comparison. The base pressure during annealing is about ~10^{-9} torr in vacuum. Fig. 2-7 plots the nanoring density versus *in situ* annealing time in vacuum for the uncapped QDs. The density of uncapped QDs using SiH_4/H_2 for Si capping layer growth can increase from $3.5x10^{8}cm^{-3}$ to ~$8x10^{8}$ cm^{-2}. Note the uncapped QDs start to form nanorings after 1 h *in situ* vacuum annealing. As the annealing time increases, the average width increase, and the depth remain similar. The Ge atoms diffuse out from the QDs at initially 1 h and surface diffuse to form nanorings with larger width. For capped QDs using SiH_4/He for Si capping layer in Fig 2-8, the dot density is similar to the density of uncapped QDs. Some of the QDs start to form nanorings after 4 h *in situ* annealing in vacuum [Fig. 2-8(a)]. When the annealing time increases to 6 h, ring structure was clear on the surface, indicated by white rings in Fig. 2-8(b). The average width and depth of nanorings after 6 h *in situ* annealing in vacuum are 85 nm and 7 nm, respectively. For the capped QDs, there could be two steps to form nanorings. The *in situ* annealing in vacuum makes Si diffusion from peak to form uncapped QDs firstly and then Ge diffuse out to form nanorings. It is clear that a Si cap layer grown with He on QDs can retard Ge out-diffusion and longer formation time is needed than uncapped QDs.

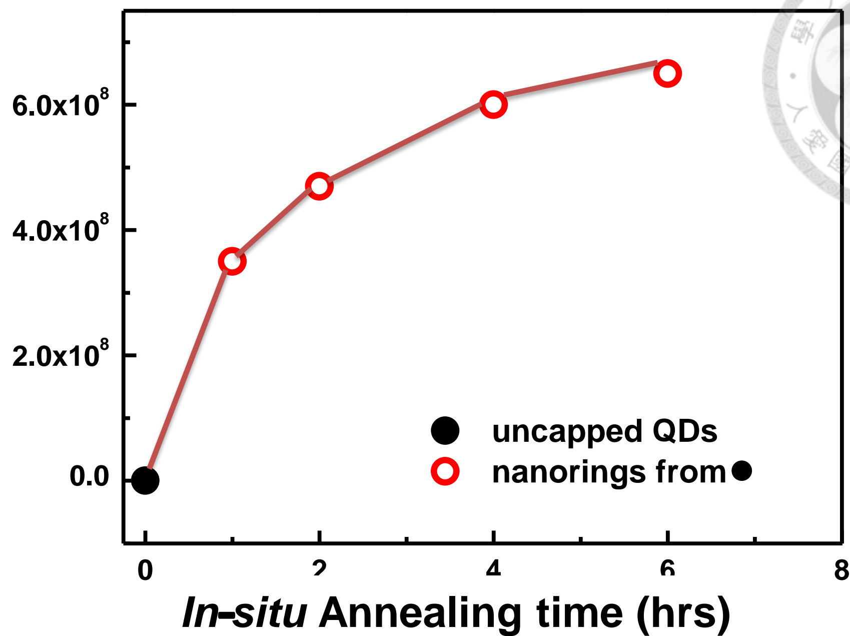

Fig.2-7 The nanoring density as a function of *in-situ* annealing time in vacuum from uncapped QDs.

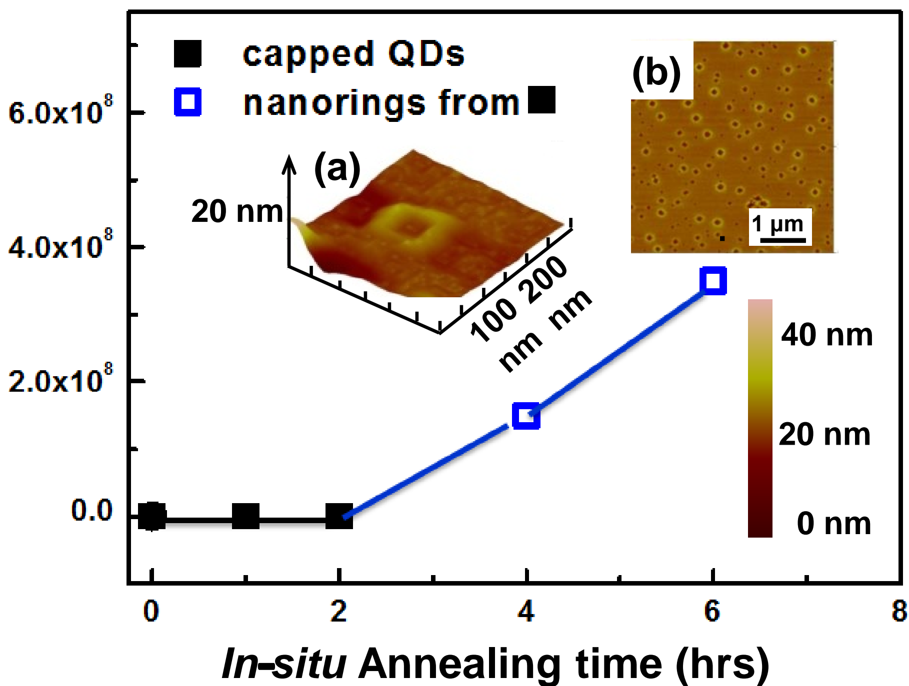

Fig.2-8 The nanoring density as a function of *in- situ* annealing time in vacuum from capped QDs. The inset images are the corresponding (a) 3D AFM image and (b) 5μm x 5μm AFM image of nanorings from capped QDs.

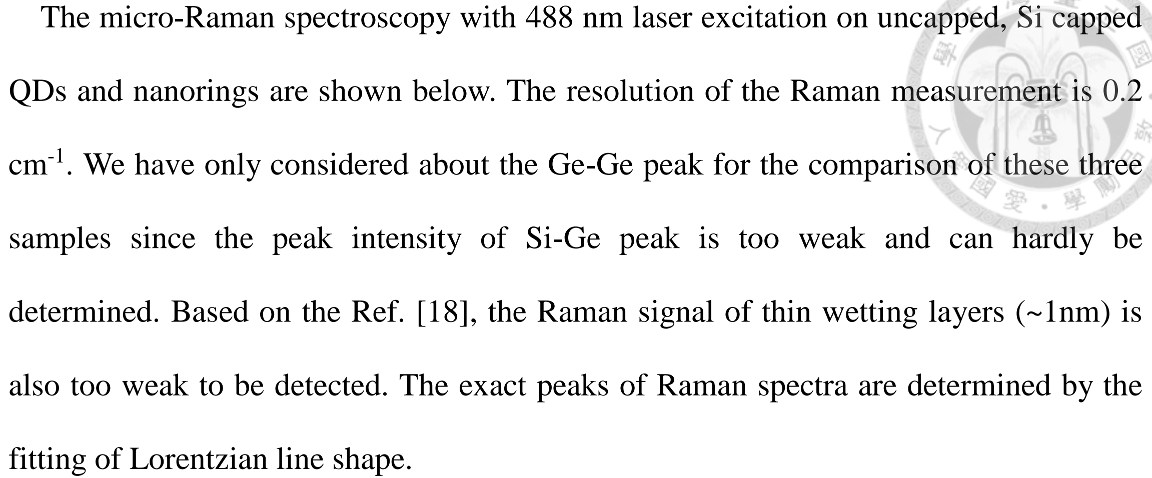

The micro-Raman spectroscopy with 488 nm laser excitation on uncapped, Si capped QDs and nanorings are shown below. The resolution of the Raman measurement is 0.2 cm^{-1}. We have only considered about the Ge-Ge peak for the comparison of these three samples since the peak intensity of Si-Ge peak is too weak and can hardly be determined. Based on the Ref. [18], the Raman signal of thin wetting layers (~1nm) is also too weak to be detected. The exact peaks of Raman spectra are determined by the fitting of Lorentzian line shape.

The Ge-Ge peak is sensitive to the strain and Ge concentration. Either the decrease of Ge content or the decrease of compressive strain inside SiGe QDs leads to the negative shift of Ge-Ge peak in the Raman spectra [13]. In our case, the Ge-Ge peak of the Si capped QDs sample is ~0.5 cm^{-1} higher than the uncapped QDs sample (Fig.2-9). From the Ref.19, even both the uncapped and Si capped QDs samples are under compressive strain, the uncapped QDs samples shows a lower compressive strain than Si capped QDs from XRD. The lager Ge-Ge LO phonon peak position of the capped QDs from Raman than from the uncapped QDs is probably due to additional compressive strain caused by the Si cap on QDs [19]. Larger compressive strain for capped Si QDs could come from the strain induced from the Si cap to QDs. Once the Si atoms diffuse from dot peak for uncapped QDs, the compressive strain in QDs can be relaxed.

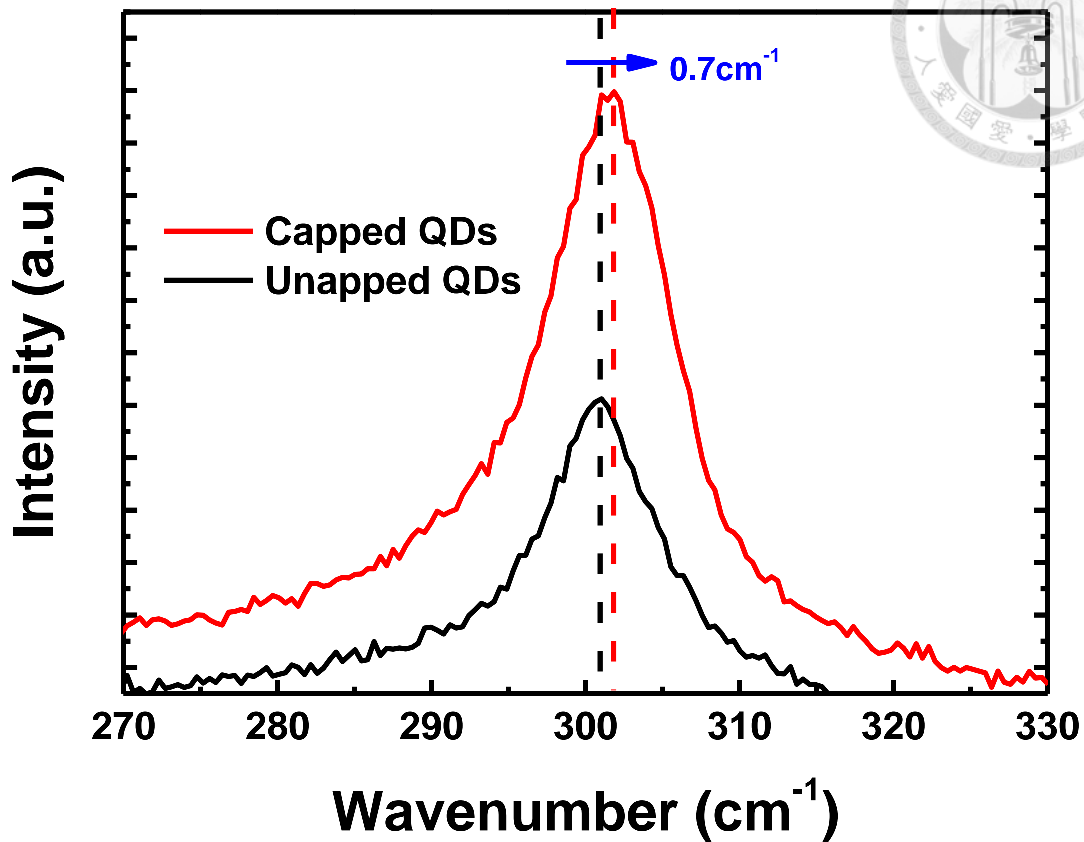

Fig.2-9 Ge–Ge LO phonon wave number positions for capped and uncapped QDs.

The Ge-Ge LO phonon peak as a function of *in situ* annealing time for uncapped QDs to form nanorings is shown in Fig. 2-10. The peaks of uncapped QDs increase after 1 h *in situ* annealing in vacuum where nanorings are already formed. Since the top of QDs is more relaxed than the bottom [14] the out-diffusion of Ge on the top QDs to form nanorings leaves more compressive strained bottoms. This leads to the positive shift of the Raman peak.

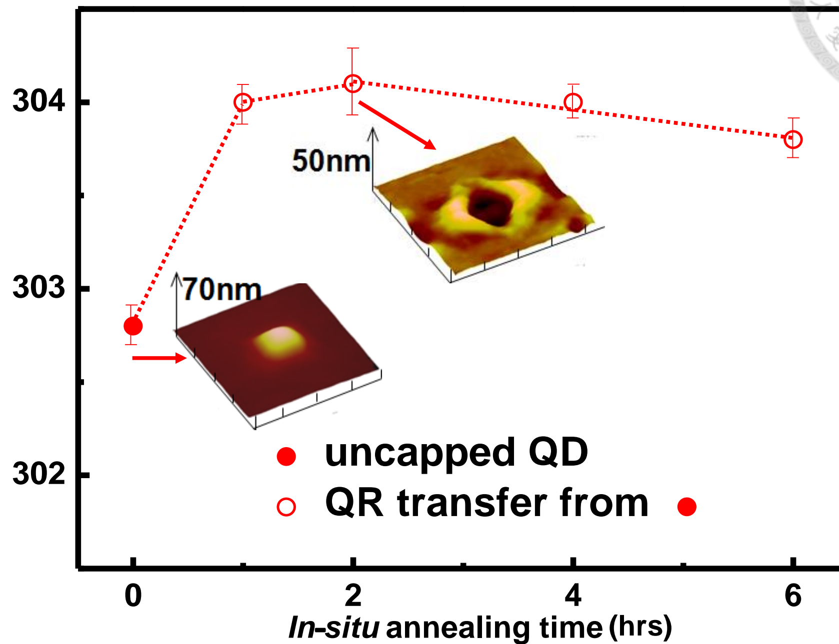

Fig.2-10 Ge–Ge LO phonon wave number positions as a function of *in-situ* annealing time in vacuum for uncapped QDs. Note the wave number shifts positively as soon as the nanorings formed

For Si capped QDs, the Ge-Ge LO phonon peak Raman have larger wave number than uncapped QDs due to additional compressive strain caused by the Si cap on QDs [19] and decreases after initial annealing time up to 2 h (Fig. 2-11). The negative shift may be due to the additional Si diffusion into Ge from the Si capping layer, which reduces Ge content in QDs and resulting to smaller Ge-Ge LO phonon wave number. Moreover, compressive strain in QDs can also decrease due to the thinning of the Si cap by *in-situ* annealing. When capped QDs transform to nanorings, Ge-Ge peaks shift to the larger wave number, indicating the increase of compressive strain in the nanorings,

which is similar to uncapped QDs. Note that the Raman peak of wetting layers should shift negatively if the Ge content decreases after the subsequent annealing, but our peaks have different shift by annealing (Fig. 2-10, Fig. 2-11), also indicating the signal from wetting layers can be ignored.

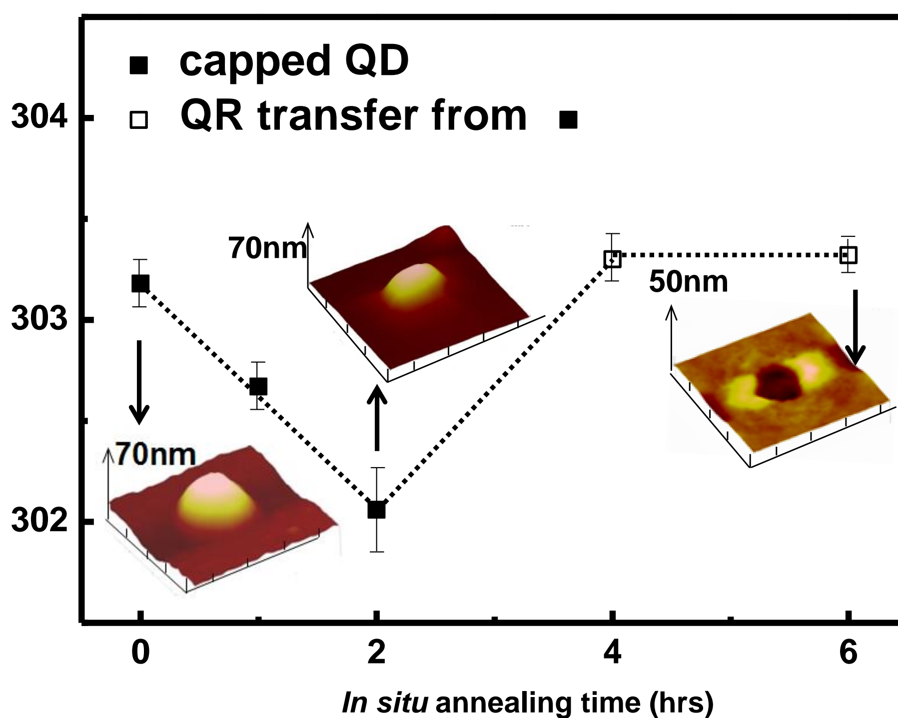

Fig.2-11 Ge–Ge LO phonon wave number positions as a function of *in-situ* annealing time in vacuum for capped QDs. Note the wave number of capped QDs and the positive shift as soon as the nanorings formed

2.4 Carrier Gas Effects on Annealing for Nanoring Formation

Except the Si capping layer effect on nanoring formation, the carrier gases during *in-situ* annealing for the possible nanoring formation are also studied. In the Fig 2-12(a)~(c), for capped QDs, the Ge cannot diffuse out to form nanorings by *in-situ* annealing in vacuum, in H_2 and in He. Si cap is the crucial role to retard the Ge out-diffusion for nanoring formation. The Si capping layer has also been a good candidate to passivate the $Si_{0.2}Ge_{0.8}$ p-type channel metal oxide semiconductor field effect transistors [20].

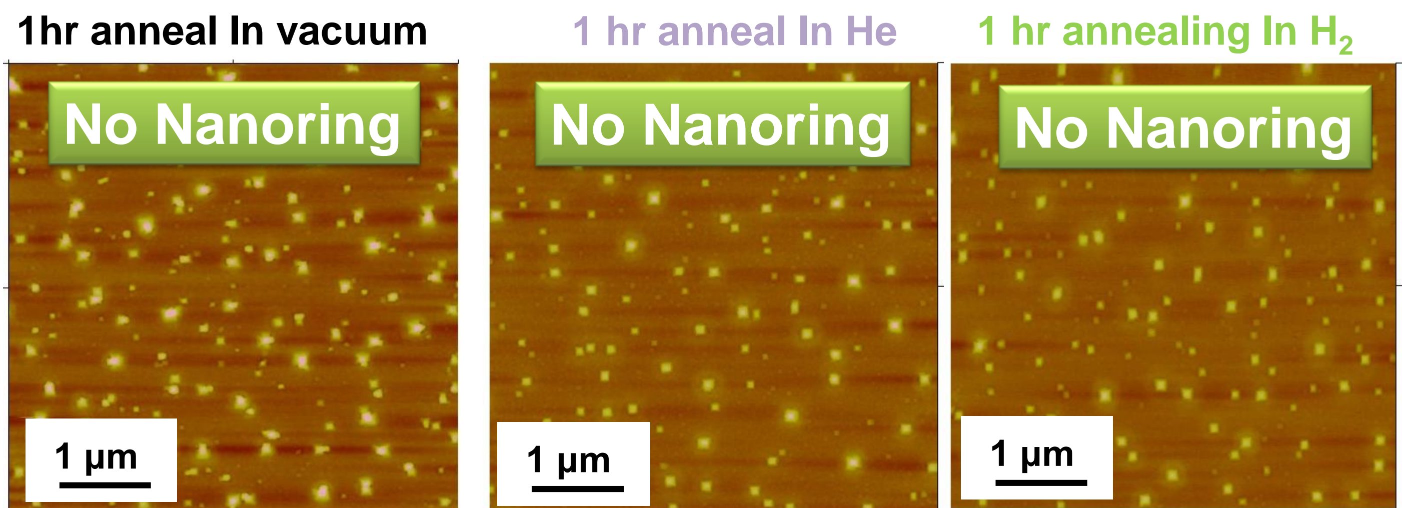

Fig.2-12 The AFM images (5μm x 5μm) of capped QDs with *in-situ* anneal at 500°C in vacuum, in He ambient and in H_2 ambient.

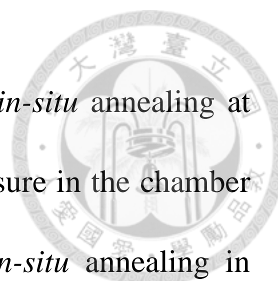

For uncapped QDs, Ge can diffuse out to form nanoring when *in-situ* annealing at 500°C in vacuum for only one hour (Fig.2-13), where the base pressure in the chamber is about 10^{-9} torr. The nanoring density can increase with the *in-situ* annealing in vacuum time and reach 7.5×10^{8} cm^{-2}. Even for uncapped QDs, no nanorings can be formed by *in-situ* annealing in H_2 or He at 500°C for 1hr. No nanoring can be formed from uncapped QDs even after annealing in H_2 up to 5 h. The nanoring can be formed only with annealing both in vacuum and in He ambient (Fig. 2-13).

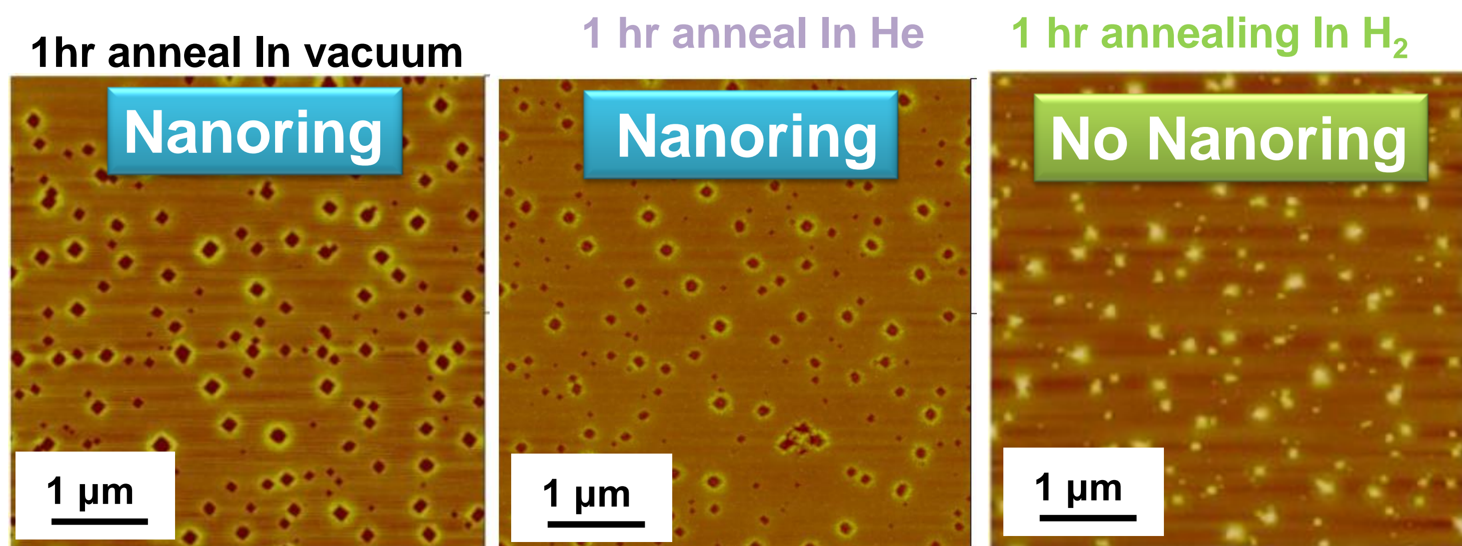

Fig.2-13 The AFM images (5μm x 5μm) of uncapped QDs with *in-situ* anneal at 500°C in vacuum, in He ambient and in H_2 ambient. Note no nanoring can be formed with *in- situ* anneal in H_2 even from uncapped QDs.

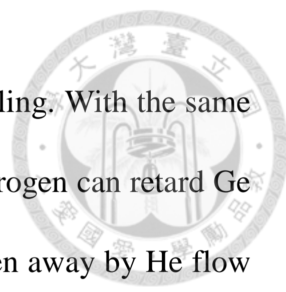

The Fig.2-14 is the model for uncapped QDs with different annealing. With the same hydrogen passivation effect, the QDs surface which covers with hydrogen can retard Ge out-diffusion. In the case with *in situ* annealing in He, H can be taken away by He flow and create unpassivated QDs, nanorings can be formed after 1 h at 500°C (Fig. 2-14). Therefore the hydrogen can not only retard the Si capping layer growth for uncapped QDs formation, but also retard the Ge out-diffusion during anneaing. For the application, post annealing with hydrogen instead of vacuum can be used for SiGe channel devices without capping layer. The time evolution of Raman spectra for H_2 annealing, in which no nanoring can be formed, shows a negative shift of Ge-Ge peak (Fig. 2-15), probably due to the diffusion of underneath Si into QDs.

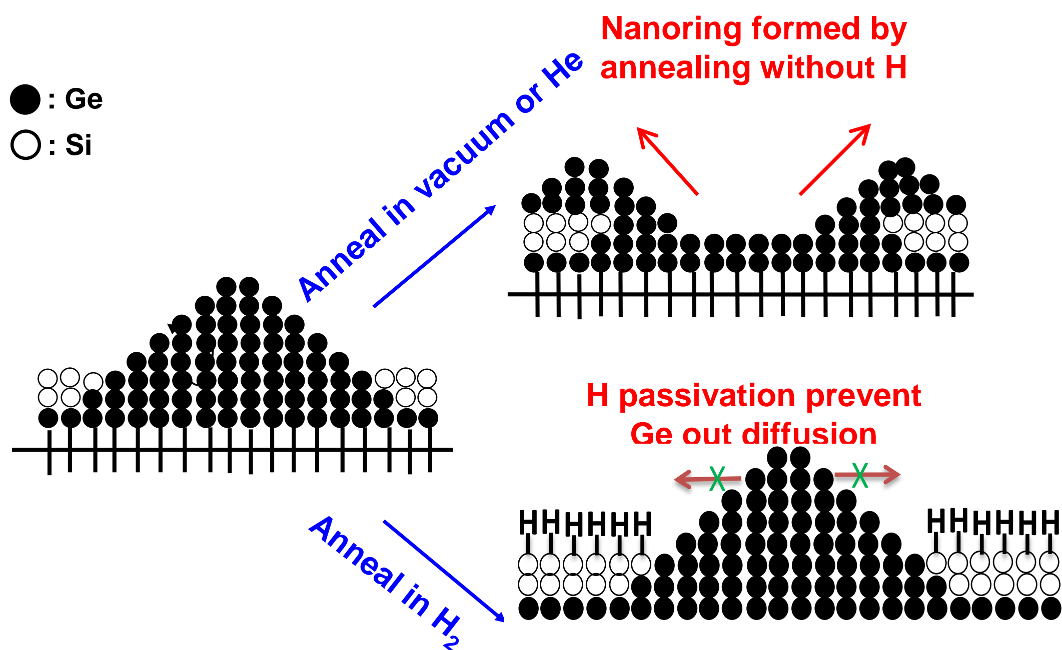

Fig.2-14 The schematics for annealing effects on nanoring formation. Even for the uncapped QDs, the nanoring cannot be formed with H_2 annealing by H passivation.

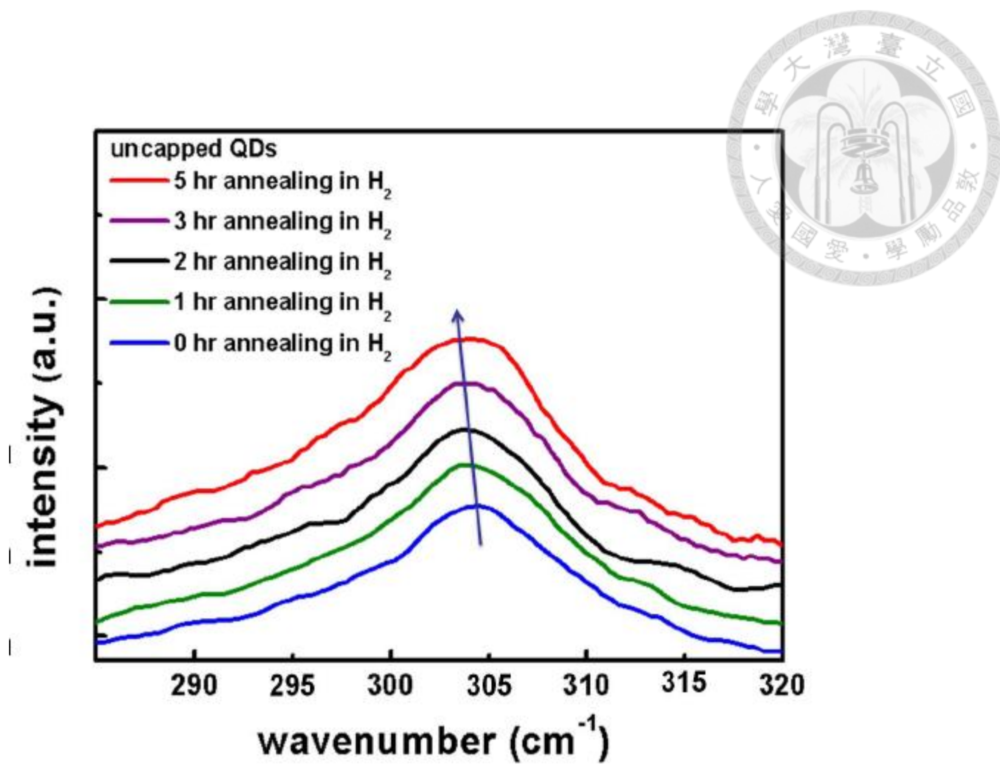

Fig.2-15 Raman spectra as a function of *in-situ* annealing time in H_2 for uncapped QDs

2.5 Summary

The Si layer has been used to passivate the $Si_{0.2}Ge_{0.8}$ p-channel metal oxide semiconductor field effect transistors [20]. The Ge out-diffusion from QDs is the key factor to form nanorings at 500°C, and the nanoring formation is also a good indicator of Ge out-diffusion. Both the Si cap and the hydrogen passivation can reduce the Ge out-diffusion while the annealing in vacuum and in He can enhance the Ge out-diffusion to form nanorings. The conditions to form nanoring is summarized in Table 2-1 Using the carrier gas effect, Ge out-diffusion which is good for nanoring formation but not desired for integral circuit process can be well controlled.

Table 2-1 The summary conditions for nanoring formation at 500°C.

Si capping layer effects

● : **quantum dots**
O : nanorings

Annealing in vacuum	0 hr	1 hr	2 hr	4 hr	6 hr
Si layer from **SiH_4/H_2**	●	O	O	O	O
Si layer from **SiH_4/He**	●	●	●	O	O

***In situ* annealing effects**

Uncapped QDs	**0 hr**	**1 hr**	**2 hr**	**3 hr**	**5 hr**
Annealing in He	●	O			
Annealing in H_2	●	●	●	●	●
Capped QDs	**0 hr**	**1 hr**	**2 hr**	**3 hr**	**5 hr**
Annealing in He	●	●	●		
Annealing in H_2	●	●	●		

Reference:

[1] G. Jin, J. L. Liu, and K. L. Wang, Appl. Phys. Lett. 83, 2847 (2003).

[2] Y. Q. Wu, F. H. Li, J. Cui, J. H. Lin, R. Wu, J. Qin, C. Y. Zhu, Y. L. Fan, X. J. Yang, and Z. M. Jiang, Appl. Phys. Lett. 87, 223116 (2005).

[3] H. J. Kim and Y. H. Xie, Appl. Phys. Lett. 79, 263 (2001).

[4] D. Granados and J. M. Garcia, Appl. Phys Lett. 82, 2401 (2003).

[5] G. Huang, W. Guo, P. Bhattacharya, G. Ariyawansa, and A. G. U. Perera, Appl. Phys. Lett. 94, 101115 (2009).

[6] M. W. Kim and P.-C. Ku, Appl. Phys. Lett. 98, 201105 (2011).

[7] J. Cui, Q. He, X. M. Jiang, Y. L. Fan, X. J. Yang, F. Xue, and Z. M. Jiang,Appl. Phys. Lett. 83, 2907 (2003).

[8] S. W. Lee, L. J. Chen, P. S. Chen, M.-J. Tsai, C. W. Liu, T. Y. Chien, and C. T. Chia, Appl. Phys. Lett. 83, 5283 (2003).

[9] C.-H. Lee, Y.-Y. Shen, C. W. Liu, S. W. Lee, B.-H. Lin, and C.-H. Hsu, Appl. Phys. Lett. 94, 141909 (2009).

[10] W. A. P. Claassen and J. Bloem, J. Crytal Growth 51, 443 (1981).

[11] E. Rudkevich, F. Liu, D. E. Savage, T. F. Kuech, L. McCaughan, and M. G. Lagally, Phys. Rev. Lett., 81, 3467, (1998).

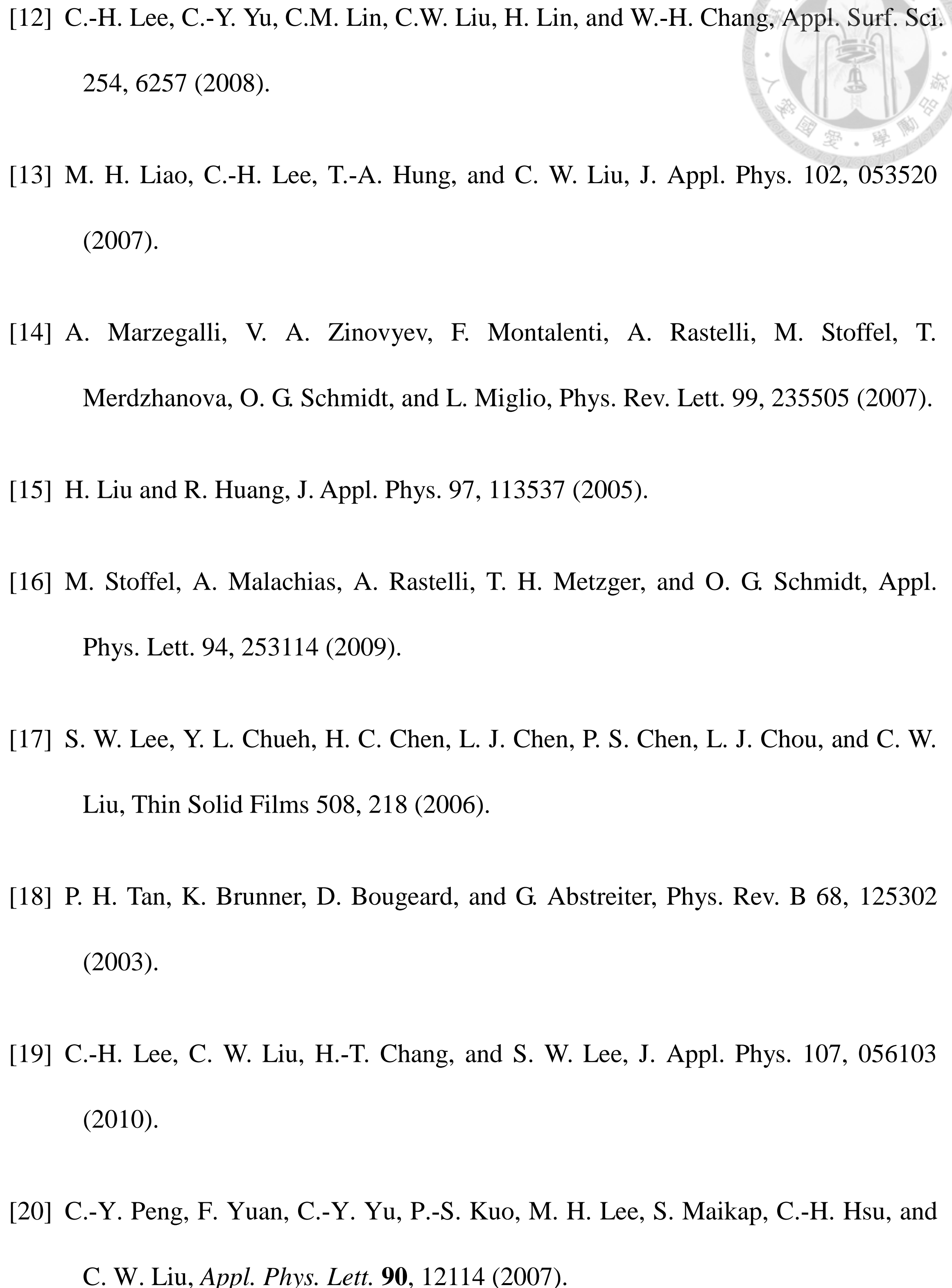

[12] C.-H. Lee, C.-Y. Yu, C.M. Lin, C.W. Liu, H. Lin, and W.-H. Chang, Appl. Surf. Sci. 254, 6257 (2008).

[13] M. H. Liao, C.-H. Lee, T.-A. Hung, and C. W. Liu, J. Appl. Phys. 102, 053520 (2007).

[14] A. Marzegalli, V. A. Zinovyev, F. Montalenti, A. Rastelli, M. Stoffel, T. Merdzhanova, O. G. Schmidt, and L. Miglio, Phys. Rev. Lett. 99, 235505 (2007).

[15] H. Liu and R. Huang, J. Appl. Phys. 97, 113537 (2005).

[16] M. Stoffel, A. Malachias, A. Rastelli, T. H. Metzger, and O. G. Schmidt, Appl. Phys. Lett. 94, 253114 (2009).

[17] S. W. Lee, Y. L. Chueh, H. C. Chen, L. J. Chen, P. S. Chen, L. J. Chou, and C. W. Liu, Thin Solid Films 508, 218 (2006).

[18] P. H. Tan, K. Brunner, D. Bougeard, and G. Abstreiter, Phys. Rev. B 68, 125302 (2003).

[19] C.-H. Lee, C. W. Liu, H.-T. Chang, and S. W. Lee, J. Appl. Phys. 107, 056103 (2010).

[20] C.-Y. Peng, F. Yuan, C.-Y. Yu, P.-S. Kuo, M. H. Lee, S. Maikap, C.-H. Hsu, and C. W. Liu, *Appl. Phys. Lett.* **90**, 12114 (2007).

Chapter 3

A Transition from Three to Two Dimensional Si growth on Ge (100) substrate

3.1 Introduction

SiGe quantum wells (QWs) [1, 2] and quantum dots (QDs) [3, 4] have drawn much attention in the applications of nanoelectronics and optoelectronics. The three dimension growth mode, Stranski-Krastanov (SK) growth mechanism, has been well-known to dominant the SiGe epitaxial growth on Si substrate [5, 6]. A few monolayers of Si directly grown on Ge has been investigated to reduce the surface roughness of the Ge p-channel metal-insulator-semiconductor field effect transistor [7,8]. Moreover, a 10 nm doped epi-Si-passivation layer, which can eliminate Fermi level pinning, has also been demonstrated above the Ge substrate to reduce the contact resistivity [9]. However, only limit literatures have discussed about the growth mechanism of Si on Ge growth. The dot growth of 4~20 monolayer of Si on Ge(001) by molecular beam epitaxy (MBE) system [10] was studied over a wide range of growth

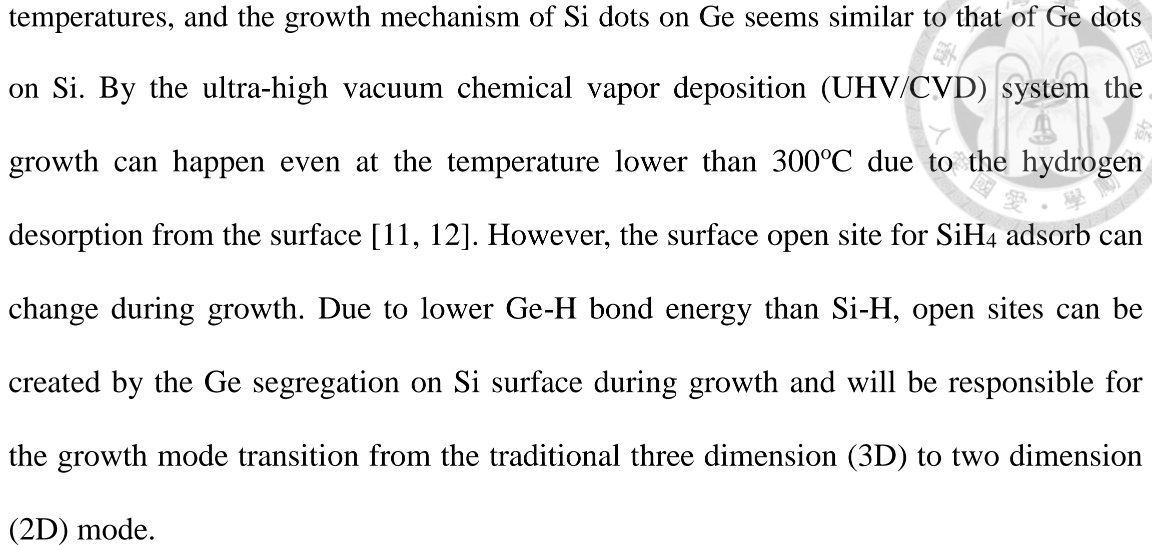

temperatures, and the growth mechanism of Si dots on Ge seems similar to that of Ge dots on Si. By the ultra-high vacuum chemical vapor deposition (UHV/CVD) system the growth can happen even at the temperature lower than 300°C due to the hydrogen desorption from the surface [11, 12]. However, the surface open site for SiH_4 adsorb can change during growth. Due to lower Ge-H bond energy than Si-H, open sites can be created by the Ge segregation on Si surface during growth and will be responsible for the growth mode transition from the traditional three dimension (3D) to two dimension (2D) mode.

In this chapter, the transition from 3D to 2D growth for Si on Ge, which is different from the Ge on Si case, was observed for the first time by the atomic force microscopy (AFM) and the cross-sectional transmission electron microscopy (TEM). The strain in Si film on Ge was analyzed through the Raman and x-ray diffraction (XRD) using synchrotron radiation source.

3.2 Experiments

All the samples were grown by the UHV/CVD system at 550°C. The base pressure was ~10^{-9} torr. Pure silane (SiH_4) at a fixed 100 sccm flow was used for Si growth. The Si is directly grown on Ge without the buffer layer. The Si dots grown at 550°C are shown in Fig. 3-1 with the dot density of ~ 7×10^8 cm^{-2} and the surface root-mean-square (RMS) roughness of ~1.21 nm. The much lower density as compared to the Ge dots on Si (~10^{10} cm^{-2}) probably due to the impedance of three-dimensional dot growth by the tensile strain [13, 14].

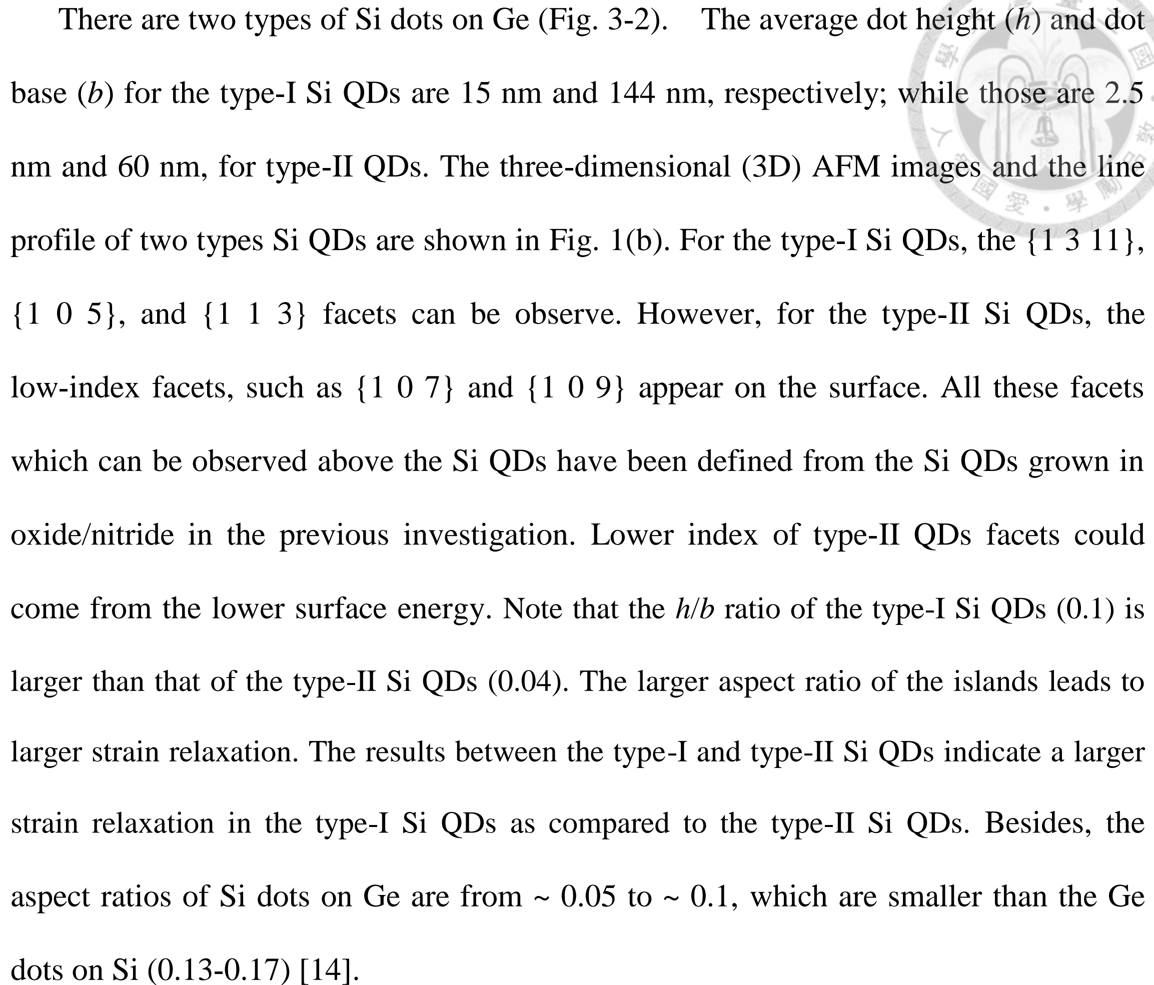

There are two types of Si dots on Ge (Fig. 3-2). The average dot height (*h*) and dot base (*b*) for the type-I Si QDs are 15 nm and 144 nm, respectively; while those are 2.5 nm and 60 nm, for type-II QDs. The three-dimensional (3D) AFM images and the line profile of two types Si QDs are shown in Fig. 1(b). For the type-I Si QDs, the {1 3 11}, {1 0 5}, and {1 1 3} facets can be observe. However, for the type-II Si QDs, the low-index facets, such as {1 0 7} and {1 0 9} appear on the surface. All these facets which can be observed above the Si QDs have been defined from the Si QDs grown in oxide/nitride in the previous investigation. Lower index of type-II QDs facets could come from the lower surface energy. Note that the *h*/*b* ratio of the type-I Si QDs (0.1) is larger than that of the type-II Si QDs (0.04). The larger aspect ratio of the islands leads to larger strain relaxation. The results between the type-I and type-II Si QDs indicate a larger strain relaxation in the type-I Si QDs as compared to the type-II Si QDs. Besides, the aspect ratios of Si dots on Ge are from ~ 0.05 to ~ 0.1, which are smaller than the Ge dots on Si (0.13-0.17) [14].

The cross sectional TEM image of the type-II Si dot having the aspect ratio of ~ 0.05 is shown in Fig, 3-3. The wetting layer of the Si dot is ~5 nm, which is thicker than that of the Ge dot on Si (~1 nm). The thicker wetting layer of Si dot on Ge was also report in the ref.10. The observed thicker wetting is probably due to the tensile strain [13]. It is evident that the SK mode growth is still valid for the tensile strained Si growth on Ge (001) [10].

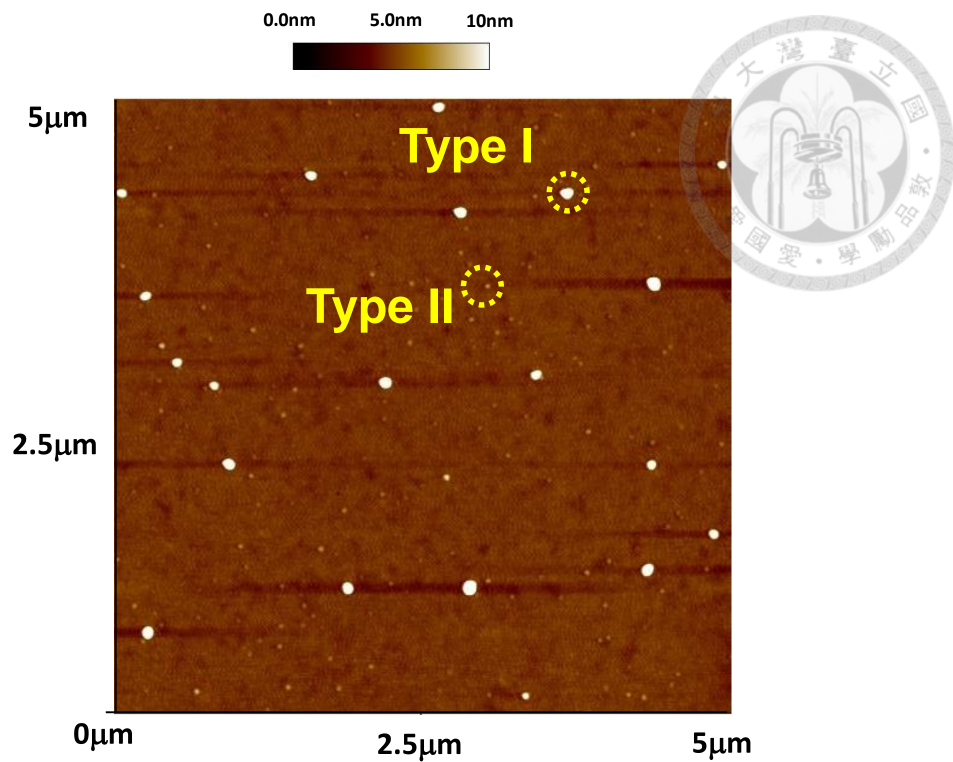

Fig.3-1 The AFM images (5μm × 5μm) of Si QDs grown on Ge substrate. Two types of Si QDs (indicated by dash circles) can be observed.

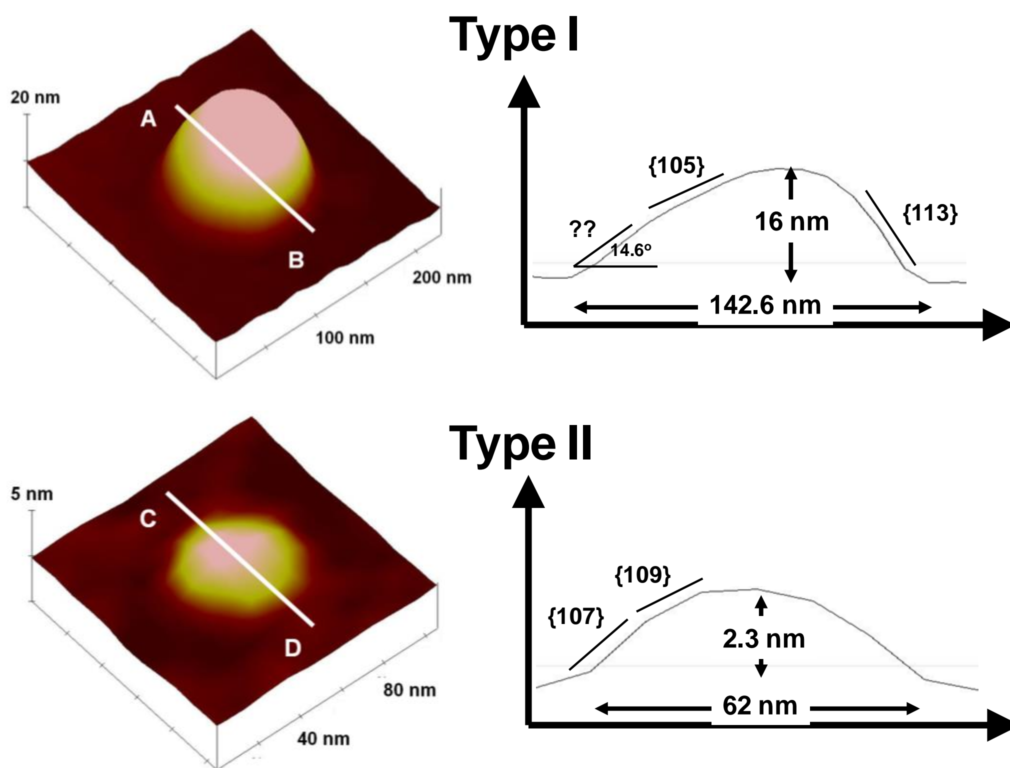

Fig.3-2 The 3D AFM images and line profiles of the type I and type II Si QDs shown in Fig.3-1.

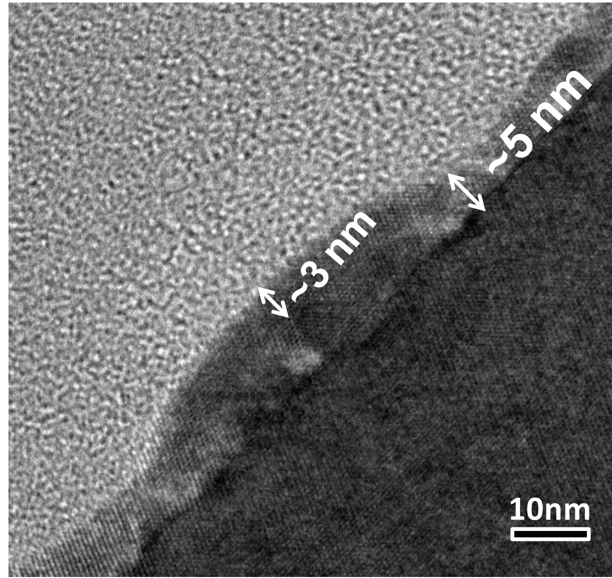

Fig.3-3 The cross-sectional TEM image of a type II Si dot with the wetting layer of ~5 nm and the dot height of ~3 nm.

3.3 Transition from 3D to 2D Growth on Ge(001)

The transition from 2D to 3D growth of Ge on Si(001) is well-known as SK mode growth. The Ge islands continue to grow with increasing growth time and coalescences with other islands [21, 22]. The SK mode growth is still valid in the Si on Ge(001) growth [10]. Two types Si QDs, which have been discussed before, were observed when the Si film was deposited for 7.5 min (Fig. 3-2) with the wetting layer thickness of ~5 nm (Fig. 3-3). However, while the Si thickness increases, the surface morphology changes. No dots were observed on the surface with the Si thickness of ~11 nm (Fig.3-4). Instead, the smooth surfaces (RMS roughness ~0.91 nm) with scattered ring-like structures were observed on the surface (Fig, 3-5 (a)). The density of the ring-like structure is ~ 2×10^7

cm^{-2}.

The Fig.3-6 shows the 3D AFM image and the line profile of the ring-like structure. The ring average width and depth is ~129.4nm and ~1nm, respectively. For Ge growth on Si, the ring could be due to the SiO_2 particles from other's work [15] or surface diffusion of adatoms to relatively strain-free regions from our early work [16].

For Si growth on Ge, since the strain is almost relaxed at Si dot facet on Ge substrate [17], the Si adatoms can diffuse to relatively strain-free facet regions and aggregate on the facet of the Si dot to form the ring-like structure in this work. Moreover, no oxide at Si/Ge interface was detected by the EDS. The three-dimensional to two-dimensional transition of Si growth would not be expected if there was some oxide on the initial Ge surface. In the TEM image (Fig. 3-4), it is found that the dots disappeared after the growth of ~ 11 nm Si film. Due to the small aspect ratio (~0.007) of the ring-like structure, it is difficult to observe the ring-like structure on the cross sectional TEM image. Note that some dislocations were observed in the Si film which can relax tensile strain. The average width of the ring structures is smaller than the base width of the type-I Si QDs. Moreover, the ring density of 2×10^7 cm^{-2} is similar to the dot density of the type-I Si QDs. Based on these results, the ring-like structures in Fig. 3-6 may probably come from the type-I Si QDs. The specific growth mechanism for the Si directly grown on Ge should be responsible for this.

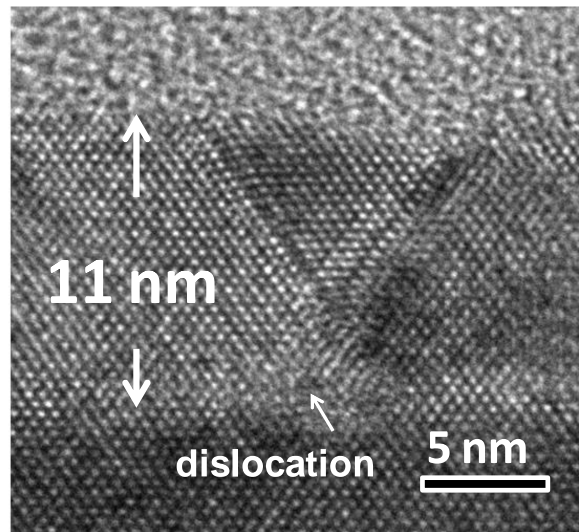

Fig.3-4 The cross-sectional TEM image of the ~11 nm Si on Ge. Note the dislocation appears to relax strain.

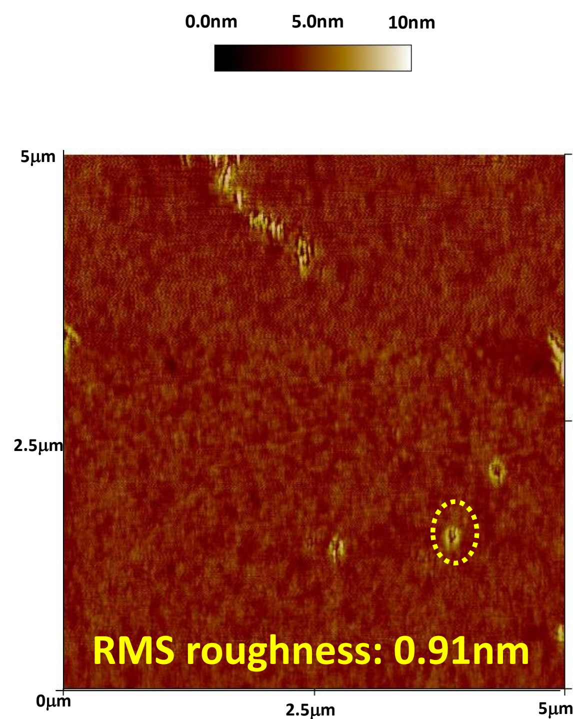

Fig.3-5 The AFM image of the ~11 nm Si film with ring-like structures on the surface.

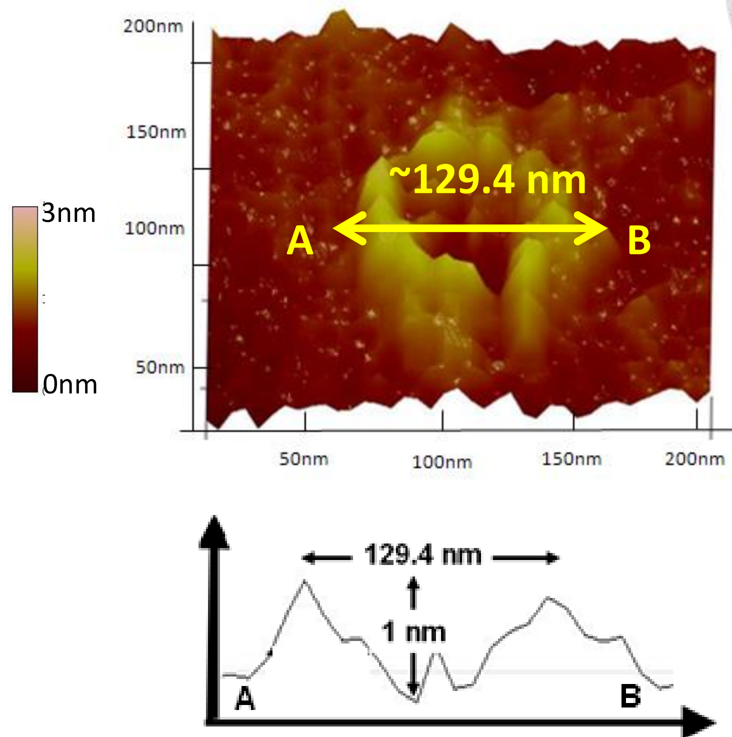

Fig.3-6 The 3D AFM images and line profile of the ring-like structure. The average width and depth is ~129.4 nm and ~1nm, respectively.

3.4 Growth Model of Si growth on Ge(001)

The Ge and Si atoms have naturally 4.2% lattice mismatch, and the Ge film would under compressive strain when grown on the Si substrate. The SK growth mechanism should dominate the Ge on Si growth. When the Ge film becomes thicker than the critical thickness, the strain in the Ge film tends to relax, and the 3D islands will form on the surface. The Ge layers could transform into SiGe alloys due to Si/Ge.

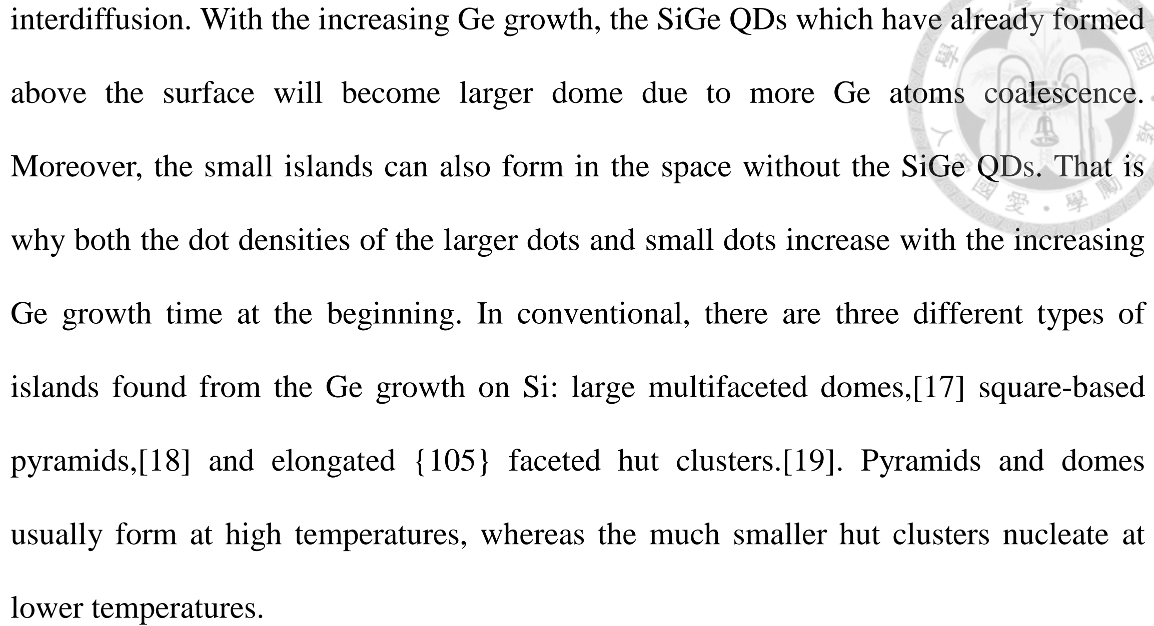

interdiffusion. With the increasing Ge growth, the SiGe QDs which have already formed above the surface will become larger dome due to more Ge atoms coalescence. Moreover, the small islands can also form in the space without the SiGe QDs. That is why both the dot densities of the larger dots and small dots increase with the increasing Ge growth time at the beginning. In conventional, there are three different types of islands found from the Ge growth on Si: large multifaceted domes,[17] square-based pyramids,[18] and elongated {105} faceted hut clusters.[19]. Pyramids and domes usually form at high temperatures, whereas the much smaller hut clusters nucleate at lower temperatures.

When the SiGe QDs become bigger, there would be less space without SiGe QDs. That is why the dot density would become lower after even longer SiGe QDs growth. The dot density of the large dots may increase, but that of the small dots would drop with the increasing Ge growth time. The dot density ratio between the large dots and small dots may thus increases. From previous works [18]. the SiGe dot density is ~8×10^8 cm^{-2}, while the average dot height and dot base width for the SiGe QDs are 16 nm and 124 nm, respectively. The dot density ratio between the large dot ($h/b > 0.133$) and small dot ($h/b < 0.1$) is ~0.6. When the growth time of Ge on Si increases to 20 min, the dot density slightly increase to ~1.1×10^9cm^{-2}, and the average dot height and dot base width for the SiGe QDs increase to 22 nm and 154 nm, respectively. Both the dot density and the dot size increase with the increasing Ge growth time. Moreover, the dot density ratio between the large dots and small dots becomes ~0.9. More large dots appear on the surface as compared to the small dots after the further Ge growth.

From previous work about SiGe dots grown on different orientations Si substrate, the square-based pyramids by Ge growth on Si(001) at 550°C (Fig.3-7(a)). It is found

that the shape of the pyramids depends on the surface orientation. The shape is hexagonal for pyramids on Si(110) (Fig.3-7(b))and triangle for pyramids on Si(111) (Fig.3-7(c)), respectively[20]. The shapes of epitaxially grown islands usually follow the symmetry of underlying substrate [21].

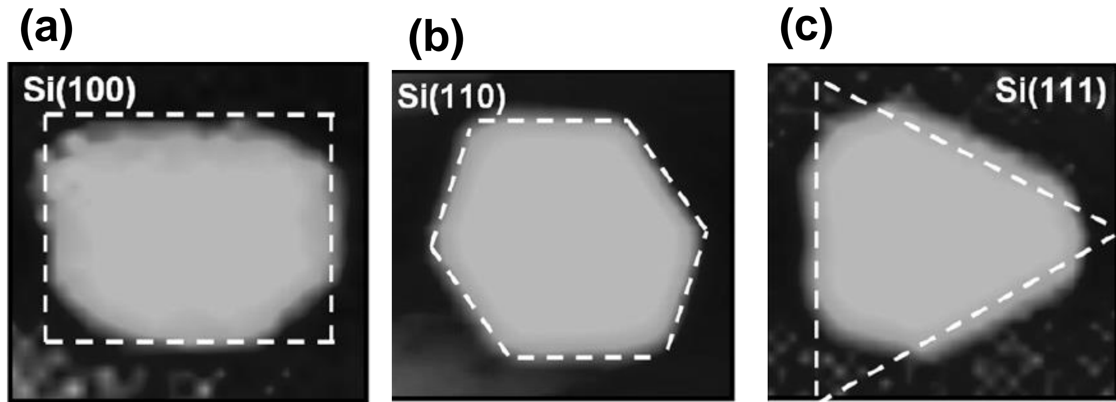

Fig.3-7 The AFM SiGe pyramid images on (a) Si(001) (b) Si(110), and (c) Si(111).

For the growth of Si growth on Ge, the growth rate enhancement on the wetting layer plays a crucial role in the growth mode transition from 3D to 2D. The Ge can segregate on Si surface with the activation energy ~ 1.4eV [22]. The Ge segregation in our samples is observed by the energy dispersive x-ray spectroscopy (EDS) measurement. For the Si dot grown on Ge, the Ge content at the wetting layer surface is ~ 37%, which is much higher than that at the dot (~10%) (Fig. 3-8).

Since the desorption energy of hydrogen from Ge (100) surface (~1.51eV) is lower than that from Si (100) surface (~2.05eV), the hydrogen desorption increases due to the increasing Ge coverage on the surface [23]. From the EDS, there is more Ge segregation

on the wetting layer (~5 nm) than on peak of Si dots for Si growth on Ge surface after the three-dimensional dot growth, more open sites can be created on dot peak than on wetting layer surface. It is known that not only Si atom adsorption, but also the hydrogen desorption is the crucial role for Si growth, which will be discussed with detail in Chapter 4. Two open sites are needed for one Si atom adsorption. Therefore more Ge segregation can yield a higher Si growth rate on the Si wetting layer than on the Si dots [24]. Higher subsequent Si growth rate at the wetting layer than the Si dots leads to the transition of three-dimensional Si dot growth to the two-dimensional Si film growth (Fig. 3-9).

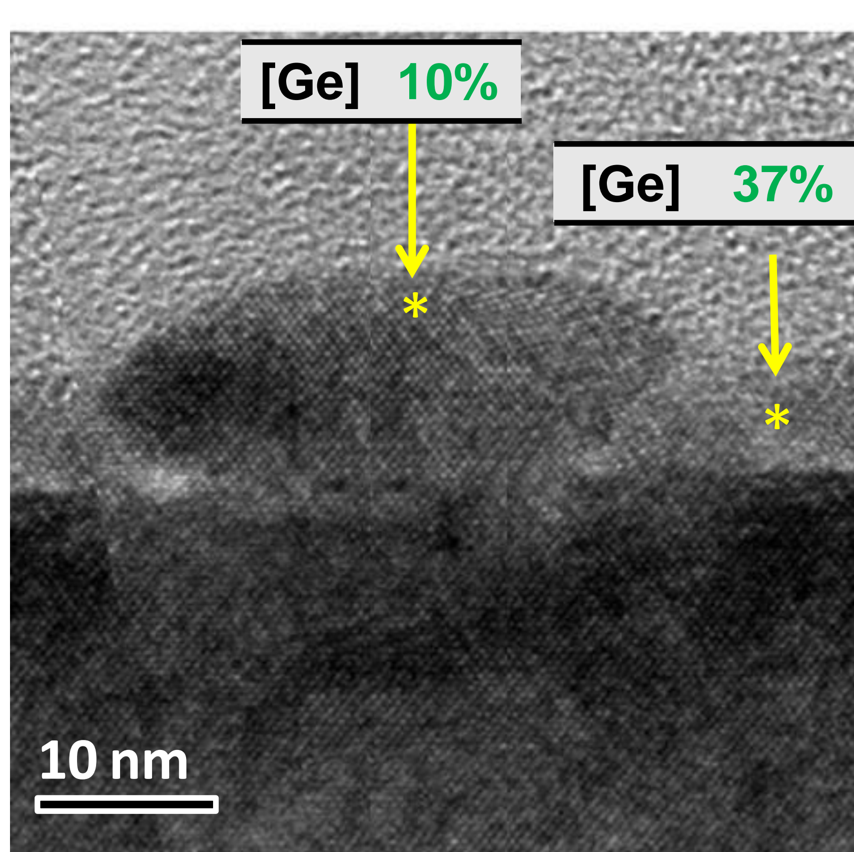

Fig.3-8 The EDS measurement for a Si dot on Ge. Note the Ge content is more on the wetting layer surface than on the QDs peak.

After ~15 nm growth of Si on Ge (Fig.3-10), neither Si dots nor ring-like structures were observed on the surface (Fig. 3-11). The surface RMS roughness is only about ~0.26 nm, which is similar to the bulk Ge substrate (~0.25 nm). From the EDS measurement (Fig. 3-11), the Ge content is ~47% near the bottom of “Si film” and gradually decreases to ~2% near the top due to Ge diffusion into Si. With the assistance of the enhanced growth rate at the initial Si wetting layer, the transition from 3D to 2D growth mode was observed for Si growth on Ge. For even thicker Si, less Ge content near the top is expected. Note that there have some dislocations found to relax tensile strain (Fig.3-10).

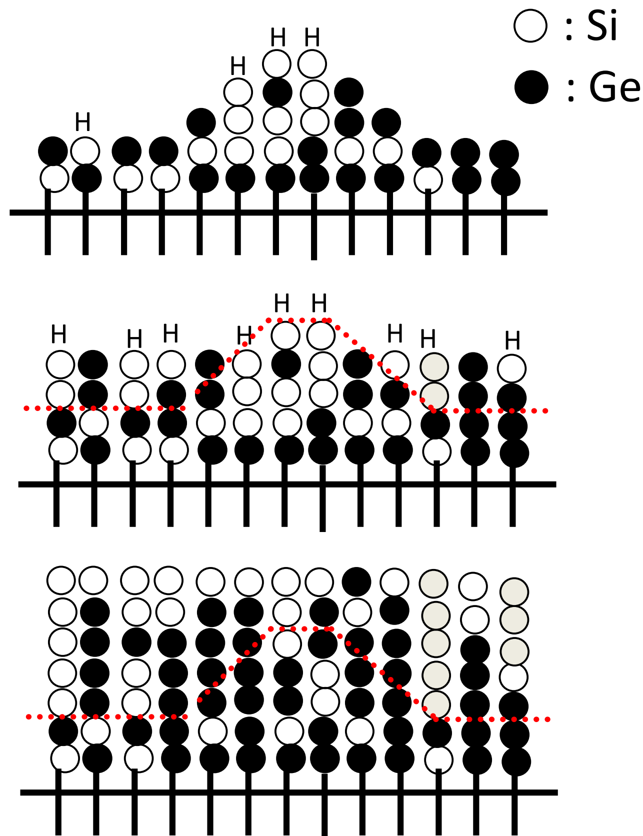

Fig.3-9 The growth model of Ge segregation effects of Si grown on Ge. Higher growth rate due to the more open sites on the wetting layer than on the dot leads to the smooth surface.

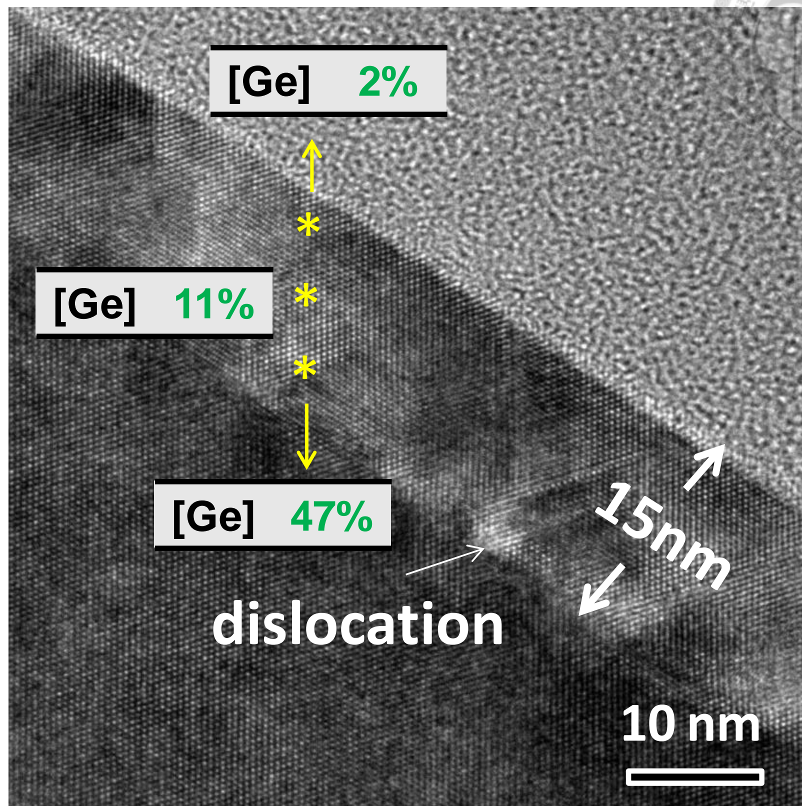

Fig.3-10 The cross-sectional TEM images of ~15 nm Si grown on Ge and Ge content by EDS measurement.

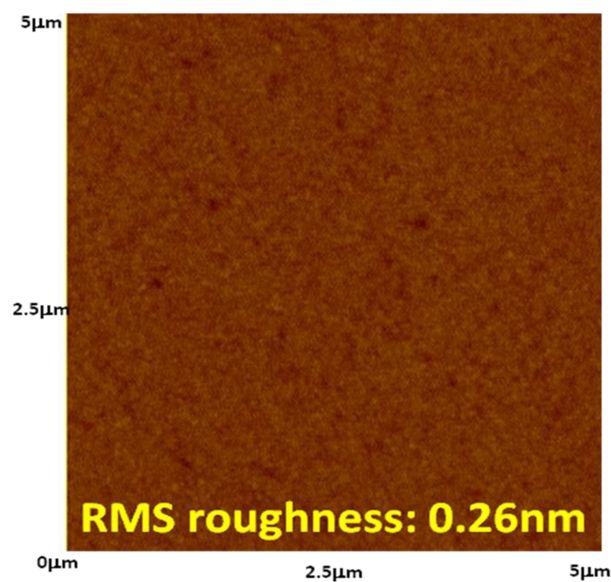

Fig.3-11 The AFM images of the ~15 nm Si grown on Ge. Note the surface roughness (~0.26 nm) is similar to bulk Ge.

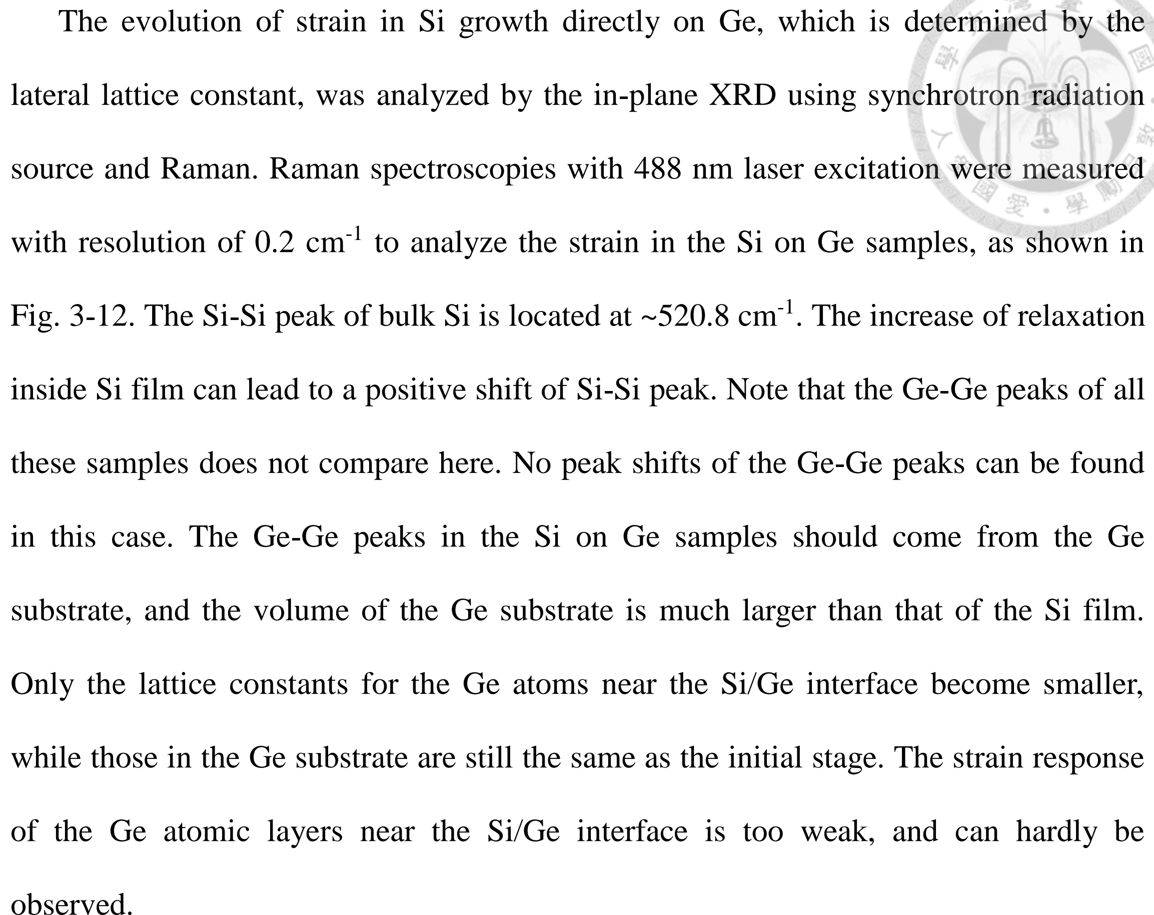

The evolution of strain in Si growth directly on Ge, which is determined by the lateral lattice constant, was analyzed by the in-plane XRD using synchrotron radiation source and Raman. Raman spectroscopies with 488 nm laser excitation were measured with resolution of 0.2 cm^{-1} to analyze the strain in the Si on Ge samples, as shown in Fig. 3-12. The Si-Si peak of bulk Si is located at ~520.8 cm^{-1}. The increase of relaxation inside Si film can lead to a positive shift of Si-Si peak. Note that the Ge-Ge peaks of all these samples does not compare here. No peak shifts of the Ge-Ge peaks can be found in this case. The Ge-Ge peaks in the Si on Ge samples should come from the Ge substrate, and the volume of the Ge substrate is much larger than that of the Si film. Only the lattice constants for the Ge atoms near the Si/Ge interface become smaller, while those in the Ge substrate are still the same as the initial stage. The strain response of the Ge atomic layers near the Si/Ge interface is too weak, and can hardly be observed.

For the Si-Si peak, when the Si QDs were initially grown, the Si-Si peak shift to a lower wave number (517.5 cm^{-1}) as compared to the bulk Si case (520.8 cm^{-1}), which means the Si film may suffer ~0.4% tensile strain in this stage. This can be easily understood since the formation of the Si dots can relax the strain inside the Si film (Fig.3-1). However, the formation of the Si dots can only partially relax the tensile strain and remain ~0.4% tensile strain in Si. With the increasing Si deposition (11 nm and 15 nm), the strain relaxations become even larger due to the appearance of threading dislocations in the Si layer (Fig. 3-4 and Fig. 3-10). The Si-Si peaks of these two samples show negative wave number shifts and moves much closer to the bulk Si peak.

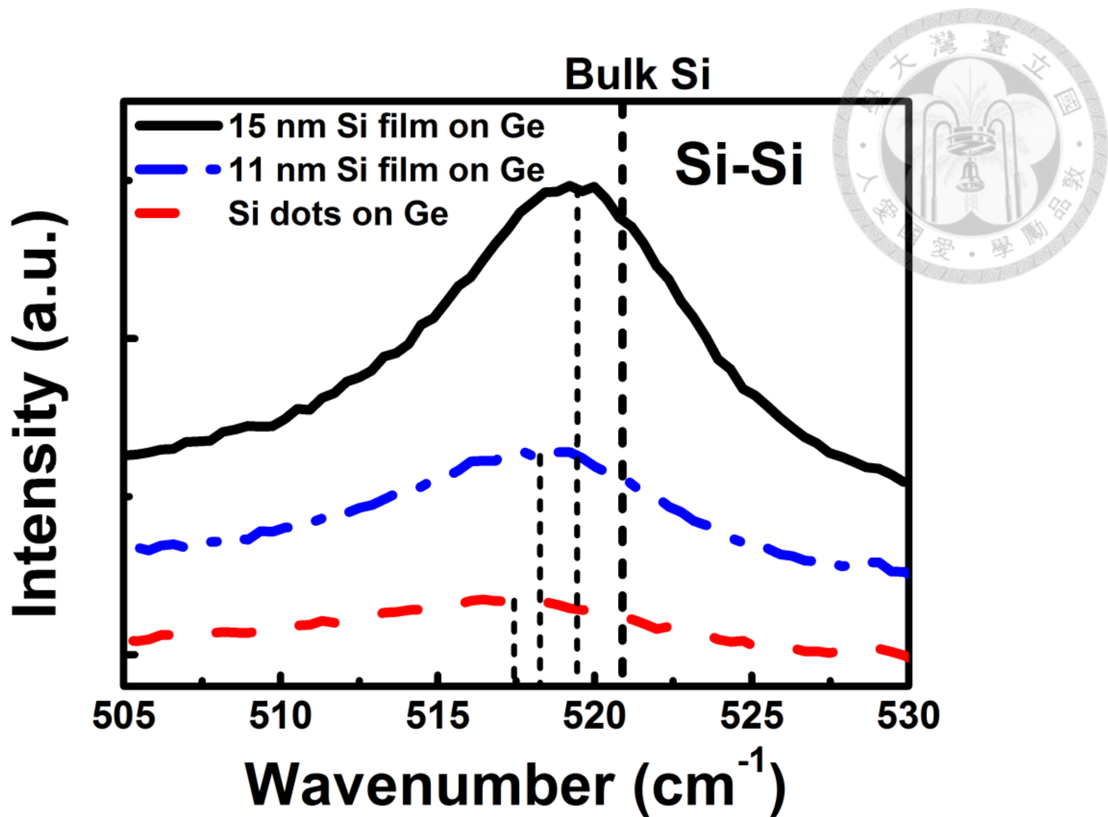

Fig.3-12 The Si-Si Raman spectroscopy of Si dots, 11 nm and 15 nm Si films grown on Ge. Positive shift of Si-Si wave number indicates the relaxed of tensile strain with increasing Si growth.

The XRD in-plane radial scans using synchrotron radiation source across Si (400) and Ge (400) peaks for the samples with Si dots and 15 nm Si on Ge are shown in Fig.3-13. The peak intensity of the Si peaks are too weak in the L-scan XRD and no information can be collect in this kind of measurement. That's why we choose the H-scan XRD to analyze the strain in the Si film. The peaks centered at 68°~69° are contributed from Si film, while the Ge(400) peaks contributed from Ge substrate can be observed at ~66° The decrease of lateral lattice parameter, as revealed by the positive shift of ~ 0.5° from the

Si dot sample to the 15 nm Si film sample, is attributed to the relaxation of lateral tensile strain. Note that the Si dots have the lateral tensile strain of ~ 0.34%. With the increasing Si thickness, the strain relaxation becomes significant. The 15 nm Si on Ge is almost relaxed. The dislocation in the 15 nm Si film (Fig.3-9) is responsible for the tensile strain relaxation.

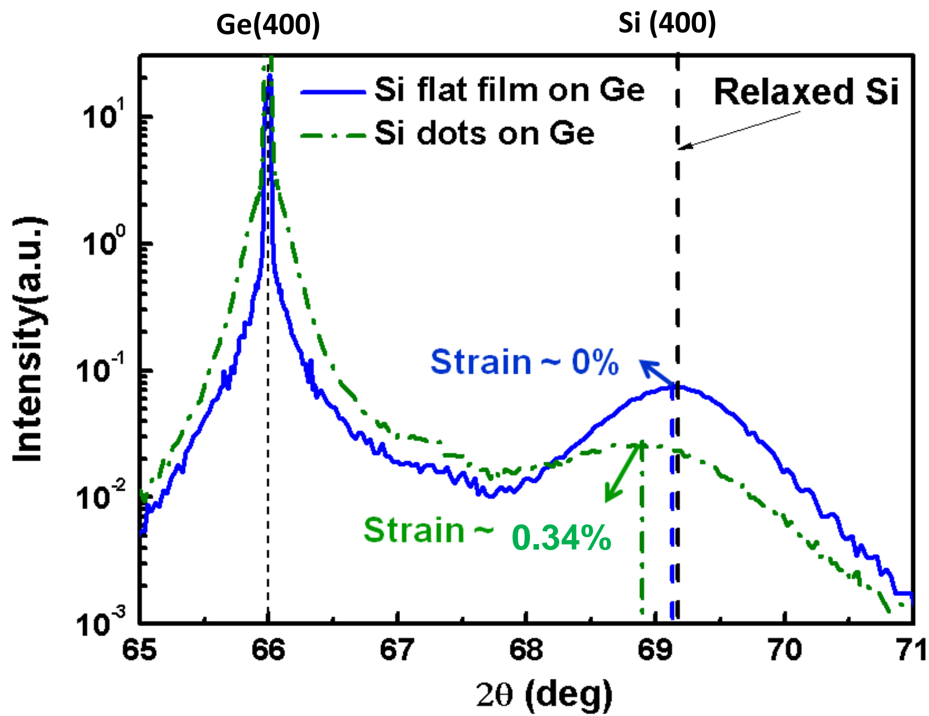

Fig.3-13 The (400) XRD in-plane radial scans of Si dots and 15 nm Si on Ge. Note the tensile strain is almost relaxed for 15 nm Si on Ge.

3.5 Summary

In summary, the transition of growth mode from three-dimensional to two-dimensional for Si growth on Ge has been observed for the first time. Growth rate dependence on the conditions of the growing surface is found. The enhanced Si growth rate due to the Ge segregation on the wetting layer leads to such transition. Smooth Si growth directly on Ge can be used for the applications of novel nanoelectronics and optoelectronics.

Reference:

[1] M. Myronov, K. Sawano, and Y. Shiraki, *Appl. Phys. Lett.*, **88**, 252115 (2006).

[2] P. Chaisakul, D. Marris-Morini, G. Isella, D. Chrastina, X. Le Roux, S. Edmond, E. Cassan, J. -R. Coudevylle, and L. Vivien, *Appl. Phys. Lett.*, **98**, 131112 (2011).

[3] M. Oehme, A. Karmous, M. Sarlija, J. Werner, E. Kasper, and J. Schulze, *Appl. Phys. Lett.*, **97**, 012101 (2010).

[4] M. Kolahdouz, A. A. Farniya, L. Di Benedetto, and H. H. Radamson, *Appl. Phys. Lett.*, **96**, 213516 (2010).

[5] Y. -W. Mo, D. E. Savage, B. S. Swartzentruber, and M. G. Lagally, *Phys. Rev. Lett.*, **65**, 1020 (1990).

[6] A. Sakai and Toru Tatsumi, *Phys. Rev. Lett.*, **71**, 4007 (1993).

[7] N. Taoka, W. Mizubayashi, Y. Morita, S. Migita, H. Ota, and S. Takagi, *Symp.on VLSI Tech.*, **T4B-4**, 80 (2009).

[8] C. –Y Peng, F. Yuan, C.-Y Yu, P. –S Kuo, S. Maikap, C.-H Hsu, and C. W. Liu, *Appl. Phys. Lett.* **90**, 12114 (2007).

[9] K. Martens, A. Firrincieli, R. Rooyackers, B. Vincent, R. Loo, S. Locorotondo, E. Rosseel, T. Vandeweyer, G. Hellings, B. De Jaeger, M. Meuris, P. Favia, H. Bender, B. Douhard, J. Delmotte, W. Vandervorst, E. Simoen, G. Jurczak, D.

Wouters, and J. A. Kittl, *Proceedings of Int. Electron Devices Meet.(IEDM) Tech. Dig.*, p.18.4.1 (2010).

[10] D. Pachinger, H. Groiss, H. Lichtenberger, G. Strangl, G. Hesser, and F. Schäffler, *Appl. Phys. Lett.*, **91**, 233106 (2007).

[11] D. A. Griitzmacher, T. O. Sedgwick, A. Powell, M. Tejwani, S. S. lyer, J. Cotte, and F. Cardone, *Appl. Phys. Lett.* , **63**, 2531 (1993).

[12] K. Nakajima, N. Hosaka, T. Hattori, and K. Kimura, *Nuclear Instruments and Methods in Physics Research B*, **190**, 587 (2002).

[13] Y. H. Xie, G. H. Glimer, C. Roland, P. J. Silverman, S. K. Buratto, J. Y., Cheng, E. A. Fitzgerald, A. R. Kortan, S. Schuppler, M. A. Marcus, and P. H. Citrin, *Phys. Rev. Lett.* , **73**, 3006, (1994).

[14] C.-H. Lee, C.-Y. Yu, C.M. Lin, C.W. Liu, H. Lin, and W.-H. Chang, *Appl. Sur. Sci.*, **254**, 6257, (2008).

[15] Qiming Li and Sang M. Han, *MRS Proc.*, 921, 0921-T02-04 (2006).

[16] S. W. Lee, L. J. Chen, P. S. Chen, M. -J. Tsai, C. W. Liu, T. Y. Chien, and C. T. Chia, *Appl. Phys. Lett.* **83**, 5283 (2003).

[17] J. A. Floro, G. A. Locadomo, E. Chason, L. B. Freund, M. Sinclair, R. D. Twesten, and R. Q. Hwang, Phys. Rev. Lett. 80, 4717 ,(1998).

[18] X. Deng, J. D. Weil, and M. Krishnamurthy, Phys. Rev. Lett. 80, 4721,(1998).

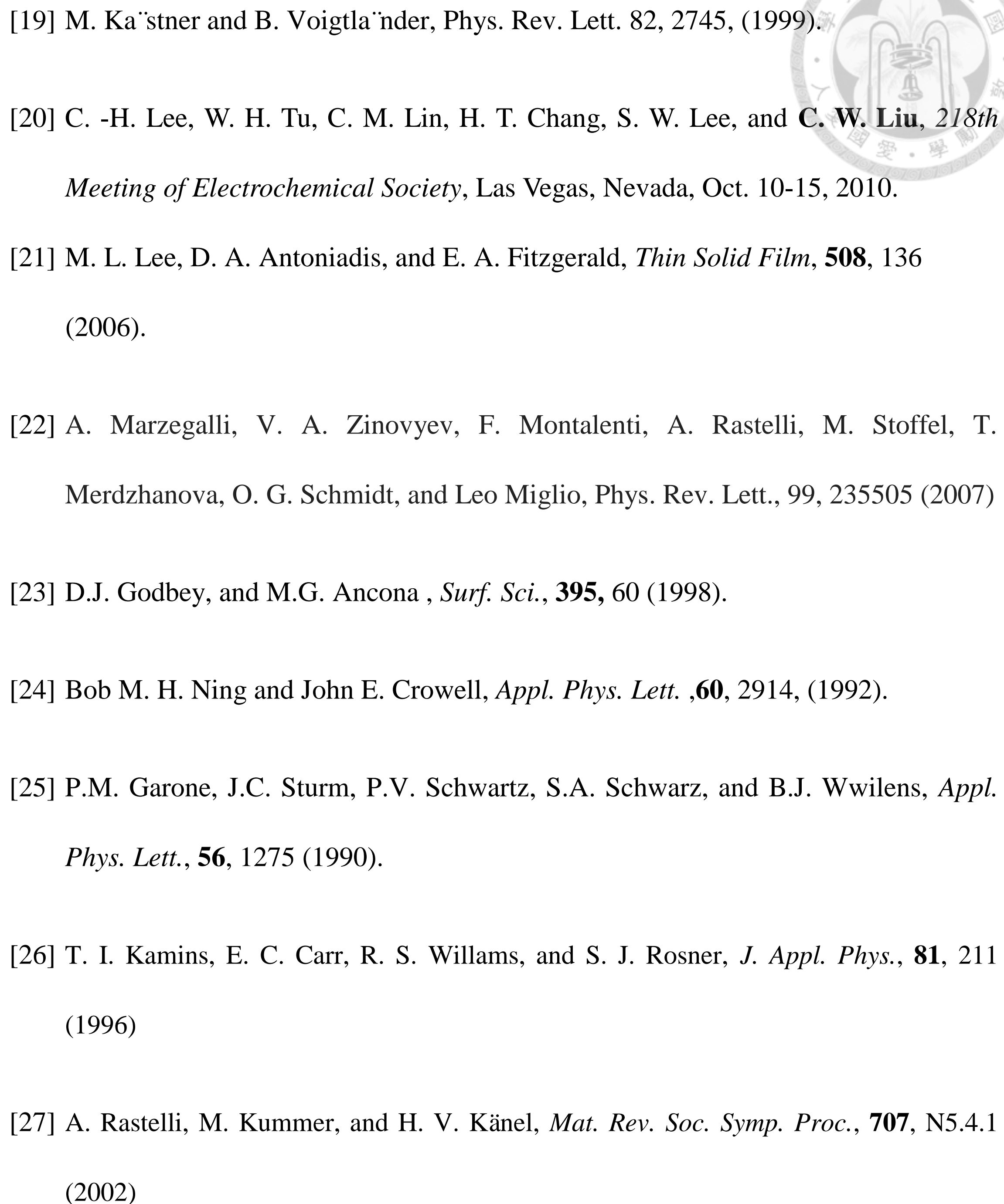

[19] M. Ka¨stner and B. Voigtla¨nder, Phys. Rev. Lett. 82, 2745, (1999).

[20] C. -H. Lee, W. H. Tu, C. M. Lin, H. T. Chang, S. W. Lee, and **C. W. Liu**, *218th Meeting of Electrochemical Society*, Las Vegas, Nevada, Oct. 10-15, 2010.

[21] M. L. Lee, D. A. Antoniadis, and E. A. Fitzgerald, *Thin Solid Film*, **508**, 136 (2006).

[22] A. Marzegalli, V. A. Zinovyev, F. Montalenti, A. Rastelli, M. Stoffel, T. Merdzhanova, O. G. Schmidt, and Leo Miglio, Phys. Rev. Lett., 99, 235505 (2007)

[23] D.J. Godbey, and M.G. Ancona , *Surf. Sci.*, **395,** 60 (1998).

[24] Bob M. H. Ning and John E. Crowell, *Appl. Phys. Lett.* ,**60**, 2914, (1992).

[25] P.M. Garone, J.C. Sturm, P.V. Schwartz, S.A. Schwarz, and B.J. Wwilens, *Appl. Phys. Lett.*, **56**, 1275 (1990).

[26] T. I. Kamins, E. C. Carr, R. S. Willams, and S. J. Rosner, *J. Appl. Phys.*, **81**, 211 (1996)

[27] A. Rastelli, M. Kummer, and H. V. Känel, *Mat. Rev. Soc. Symp. Proc.*, **707**, N5.4.1 (2002)

Chapter 4

Growth Rate of SiGe and Ge on Si(001)

4.1 Growth Model by Chemical Vapor Deposition

Silane undertakes the following reactions for CVD growth in ultra-high vacuum (UHV) conditions (clean silicon surface) [1]:

A. $SiH_{4(g)} \Rightarrow Si_{(s)} + 2H_{2(g)}$ [total mechanism]

B. $SiH_{4\ (g)} + 2\ (*) \Rightarrow H^* + SiH_{3\ (ad)}$ [silane adsorption]

C. $SiH_{3\ (ad)} + (*) \Rightarrow H^* + SiH_{2\ (ad)}$ [H decomposition]

D. $2SiH_{2\ (ad)} \Rightarrow H_{2\ (g)} + 2SiH_{\ (ad)}$ [H decomposition, H desorption]

E. $2SiH_{\ (ad)} \Rightarrow H_{2\ (g)} + 2\ Si_{\ (ad)}$ [H decomposition, H desorption]

F. $2H_{\ (ad)} \Rightarrow H_{2\ (g)} + 2\ (*)$ [H desorption]

G. $Si_{\ (ad)} \Rightarrow Si_{\ (s)} + (*)$ [surface migration]

where (*) denotes an open site (a dangling bond) for adsorption, (g) represents gas phase, H* is an adsorbed surface hydrogen atom, and (ad) represents an adsorbed species. Equation (A) is the overall surface reaction for the growth process with silane. Equations (B) through (G) are the individual reaction steps. If we balance Equations (B)-(G) (divide Equations (D) and (E) by 2) we end up with the original reaction (Equation (A)). Equation (B) is the silane adsorption step. Equations (B)-(E) are the hydrogen decomposition steps. Equation (F) is the open site generation step via mono-hydride desorption. Equation (G) is the surface diffusion step for silicon.

According to Gates, [1], [2], and [3], Equation (b) is the rate-limiting step when there are open sites available (i.e. the growth rate is limited by silane ($SiH_4(g)$) adsorption, controlled by the number of open sites (*)). From the Fig. 4-1 shown below, illustrates Equation (B) describing how silane adsorbs onto the hydrogenated 2x1 reconstructed silicon surface. In order for silane to adsorb on the surface, it also requires two adjacent open sites to be generated on the growing surface. In Fig. 4-1, only the adsorption on two adjacent open sites from separate dimer rows is shown. The silane adsorption can occur on any two adjacent open sites. Silane dissociatively adsorbs, splitting a Si-H bond and forming SiH_3 on one site and an H on another open site. At the same silane partial pressure; the open site fraction is significantly less in a hydrogen

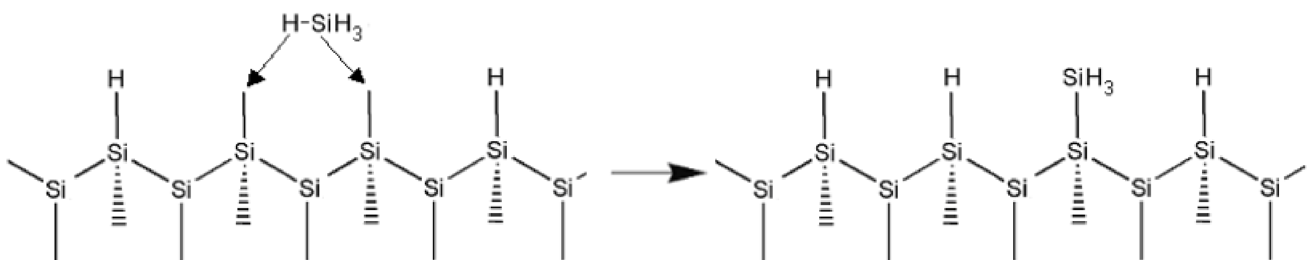

Fig.4-1 The side view of silane adsorption reaction on a (2 x 1) reconstructed silicon surface. The dashed triangle underneath the silicon surface represents the reconstruction of the surface silicon atoms in/out of the plane of the figure

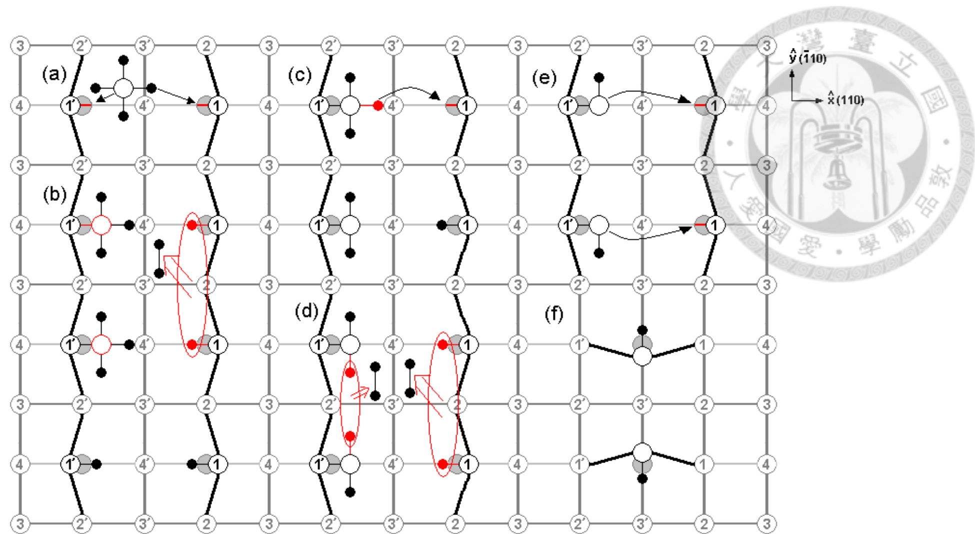

Fig.4-2 Top view of the adsorption process of silane onto a Si:H (100) (2x1) reconstructed surface based on references [1],[3]. Red circles indicate the change, and a red line indicates an open surface site.

Fig. 4-2 below illustrates the adsorption steps for silane on a hydrogenated 2x1 reconstructed silicon surface which is established by S.M. Gates. Equations (B) to (D) and Equation (F) are illustrated in the Fig. 4-2. Note that in the Fig. 4-2, the adsorption of silane is shown along the dimer row as opposed to adsorbing on two separate dimer rows in Fig. 4-1. (a) illustrates the adsorption of silane as a SiH_3 and a hydrogen atom (Equation (B)). (b) Depicts hydrogen desorption (Equation (F)) to form two open sites for (c) the SiH_3 to split into SiH_2 (Equation (C)). Another two hydrogen desorption step occurs in (d) to create two open sites and for SiH_2 to be reduced to SiH (Equation (d)). Step (e) shows the SiH bonding with its two nearest neighboring silicon atoms (i.e. incorporated into the solid) and the new reconstruction (f) on the surface. Therefore, not only the adsorption of the precursor, but also the open sites created by hydrogen desorption on the surface are the crucial rules of the dissociated precursor molecules adsorption for Si growth. To realize the effects of carrier gas, precursor on hydrogen desorption and precursor adsorption, the SiGe and Ge grown on Si(100) by ASM Epsilon RTCVD are discuss below.

4.2 SiGe Growth and Characteristics on Si(001)

The applications of SiGe film as high mobility channel and stressor are discussed in chapter 1. Having higher Ge% can have more benefits for the channel and stressor. The SiGe films using liquid dichlorosilane ($SiCl_2H_2$, DCS) for Si source and 10% germane (GeH_4) in H_2 as Ge source are studied here. The growth temperature and pressure is 650°C and 80 torr, respectively. To minimize the contamination, wafer is directly loaded into the load-lock chamber after the 10% HF dips with the subsequent 1100°C prebaking in H_2 for 2 minutes. H_2 with the flow rate at 20 standard liter per minute is fixed in the whole growth process. Having better epitaxial surface than wafer, the ~100 nm Si buffer layer was grown firstly on Si wafers. The SiGe layer using gas flows of DCS fixed at 130sccm and GeH_4 are 25~250sccm, respectively, to grow SiGe with increasing Ge content. The morphology and thickness are observed by atomic force microscope (AFM) and the cross-sectional TEM images. Besides, the quality and composition are determined by x-ray diffraction (XRD) and photoluminescence (PL) at ~60K taken in liquid nitrogen. The excitation source is 671nm laser with power of 2W/cm^2.

The Ω-2θ scans around the (004) XRD which uses Cu Kα_1 radiation with wave length at 0.15406 nm and is selected by a Ge (220) four reflection channel-cut monochromator is used to study the Ge content of SiGe films. The incident beam provides a beam having a divergence in the scattering plane (00L) of about 12 arc sec. With the X'pert epitaxy by Philips simulator, the fully strained $Si_{1-x}Ge_x$ with x~0.27 is demonstrated in the Fig. 4-3. The lattice constant of Ge and Si for simulation is 0.5657nm and 0.5431nm, respectively. And the Possion ration for simulation is 0.270 and 0.279 for Ge and Si, respectively.

The PL spectrum using 671nm laser in Fig.4-4 (a) shows the strongest SiGe peak with no-phonon (NP) peak and transverse optical (TO) peak at lower energy. The NP peak is attributed to lattice disorder (mainly alloy fluctuations) and relaxes the momentum conservation requirement. The TO phonon replicas relates to Si-Si, Si-Ge, and Ge-Ge vibrations. Using an electron-hole plasma (EHP) model [4], bandgap of extracted SiGe from the cut-off NP peak of out sample is 901meV.

The formation of the EHP phase is discussed below. At low carrier injection, when an electron in the valence band is excited into the conduction band, the free electron and hole are bound together through coulomb attractive forces and exist in the excitonic phase [11] [12]. As the carrier concentration increases above $(3\pm1)\times10^{16}$ cm^{-3} according to the Mott transition [13], due to the screening effects among the electrons and holes, the bound exciton dissociates into the electron hole plasma. The spectral distribution of the infrared radiation is considered as the result of the electron-hole recombination in the degenerate non-equilibrium plasma. We can thus fit the luminescence spectra by a convolution of the electron and hole distribution functions. The spectra from the EHP can be modeled with the equation shown below:

$$I(hv) = I_0 \int_0^{hv-E_g} dE \cdot D_e(E) \cdot D_h(hv - E_g - E) \cdot f_e(E, E_{fn}, T) \cdot f_e(hv - E_g - E, E_{fp}, T) \quad (4.1)$$

where I_0 is relative intensity, D_e and D_h are the density of states of electron and hole, E_{fn} and E_{fp} are the quasi-Fermi energies, h is the energy of the emitted photon, T is the temperature, E_g is the low-energy edge of the spectrum, f_e (E, E_{fn}, T) is the Fermi-Dirac distribution of electrons and f_h(hv -E_g-E, E_{fp}, T) is the Fermi-Dirac distribution of holes. The quasi-fermi energy of electrons and holes is defined to be zero at the conduction

band minimum and valence band maximum, respectively, and is positive when deeper into the bands. The Fermi-Dirac distribution for electron and holes are shown below:

$$f_e(\mathrm{E}, E_{fn}, \mathrm{T}) = \frac{1}{1 + \mathrm{e}^{\frac{E - E_{fn}}{KT}}}$$

$$f_h(\mathrm{hv} - E_g - \mathrm{E}, E_{fp}, \mathrm{T}) = \frac{1}{1 + \mathrm{e}^{\frac{hv - E_g - E - E_{fp}}{KT}}} \quad (4.2)$$

The density of states has a three dimensional distribution for both holes and electrons for PL measurements, is due to the localization in the accumulation layer. Taking the 3D density of states for the electrons and holes, respectively, are given below:

$$D_e(\mathrm{E}) = \frac{8\pi\sqrt{2}}{h^3} m_n^{\frac{3}{2}} \sqrt{E}$$

$$D_h(\mathrm{E}) = \frac{8\pi\sqrt{2}}{h^3} m_p^{\frac{3}{2}} \sqrt{hv - E_g - E} \quad (3.3)$$

Substituting the above equations into the EHP equation would lead to the EHP model for PL measurements. The theoretical spectrum from the EHP model is a convolution between the electron and the hole population. Based on the Bean's calculation about the function of Ge content on strained SiGe energy bandgap [5], the extracted Ge content is also ~28%. Higher Ge content estimated from PL than from XRD could come from the fully strain estimation of SiGe. Partial relaxation could make higher Ge content estimated from XRD.

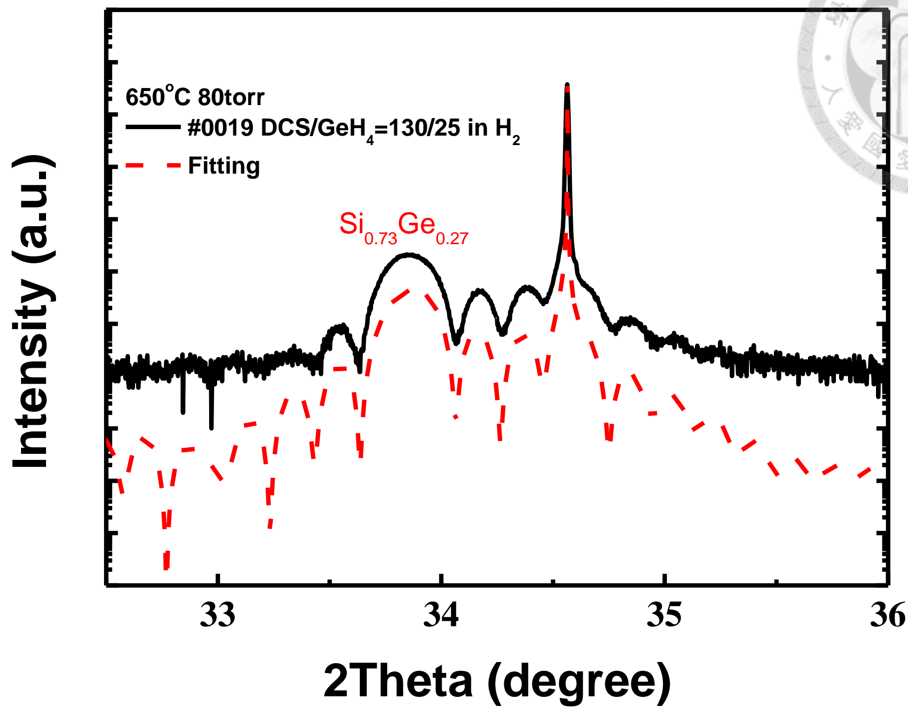

Fig.4-3 The Ω-2θ XRD of SiGe on Si(001). Note the Ge content is 27% under the fully strain fitting.

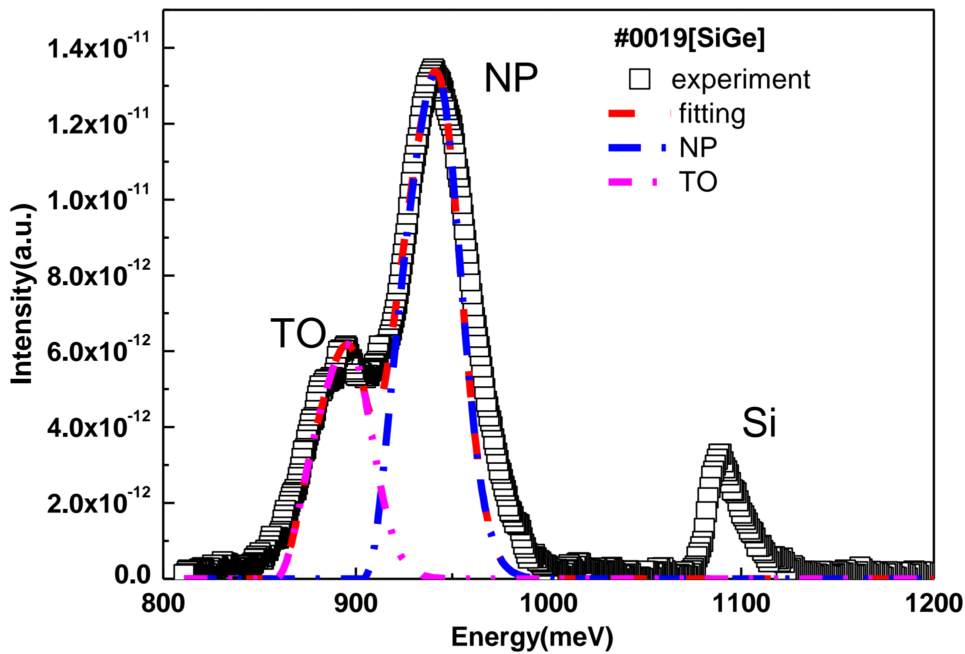

Fig.4-4 The PL spectrum of $Si_{0.73}Ge_{0.27}$ on Si with EHP fitting. The bandgap extracted from the cut-off of NP peak is 907meV.

The cross-section high resolution TEM and scanning transmission electron microscope (STEM) images of 7.4nm Si cap/24.8nm $Si_{0.73}Ge_{0.27}$ on Si shows no dislocation to relax strain (Fig.4-5(a)) and the interface is abrupt (Fig. 4-5(b)). Using STEM, which has the higher-angle detector, the atom with higher atomic number can be brighter than the smaller ones From the AFM (Fig.4-6), no cross-hatch is found and RMS roughness is only 0.1nm, which is smooth as the Si substrate surface (~0.1nm). No strain relaxation through the island or dislocation growth is found. The abrupt interface between SiGe/Si reflects no interdiffusion during the growth. Base on the SiGe thickness from TEM, the SiGe growth rate using DCS/GeH_4= 130/25 is ~0.41nm/sec.

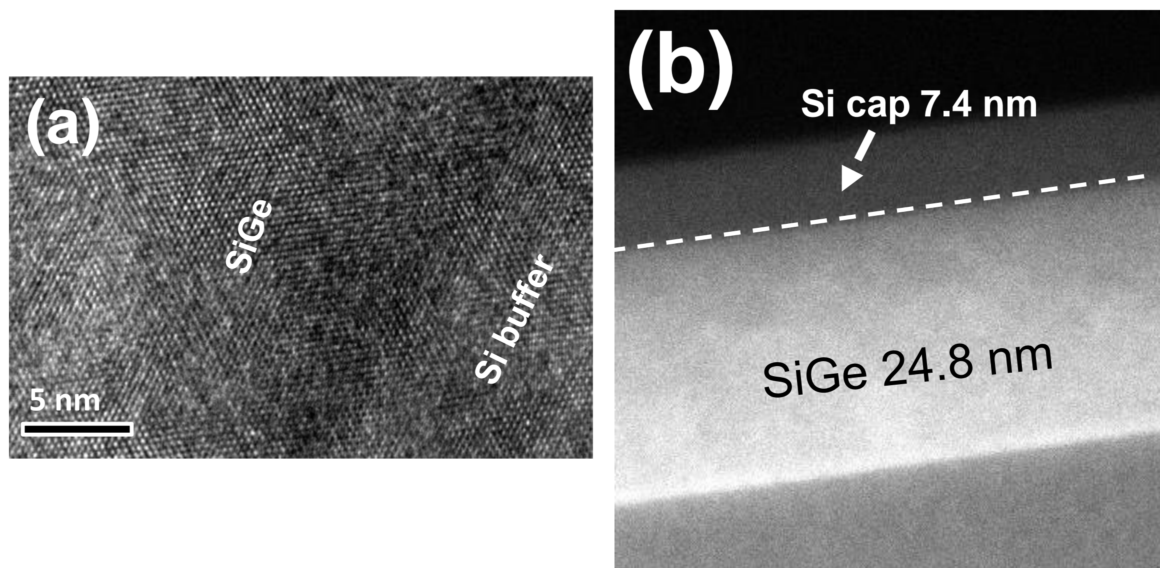

Fig.4-5 (a) The high resolution TEM of Si(7.4nm)/$Si_{0.73}Ge_{0.27}$ (24.8nm)/Si buffer on Si(001). No dislocation is found. (b) From the STEM images, abrupt interface shows no interdiffusion between $Si_{0.73}Ge_{0.27}$ and Si.

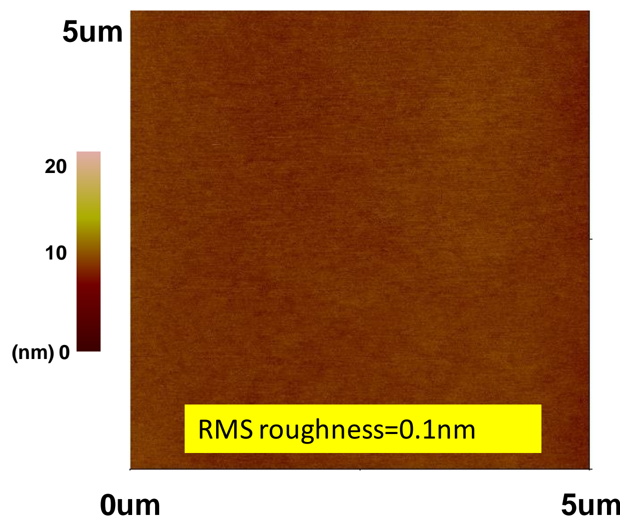

Fig.4-6 The AFM image of Si/ $Si_{0.73}Ge_{0.27}$/Si. The RMS roughness is only 0.1nm, which is close to Ge substrate surface. Note that no cross-hatch is found on surface.

With increasing GeH_4 from 25sccm to 250sccm, the $Si_{0.5}Ge_{0.5}$ can be obtained, in which the Ge content is also determined by XRD and PL (Fig. 4-7). High quality Si cap /$Si_{0.5}Ge_{0.5}$ on Si is realized with surface roughness at ~0.21nm (Fig. 4-8). No cross-hatch on the surface also indicates the SiGe film is dislocations free (Fig.4-8).

From SiGe thickness by the TEM, the 5nm Si cap/17nm $Si_{0.5}Ge_{0.5}$ on Si reflects the growth rate of $Si_{0.5}Ge_{0.5}$ is 2.9nm/sec. To study the Ge content effects on the SiGe growth rate, growth rate with different Ge content (x) of $Si_{1-x}Ge_x$ film is studied in Fig. 4-10. It is found that, with increasing GeH_4, not only Ge content can increase but also the SiGe growth rate can be enhanced (Fig.10). From the previous discussion about growth rate, the H desorption is the crucial role on growth rate. For one atom adsorbed, two open sites are needed. The catalytic effect of germane on the growth rate comes from the lower H desorption energy from Ge (1.5eV) than from Si (2.1eV) [6].

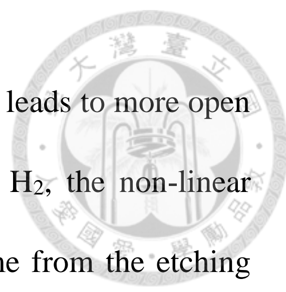

Increased hydrogen desorption from Ge sites on the growing surface leads to more open sites on surface. Since the decomposed DCS converts to HCl by H_2, the non-linear growth rate enhancement of SiGe using DCS and GeH_4 could come from the etching effect of HCl.

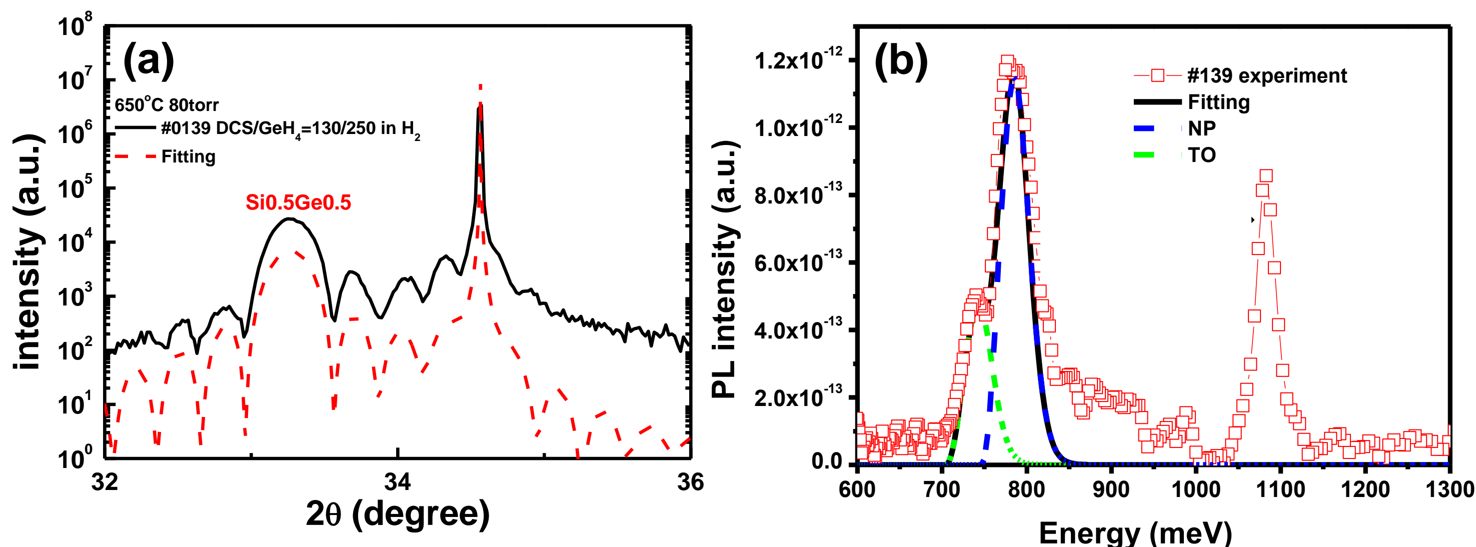

Fig.4-7 (a) The ω-2θ XRD and (b) the PL spectrum of $Si_{0.5}Ge_{0.5}$ on Si. Note the Ge% extraction from both XRD and PL is close to 50%.

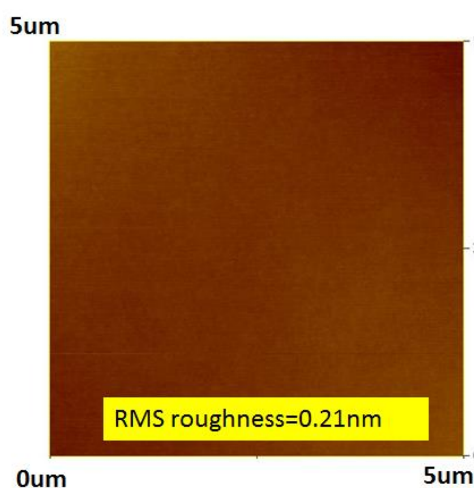

Fig.4-8 The AFM image of $Si/Si_{0.5}Ge_{0.5}/Si$. The RMS roughness is only 0.21nm. Note that no cross-hatch is found on surface.

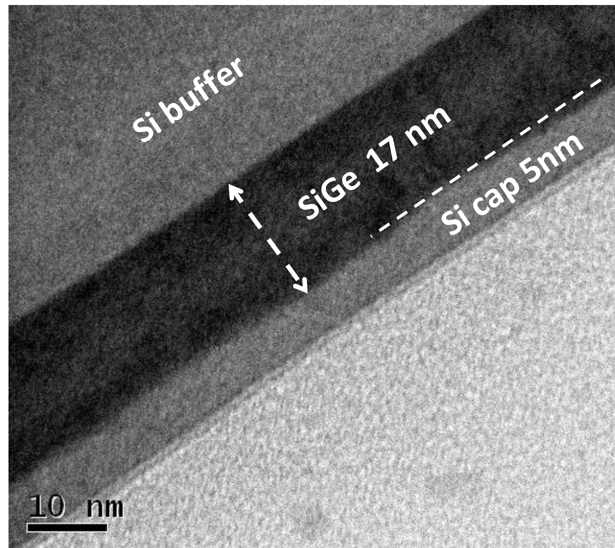

Fig.4-9 The high resolution TEM of Si(5nm)/$Si_{0.5}Ge_{0.5}$ (17nm)/Si buffer on Si(001). No dislocation is found and interface is abrupt.

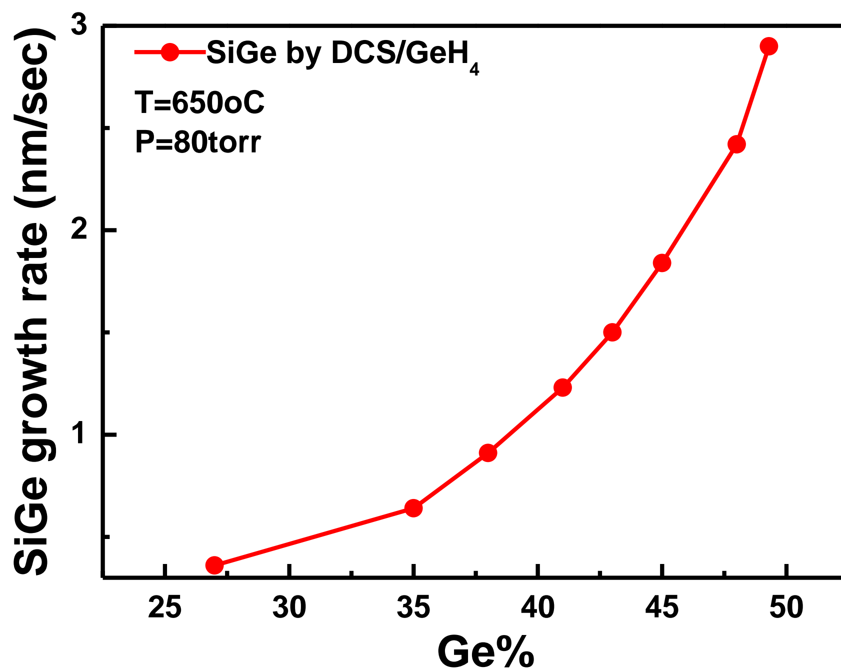

Fig.4-10 The SiGe growth rate of $Si_{1-x}Ge_x$ with $0.27<x<0.5$ Note the SiGe growth rate increases with increasing Ge content.

4.3 Carrier Gas Effects on SiGe Growth Rate on Si(001)

Using pure SiH_4 and the GeH_4 with the flow rate at 20sccm and 19sccm, higher growth rate of 0.56 nm/sec can have than its using DCS (130sccm)/GeH_4(25sccm). However, the SiGe using DCS /GeH_4 can have relatively stronger PL intensity of SiGe peak (Fig.4-11) than using SiH_4/GeH_4. The etching effect of HCl, which can clean and etching the growing surface, could be the reason for stronger PL and lower growth rate. Using the same methods discussed before, the Ge content using SiH_4/ GeH_4=25sccm/19sccm is about 21%, which is lower than using DCS/ GeH_4=130sccm/25sccm.

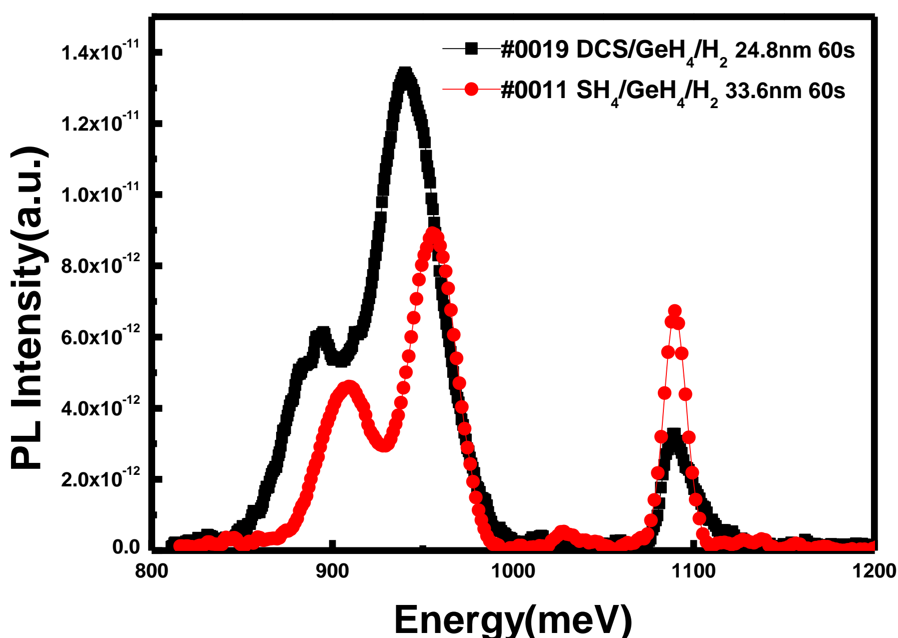

Fig.4-11 The PL spectra of SiGe using DCS/GeH_4 or SiH_4/GeH_4. Note higher Ge content and stronger SiGe PL can have by DCS/GeH_4

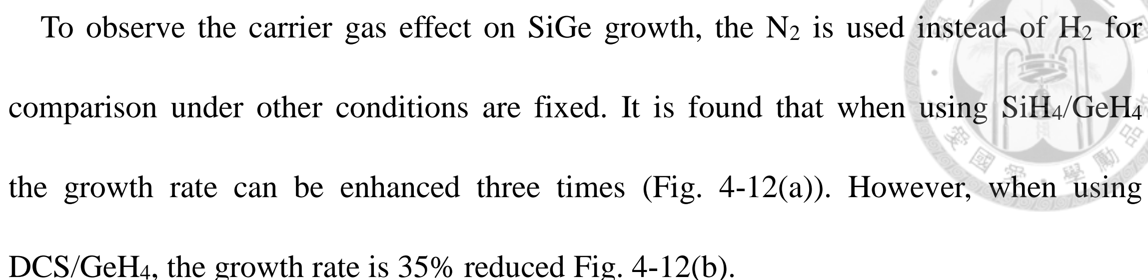

To observe the carrier gas effect on SiGe growth, the N_2 is used instead of H_2 for comparison under other conditions are fixed. It is found that when using SiH_4/GeH_4 the growth rate can be enhanced three times (Fig. 4-12(a)). However, when using DCS/GeH_4, the growth rate is 35% reduced Fig. 4-12(b).

In conventional CVD there are two growth regimes. One is mass-transport-limited, which is limited by the transport of the precursor to the surface of the wafer, via diffusion through a boundary layer. The other is the reaction-rate-limited which is limited by surface reaction between the gas and the surface. The former occurs at high growth temperatures and the latter occurs at low growth temperatures. For the SiGe growth at 650°C, it is in the reaction-rate-limited regime, the growth rate is dominated not by the gas flow but by the reaction-limited region, where both the H desorption to create the surface open site and the adsorption of adatom are the crucial roles. Note that two open sites needed on the growing surface for silane adsorption. When using SiH_4/GeH_4 in the N_2 ambient, open sites created only at Ge sites. On the other hand, in the case using DCS/GeH_4, low H_2 partial pressures disable the Si adsorption by $SiCl_2$ removing the Cl with H_2 and makes lower growth rate and higher Ge%.

$\underline{SiCl_2} + H_2 \rightarrow \underline{Si} + HCl\ (g)$

However, when using SiH_4/GeH_4 in the H_2 ambient, even the partial pressure of SiH_4 is larger than GeH_4, lower SiH_4 adsorption rate than GeH_4 makes large Ge%. In the N_2 ambient, where most of open sits are available and adatom adsorption is irrelevant, larger SiH_4 partial pressure than GeH_4 leads to low Ge%

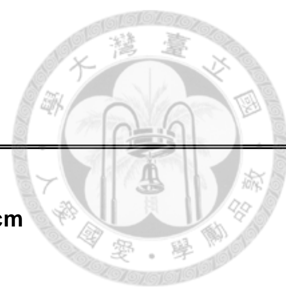

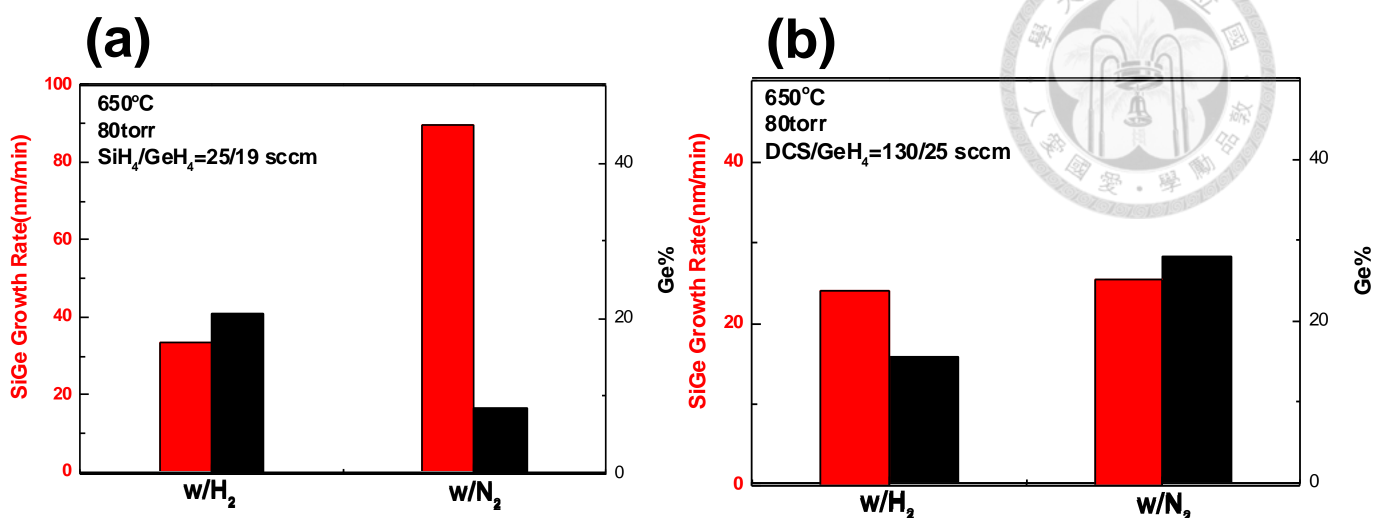

Fig.4-12 The SiGe growth rate and Ge content using (a) SiH_4/GeH_4 with H_2 and N_2 as carrier gas (b) DCS/GeH_4 with H_2 and N_2 as carrier gas composition.

4.4 Ge Growth on Si(001)

Due to the ~4.1% lattice mismatch between Si (5.431 Å) and Ge (5.658 Å), hetero-epitaxial growth of Ge on Si beyond critical thickness generally results in the formation of misfits and associated threading dislocations even islanding .There\are a number of ways to grow high quality single crystalline Ge on Si including using a graded Ge_xSi_{1-x} buffer [8, 9] or overgrowing Ge in a Si/SiO_2 template [10]. Here we use a two-step growth approach [11, 12] with cycling growth and anneal to grow high quality Ge on Si substrate.

The low-temperature buffer layer is to prevent the Ge from Stranski-Krastanov (S-K)

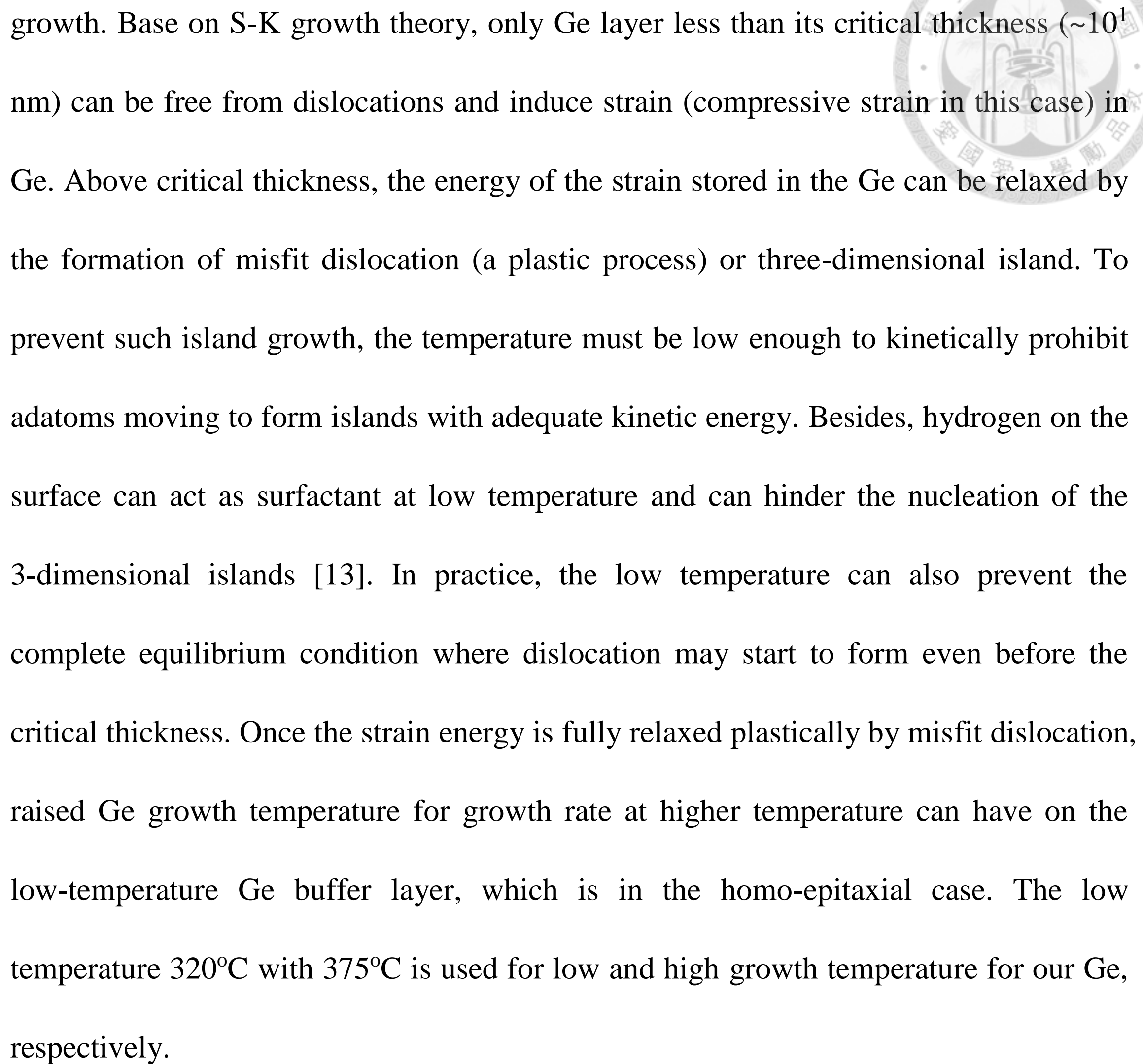

growth. Base on S-K growth theory, only Ge layer less than its critical thickness ($\sim 10^1$ nm) can be free from dislocations and induce strain (compressive strain in this case) in Ge. Above critical thickness, the energy of the strain stored in the Ge can be relaxed by the formation of misfit dislocation (a plastic process) or three-dimensional island. To prevent such island growth, the temperature must be low enough to kinetically prohibit adatoms moving to form islands with adequate kinetic energy. Besides, hydrogen on the surface can act as surfactant at low temperature and can hinder the nucleation of the 3-dimensional islands [13]. In practice, the low temperature can also prevent the complete equilibrium condition where dislocation may start to form even before the critical thickness. Once the strain energy is fully relaxed plastically by misfit dislocation, raised Ge growth temperature for growth rate at higher temperature can have on the low-temperature Ge buffer layer, which is in the homo-epitaxial case. The low temperature 320ºC with 375ºC is used for low and high growth temperature for our Ge, respectively.

Cycling thermal annealing at 825ºC after growth is performed to reduce decrease threading dislocations which propagate to the edge of the substrate at annealing. In the ref. 14, 1-2 order of reduction of threading dislocation density can have using thermal annealing at 900ºC. These threading dislocations act as both defect centers (non-radiative recombination centers) which degrade the electrical and optical properties of material. Fig. 4-13 is the 4.1mm epitaxial Ge on Si(001) with the 2.7×10^6 cm^{-2} dislocation density which is observed by etching pits using Schimmel etching. Due to the larger thermal expansion coefficient of Ge than Si, Ge tends to shrink more by

post annealing and induces ~0.16% in-plane tensile strain in Ge film upon cooling (Fig. 4-14).

The room temperature PL is taken for comparison with bulk Ge. The PL peaks at 695 meV and 780 meV are attributed to the indirect band transition and direct band transition, respectively (Fig.4-15). For the radiative recombination in an indirect bandgap material such as Ge, momentum conservation is achieved through the longitudinal acoustic phonon (28 meV) assisted transition [15]. In a direct transition, the momentum conserved is achieved without phonon. The energy difference of conduction band minimum between Γ valley and L valley is 140 meV at room temperature [16]. The spectra of the indirect and direct band gap emission in both bulk Ge and epi-Ge on Si sample were fitted by using the electron-hole plasma recombination model [17] [15] and the direct band gap recombination model [18], respectively. The band tail of absorption edge model is also taken into consideration in the direct band gap recombination model [19]. The integrated PL intensity ratios of direct to indirect band gap transition for the bulk n-Ge and epi-Ge on Si sample are 0.05 and 2.5, respectively. For the indirect radiative recombination in bulk Ge, a dominant LA phonon (~28 meV) is involved to satisfy the momentum conservation between the L valleys and the zone center in the valance band.

For the epi-Ge on Si sample, the large defect density in the Ge film may lead to a spread of trap levels in momentum space. These trap levels enhance the non-radiative recombination rate because the more phonons with different momentum can be involved in the momentum conservation. Thus, the relative intensity of the indirect band gap transition is lower in the epi-Ge on Si sample than in the bulk Ge [20].

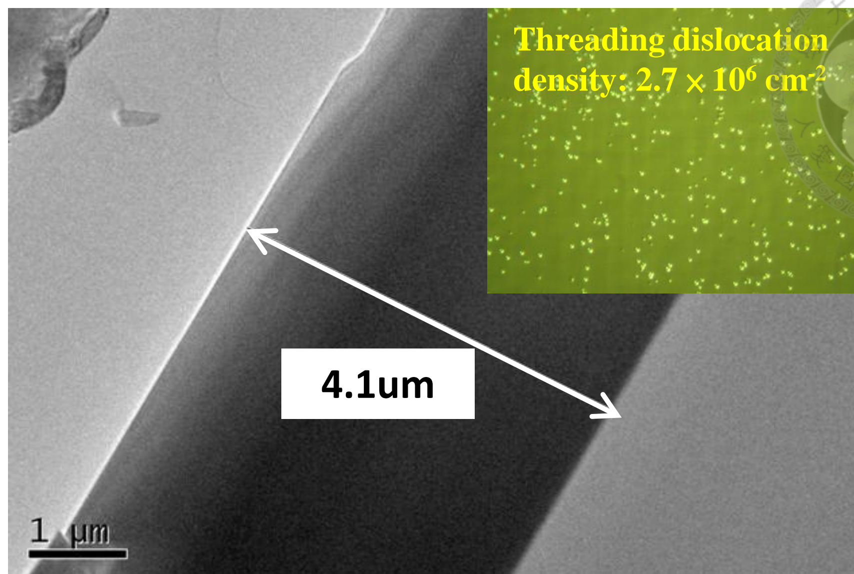

Fig.4-13 The high resolution TEM image of 4.1μm Ge on Si(001). The inset is the Nomarski micrograph of Ge with Shimmel etching for etching pits observation.

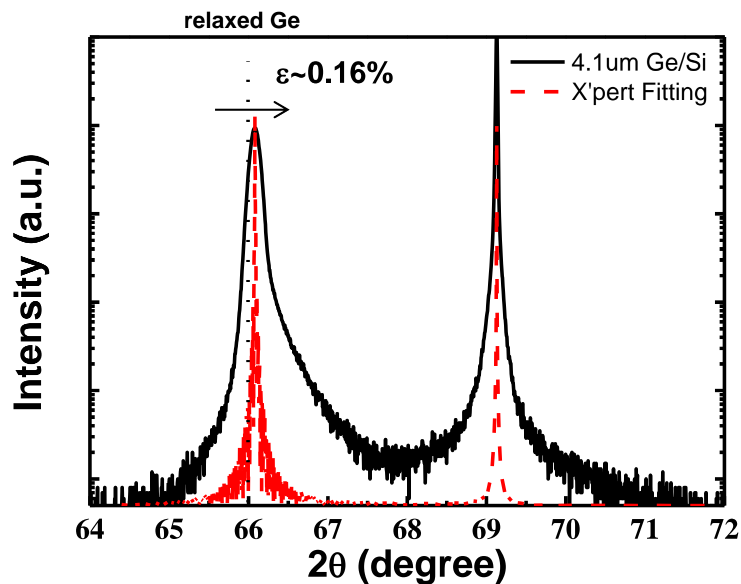

Fig.4-14 The ω-2θ XRD of 4.1 μm Ge on Si(001). Note the 0.16% tensile strain in Ge film.

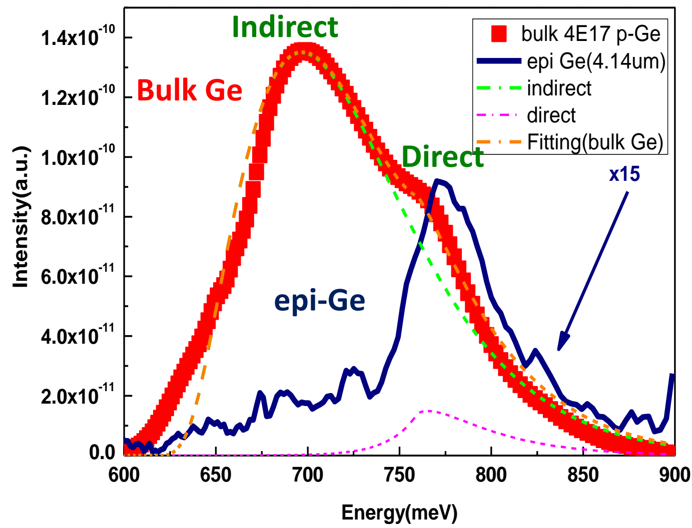

Fig.4-15 The PL spectra of the bulk Ge and epitaxial Ge on Si at room temperature. The integrated PL intensity ratios of the direct to indirect band gap transition of the bulk n-Ge and epitaxial Ge on Si sample are 0.05 and 2.5, respectively. The bulk Ge is ~15 times the integrated intensity of PL of the epitaxial Ge sample.

To observe the carrier gas effect on Ge growth, 375°C, 40torr with nitrogen and hydrogen are used for comparison. Both samples have post annealing in hydrogen at 825°C to reduce the threading dislocations. It is found that the Ge growth rate enhanced three times in N_2 over in H_2 (Fig.4-16 (a)). At 375°C for Ge growth, it is in the reaction-rate-limited regime, where H desorption more in nitrogen ambient can be the main reason for higher growth rate than in hydrogen. More open sites created in nitrogen ambient also lead to smoother surface than in hydrogen (Fig.4-16 (b)). Using N_2 as carrier gas strongly reduces the H_2 partial pressure compared to a deposition in hydrogen as carrier gas. The balance between the germane and hydrogen adsorption and the hydrogen desorption is modified depending on the nature of the carrier gas [21].

Lower hydrogen partial pressure favors germane adsorption and enhance hydrogen desorption to enhance Ge growth rate.

The surface roughness reduction can be explained in terms of the Ge diffusion barrier as compared to the Ge–H cluster [22]. The effect of attaching H to Ge reduces the diffusion barrier and increases the surface mobility by increasing the local density of states (LDOS) at the Fermi level [23]. The maximum barrier height reduction in the Ge–H may be set at 92 meV.

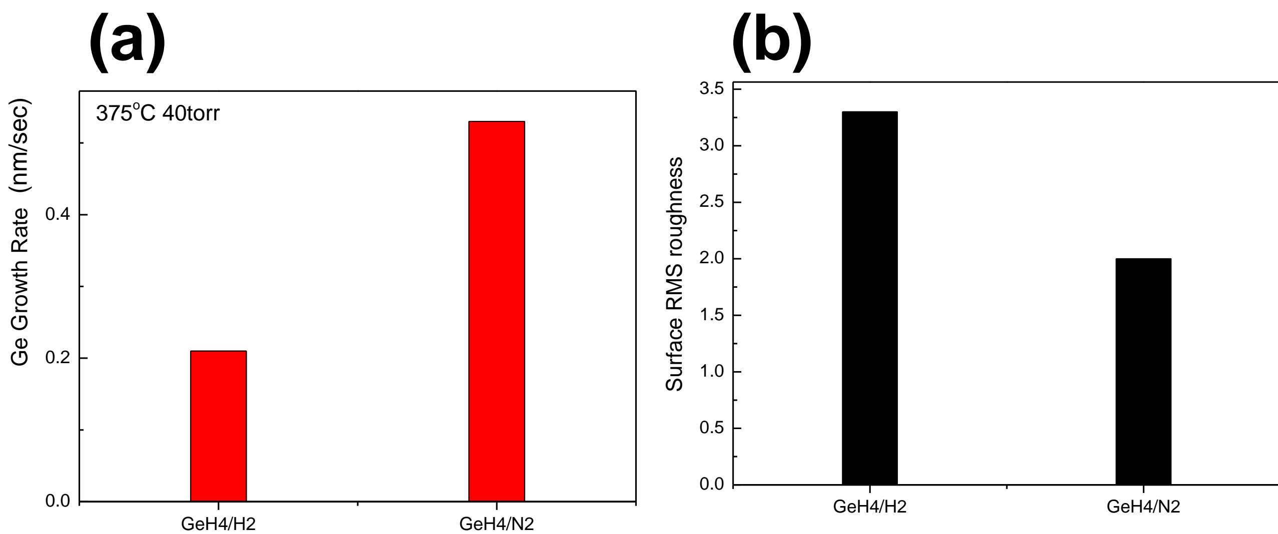

Fig.4-16 (a) The Ge growth rate using GeH_4/H_2 and GeH_4/N_2 as composition. Growth rate can be 3 times enhanced using GeH_4/N_2 and (b) smoother surface with surface RMS roughness of 2nm

4.5 Summary

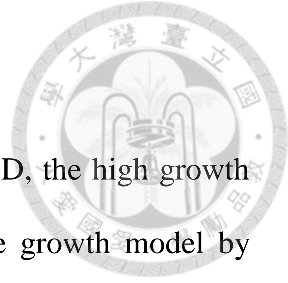

To reduce the cost of tool investment for epitaxial growth by CVD, the high growth rate of epitaxial layer is crucial for device development. With the growth model by CVD, the growth rate can be changed by Ge content of SiGe film, precursors, or carrier gas. Due to lower H desorption energy from Ge than from Si, more open sites created leads to higher growth rate when Ge% increasing. When using SiH_4/ GeH_4 for SiGe films and GeH_4 for Ge films growth with N_2 instead of H_2 as carrier gas. The growth condition having more surface open site in N_2 than in H_2 is the main reason for growth rate enhancement. In the case using DCS/ GeH_4 for SiGe films, the need of H_2 for the conversion of adsorbed $SiCl_2$ into Si results to growth rate reduction in N_2.

Reference:

[1] S.M. Gates, et al., *Appl. Phys. Lett*. **58**, 2964 (1991).

[2] S. M. Gates, et al.,*Journal of Chemical Physics*,**93,** 7493 (1990)**.**

[3] S.M. Gates et al., *Appl. Phys. Lett*.,**58,** 2964 (1991)**.**

[4] X. Xiao, C. Liu, J. Sturm, L. Lenchyshyn, and M. Thewalt, Appl. Phys. Lett., vol. 60, p. 1720, (1992).

[5] John C. Bean, PROCEEDINGS OF THE IEEE, VOL. *80,* NO 4, APRIL (1992).

[6] P. M. Garonne, J. C. Sturm and P. V. Schwartz, Appl. Phys. Lett., 56 (1990) 1275

[7] W.A.P. CLAASSEN and J. BLOEM, Journal of Crystal Growth 50 N807-815 (1980).

[8] E. A. Fitzgerald, Y.-H. Xie, M. L. Green, D. Brasen, A. R. Kortan, J. Michel, Y.-J. Mii, and B. E. Weir, Appl. Phys. Lett. 59(7), 811~813 (1991).

[9] S. B. Samavedam and E. A. Fitzgerald, J. Appl. Phys. 81(7), 3108~3116 (1997).

[10] T. A. Langdo, C. W. Leitz, M. T. Currie, E. A. Fitzgerald, A. Lochtefeld, and D. A. Antoniadis, Appl. Phys. Lett. 75(25), 3700~3702 (2000).

[11] L. Colace, G. Masini, F. Galluzzi, G. Assanto, G. Capellini, L. D. Gaspare, E. Palange, and F. Evangelisti, Appl. Phys. Lett. 72(24), 3175~3177 (1998).

[12] H.-C. Luan, D. R. Lim, K. K. Lee, K. M. Chen, J. G. Sandland, K. Wada, and L. C.

Kimerling, Appl. Phys. Lett 75(19), 2909~2911 (1999).

[13] D. J. Eaglesham, F. C. Unterwald, and D. C. Jacobson, Phys. Rev. Lett. 70(7), 966~969 (1993).

[14] J. Liu, Ph.D. thesis, Massachusetts Institute of Technolog,(2007).

[15] M. H. Liao, T.-H. Cheng, and C. W. Liu, *Appl. Phys. Lett*., Vol. 89, 261913, (2006).

[16] S. M. Sze, Physics of Semiconductor Devices, 2nd edition, Wiley, New York, (1981).

[17] C. W. Liu, M. H. Lee, M.-J. Chen, I. C. Lin, and C-F Lin, Appl. Phys. Lett., Vol. 76, pp. 1516-1518, (2000).

[18] P.-S. Kuo, B.-C. Hsu, P.-W. Chen, P. S. Chen, and C. W. Liu, Electrochem. Solid-State Lett., 7 (10), G201, (2004).

[19] M. El Kurdi, T. Kociniewski, T.-P. Ngo, J. Boulmer, D. Débarre, P. Boucaud, J. F. Damlencourt, O. Kermarrec, and D. Bensahel, Appl. Phys. Lett., Vol. 94, 191107, (2009).

[20] S.-R. Jan,C.-Y. Chen, C.-H. Lee, S.-T. Chan, K.-L. Peng, C. W. Liu,,Y. Yamamoto, and B. Tillack, Appl. Phys. Lett 98,141105, (2011).

[21] J. Pejnefors, S.-L. Zhang, H.H. Radamson, J.V. Grahn, M.O¨ stling, J. Appl. Phys. 88 (3),1655,(2000).

[22] Ammar Nayfeh, Chi On Chui, and Krishna C. Saraswat, Takao Yonehara, Appl. Phys. Lett 85,14, (2004).

[23] S. Horch, H. T. Lorensen, S. Helveg, E. Laegsgaard, I. Stensgaard, K. W. Jacobsen, J. K. Norskov, and F. Basenbacher, Nature (London) **398**, 134 (1999).

Chapter 5

Solid Phase Doped Ge by Chemical Vapor Deposition

5.1 Introduction

Ge has been widely investigated for high mobility channels of metal–oxide–semiconductor field effect transistors (MOSFETs). To realize high performance Ge MOSFETs, the source/drain doping is essential for scaled devices. Ion implantation still has the possibility to create defects even after implant anneal. For phosphorous, the point defects such as Ge vacancies are the main root cause of fast diffusion of dopants [1] and low activation fraction [2]. Although the diffusivity of boron is smaller than phosphorous in Ge, stable defects by implantation-induced crystal disorder remain after long time annealing [3]. All of these defects degrade the Ge diode performance to have non-ideal forward current, low on/off ratio, and high reverse saturation current. The required high temperature of 650°C ~ 750°C to release dopants from the solvent volume by spin-on doping on bulk Ge, results in the deep junction depth of ~500nm [4]. The carrier gas (N_2 vs. H_2) effects on the deposition of boron layers and phosphorous layers on Ge show that H_2 retards the incorporation of B_2H_6 and PH_3 [5, 6]. The Si p^+n

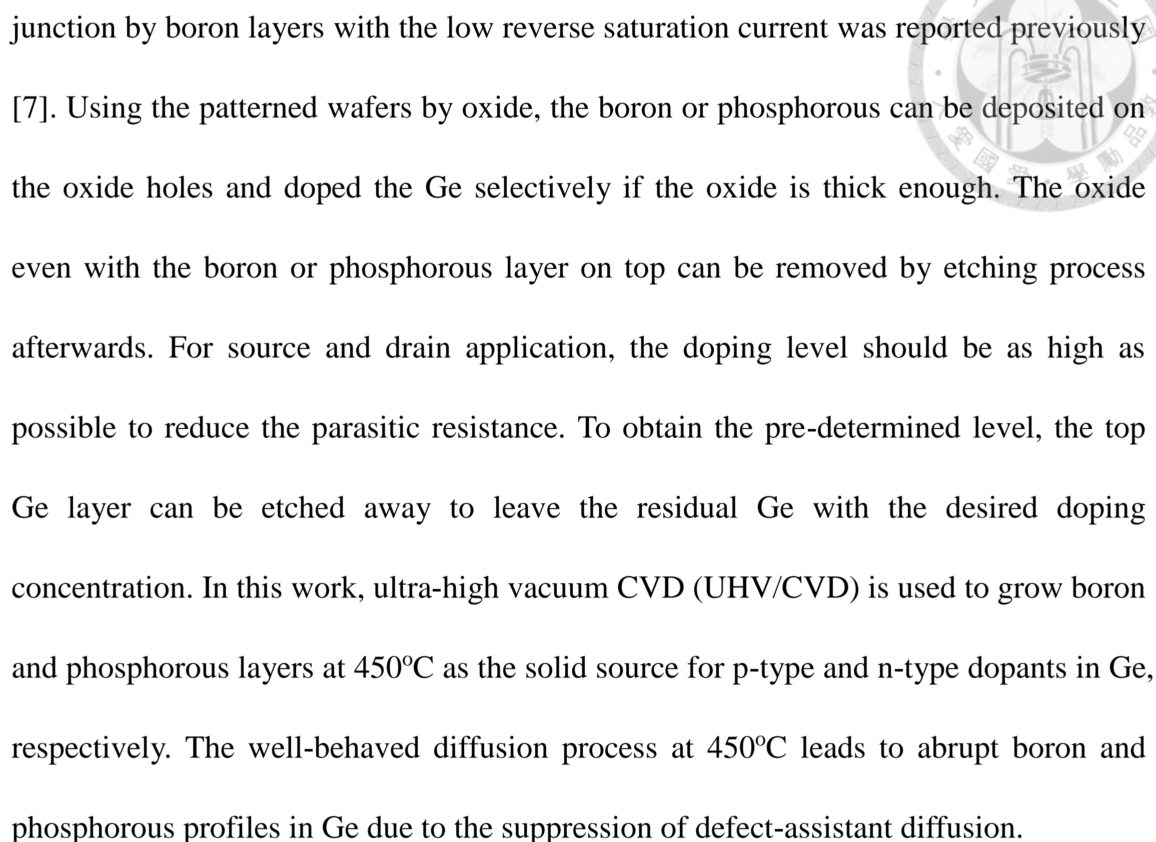

junction by boron layers with the low reverse saturation current was reported previously [7]. Using the patterned wafers by oxide, the boron or phosphorous can be deposited on the oxide holes and doped the Ge selectively if the oxide is thick enough. The oxide even with the boron or phosphorous layer on top can be removed by etching process afterwards. For source and drain application, the doping level should be as high as possible to reduce the parasitic resistance. To obtain the pre-determined level, the top Ge layer can be etched away to leave the residual Ge with the desired doping concentration. In this work, ultra-high vacuum CVD (UHV/CVD) is used to grow boron and phosphorous layers at 450°C as the solid source for p-type and n-type dopants in Ge, respectively. The well-behaved diffusion process at 450°C leads to abrupt boron and phosphorous profiles in Ge due to the suppression of defect-assistant diffusion.

5.2 Experiments

After HF dip, the (100) Si substrate is immediately loaded into UHV/CVD system with the cold-wall stainless steel chamber. The base pressure and the growth pressure are maintained below ~10^{-9} torr and ~10^{-3} torr, respectively. This high vacuum ensures the partial pressures of water vapor, oxygen, and hydrocarbons to be in the 10^{-11} torr range and reduces the contamination during the deposition process. Pure germane with the gas flow of 10 sccm and the growth temperature of 420°C is used for epitaxial Ge growth on Si (100) substrate. It has been shown the threading dislocation density in the Ge epitaxial film can be reduced by 1-2 order of magnitude to 2×10^{7} cm^{-2} using a

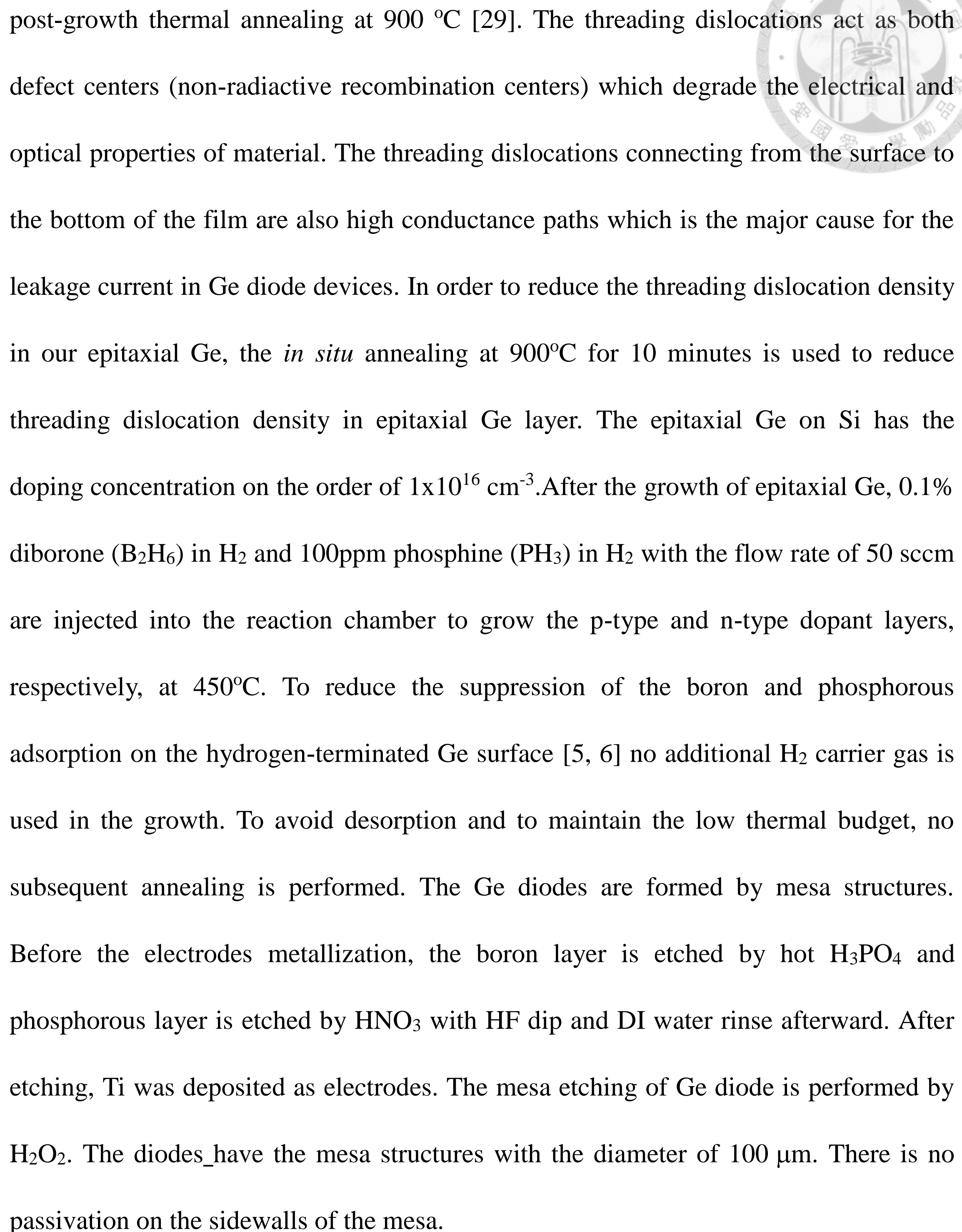

post-growth thermal annealing at 900 ^oC [29]. The threading dislocations act as both defect centers (non-radiactive recombination centers) which degrade the electrical and optical properties of material. The threading dislocations connecting from the surface to the bottom of the film are also high conductance paths which is the major cause for the leakage current in Ge diode devices. In order to reduce the threading dislocation density in our epitaxial Ge, the *in situ* annealing at 900^oC for 10 minutes is used to reduce threading dislocation density in epitaxial Ge layer. The epitaxial Ge on Si has the doping concentration on the order of $1x10^{16}$ cm^{-3}.After the growth of epitaxial Ge, 0.1% diborone (B_2H_6) in H_2 and 100ppm phosphine (PH_3) in H_2 with the flow rate of 50 sccm are injected into the reaction chamber to grow the p-type and n-type dopant layers, respectively, at 450^oC. To reduce the suppression of the boron and phosphorous adsorption on the hydrogen-terminated Ge surface [5, 6] no additional H_2 carrier gas is used in the growth. To avoid desorption and to maintain the low thermal budget, no subsequent annealing is performed. The Ge diodes are formed by mesa structures. Before the electrodes metallization, the boron layer is etched by hot H_3PO_4 and phosphorous layer is etched by HNO_3 with HF dip and DI water rinse afterward. After etching, Ti was deposited as electrodes. The mesa etching of Ge diode is performed by H_2O_2. The diodes_have the mesa structures with the diameter of 100 μm. There is no passivation on the sidewalls of the mesa.

5.3 Boron and Phosphorous layer on Ge by Chemical Vapor Deposition

Fig. 5-1 shows the cross-sectional transmission electron microscopy (TEM) images of epitaxial 130nm Ge on Si(001) before and after 900ºC annealing. The epitaxial Ge with the threading dislocation density at $5x10^8$ cm^{-2} is demonstrated. After B2H6 dn PH3 injection for two hours at 450ºC, boron and phosphorous layers are deposited on (100) Ge (Fig.5-2). The adsorbed B_2H_6 forms a ~5nm boron layer on the Ge surface (Fig. 5-2(a)), while the phosphorous layer by PH_3 is too thin to be clearly observed (Fig. 5-2(b)). The much lower sticking coefficient of phosphorous [8] and limitation of surface open sites for phosphorous adsorption [6] are responsible for this. It was reported that phosphorous can only reach a half of monolayer on Ge surface at saturation [9].

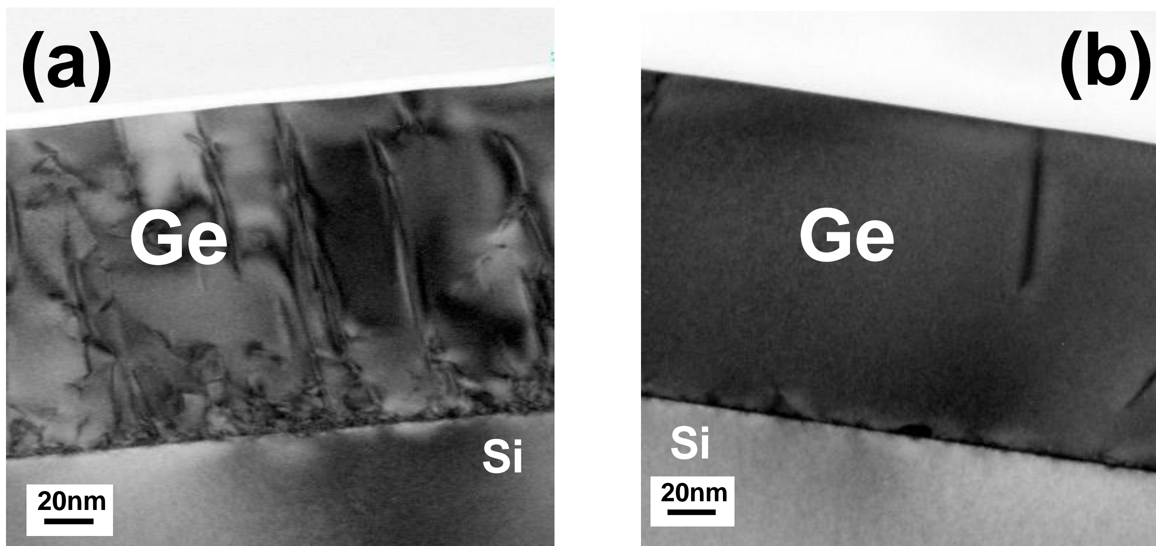

Fig.5-1 The TEM cross-sectional images of epitaxial Ge (a) as grown and (b) after anneal. Note the threading dislocation density in Ge film with post annealing is ~$5x10^8$ cm^{-2}.

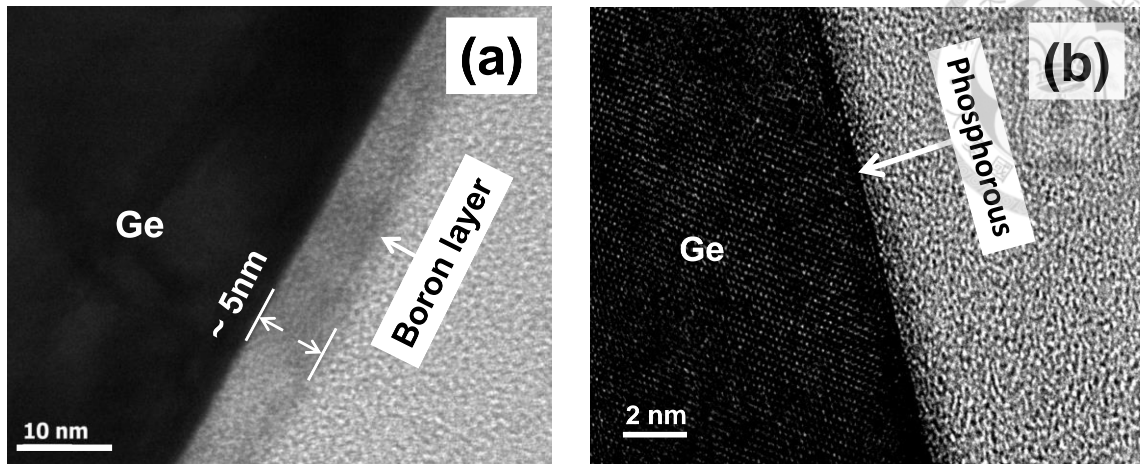

Fig.5-2 The TEM cross-sectional images of (a) a ~5nm boron layer and (b) less than monolayer phosphorous layer on epitaxial Ge growth at 450°C for 2 hrs.

The doping layer on Ge surface is further characterized by x-ray photoelectron spectroscopy (XPS) (Fig. 5-3). Based on material database and references [10-12], the embedded peaks can be deconvoluted. For the boron layer on Ge, there are boron-interstitial-clusters (B-B) at 186.5eV and the complex of boron coordinated with Ge (B-Ge) at 187.6eV (Fig. 5-3(a)). Due to the instability of the boron-vacancy pair, the boron above the solid solubility could be precipitated through the boron-interstitial-cluster [13]. The chemical structures of such clusters in Ge are not known, but BI^-, B_2I^0, and $B_2I_3{}^0$ clusters have been found in Si [14]. For the phosphorous layer on Ge, there are phosphorous- interstitial-clusters (P-P) at 130.3eV, the complex of phosphorous coordinated with Ge (P-Ge) at 129.2eV, and Ge 3p at 126eV (Fig. 5-3(b)). The B-Ge peak and P-Ge peak are signatures of the B and P diffusion into Ge, respectively.

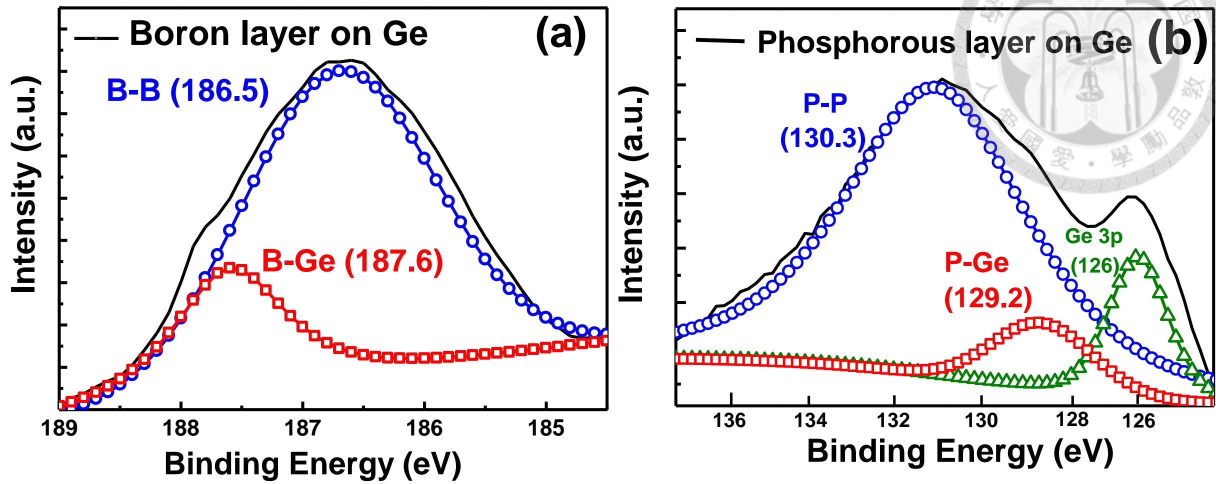

Fig.5-3 X-ray photoelectron spectra of (a) the boron layer on Ge and (b) the phosphorous layer on Ge. The peak in (a) can be deconvoluted into B-B peak (186.5eV) and (B-Ge) peak (187.6eV). The peak in (b) can be deconvoluted into P-P peak (130.3eV), P-Ge peak (129.2eV), and Ge 3p (126eV).

Notably, the high surface doping density with sharp spatial decay, obtained by using the solid phase doping technique, is of particular advantage for the formation of abrupt dopant distribution at source/drain of scaled devices [15,16]. The boron and phosphorrous doping profiles by the secondary ion mass spectrometry (SIMS) measurement using O_2^+ ion and Cs^+ ion, respectively, are shown in Fig. 5-4.The abruptness of boron profile is ~3nm/dec with the peak surface concentration of ~7×10^{21} cm^{-3} (Fig. 5-4(a)) while the abruptness of phosphorous profile is ~5nm/dec , with the peak surface concentration of ~6×10^{19} cm^{-3} (Fig. 5-4(b)). The target atoms are collided by the sputtering ions (O_2^+ or Cs^+) can be driven into deeper depth, so called "knock-in effect". Since the phosphorous is heavier than boron, the knock-in effect of phosphorous

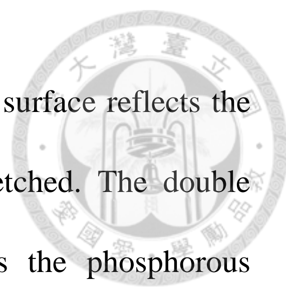

is not as significant as boron. The high boron concentration on the surface reflects the residuals of boron layers even after the top boron layers were etched. The double negatively charged vacancy (V_{Ge}^{-2}) [17] in n-type Ge mediates the phosphorous diffusion [18] while the Ge interstitial in p-type Ge mediates the boron diffusion [19]. Because the formation energy of Ge vacancy is 1 eV lower than that of interstitial [20], the V_{Ge}^{-2} dominates in the epitaxial Ge layers. The phosphorous diffusion, mediated by the vacancy, has a larger roll-off slope of phosphorous (5nm/dec) than boron (3nm/dec). Due to the calibration difficulties of the spreading resistance measurement on such thin layers, the reliable carrier profile cannot be measured.

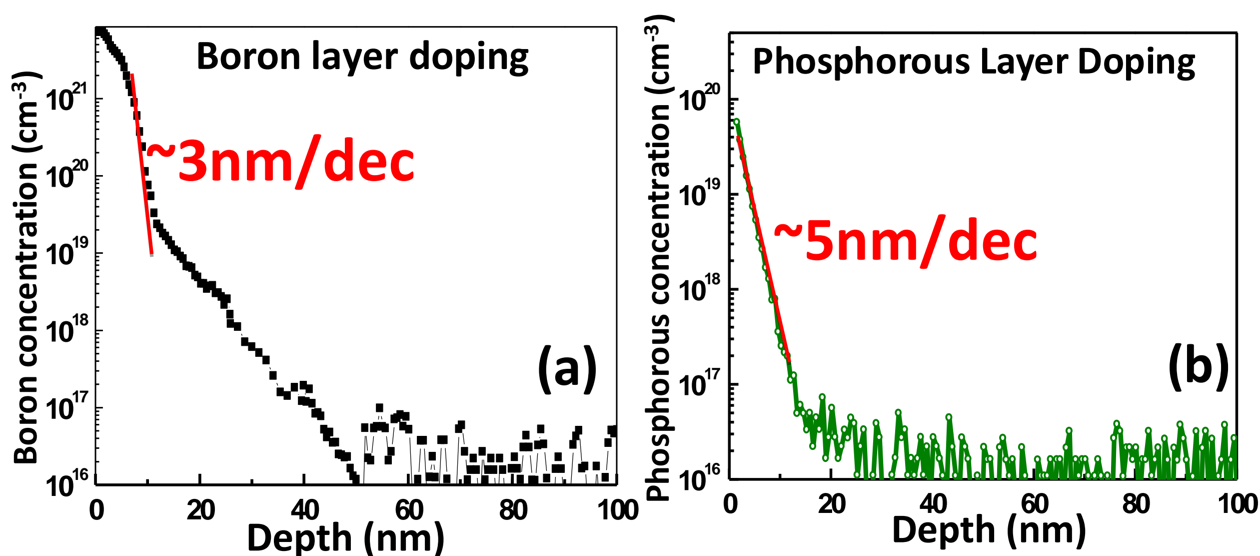

Fig.5-4 The SIMS profiles of (a) boron dopants in Ge and (b) phosphorous dopants in Ge.

5.4 $P^{+}N$ or $N^{+}P$ Ge Diodes by Solid Phase Layer Doping

Ge p^{+}/n and n^{+}/p diodes are fabricated by dopant layer deposition to investigate the effects of defects on diode performance. The electrical characteristics of p^{+}/n diodes doped by boron layer on epitaxial Ge has ~10^{5} on/off ratio, the reverse saturation current (I_{off}) of ~1×10^{-4}A/cm^{2} at -2V, and the ideality factor (n) of ~1.1 (Fig. 5-5(a)). The activation energy (E_a) of 0.34eV is estimated by the slope of the Arrhenius plot of the temperature-dependent reverse saturation currents (Fig. 5-5(b)).

The reverse saturation current from the Ref. 21 is

$$J_R = J_{diffusion} + J_{generation} = q\sqrt{\frac{D}{\tau}}\frac{n_i^2}{N} + \frac{qWn_i}{\tau}$$

where the W is the depletion width, D is the diffusivity of carrier, τ is the effective lifetime, and n_i is the intrinsic carrier density with an activation energy of half bandgap. There are two parts of activation energy in our $p^{+}n$ diodes. The activation energy of the generation current, which is near the half band gap of Ge, indicates that the carrier generation from conduction band to valance band is dominant instead of the defect-assisted generation current. When the temperature increases to ~100°C, the diffusion currents start to affect the reverse currents and the activation energy increases [21].

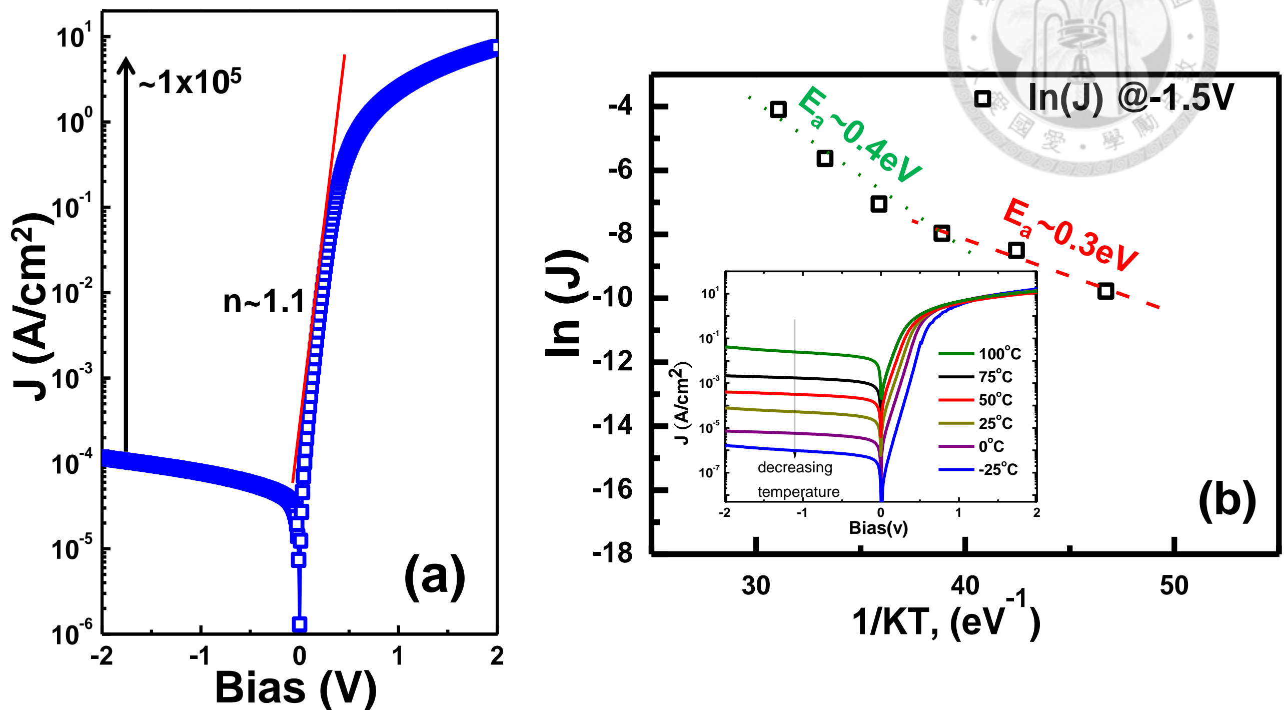

Fig.5-5 (a) Current density vs. voltage (J–V) characteristics of p^+/n Ge diodes by *in-situ* boron layer at the room temperature. The on/off ratio is about $\sim 1 \times 10^5$, ideality factor is about 1.1, and the reverse saturation current is $\sim 1 \times 10^{-4}$ A/cm^2. (b) The Arrhenius plot of the reverse saturation currents with the J-V curves at different temperatures in the inset.

From the Fig. 5-6 (a), the electrical characteristic of n^+/p diodes doped by phosphorous layers on epitaxial Ge has the on/off ratio of $\sim 1.5 \times 10^5$, the reverse saturation current of $\sim 4 \times 10^{-5}$ A/cm^2 at -2V, and the ideality factor of ~1.2. Since there is no passivation on the sidewalls of the mesa, the ideality factor of 1.2 of n^+/p can be the defects on the sidewalls and/or the defects near the bottom Ge on Si, where the misfit dislocations exist. The activation energy of 0.36eV (Fig. 5-6 (b)) is larger than those by ion implantation (0.15~0.26eV) [27], also indicating the carrier generation from the valance band edge to the conduction band edge.

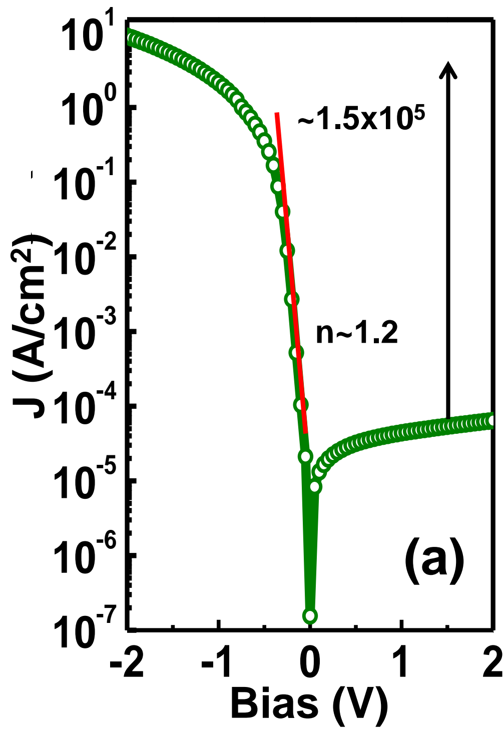

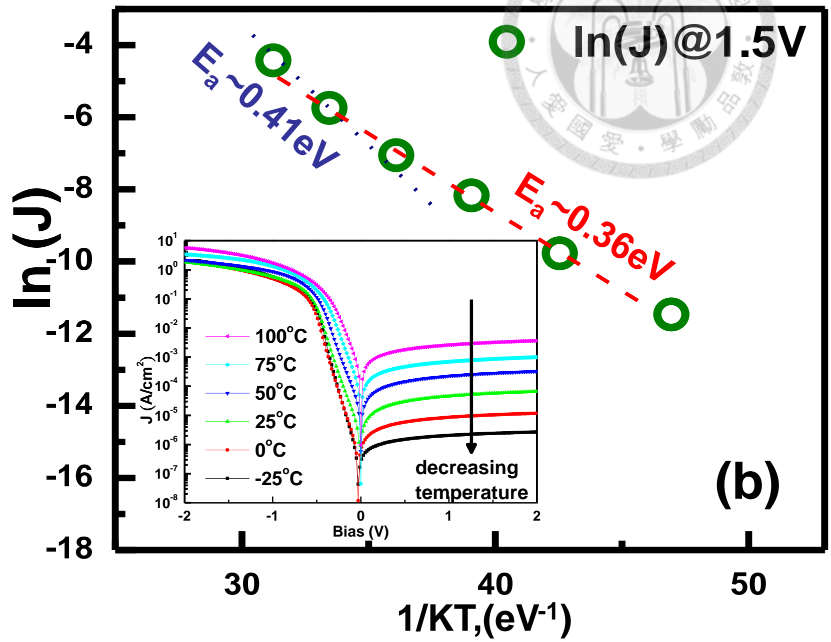

Fig.5-6 (a) J–V characteristics of n^+/p Ge diodes by *in-situ* phosphorous layer at the room temperature. The on/off ratio is ~$1.5\text{x}10^5$, ideality factor is about 1.2, and the reverse saturation current is $4\text{x}10^{-5}A/cm^2$. (b) The Arrhenius plot of the reverse saturation currents with the J-V curves at different temperatures in the inset.

5.5 Summary

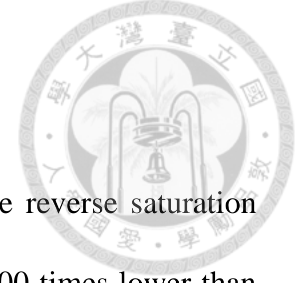

As compared to the reported Ge p+/n diodes in Table 5-I, the reverse saturation currents of our p+/n diodes by *in situ* boron layer doping is 10 to 100 times lower than that by ion implanted diodes on bulk Ge and epitaxial Ge [22-24] Free from implantation damage by *in-situ* boron layer doping is the root cause.

Table 5-1. Comparison of the p+/n Ge diodes by *in-situ* boron layer doping and other methods from precious works. Our diodes shows superior on/off ratio and I_{off} [22-24]

	on/off ratio	I_{off}(A/cm^2)
BF_2 ion implantation / RTA of Ge (Ref.22)	~1x10^3	3x10^{-2}
Metal induce defect annealing of Ge (Ref.23)	~4x10^4	1x10^{-2}
BF_2 ion implantation /RTA of epi-Ge (Ref.24)	~5x10^3	7x10^{-4}
B ion implantation/ RTA on Ge (our group)	~1x10^5	5x10^{-3}
Boron Layer Doping of epi-Ge (This work)	**~1x10^5**	**1x10^{-4}**

The on/off ratio also reaches the best among all the diodes. Besides, the reported n+/p diodes listed in the Table 5-II. Since the threading dislocations connecting from the surface to the bottom of the film are also high conductance paths which is the major cause for the leakage current in diodes, our epitaxial Ge on Si by *in situ* annealing after

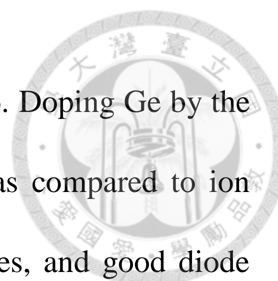

growth is also responsible for better performance than that in Ref.26. Doping Ge by the diffusion of dopant layers on Ge has much lower defect density as compared to ion implantation. The low defect density leads to abrupt dopant profiles, and good diode characteristics. This work provides an alternative path way for doping using chemical vapor deposition.

Table 5-2. Comparison of the n^+/p Ge diodes by *in-situ* phosphorous layer doping and other methods from precious works. Our diodes shows superior I_{off} [4, 25-28].

	on/off ratio	**I_{off} (A/cm^2)**
Sb ion implantation / Laser on Ge (Ref.25)	~$1x10^3$	$1x10^{-2}$
In situ Doping of epi-Ge (Ref.26)	~$1.1x10^4$	$1.2x10^{-2}$
Spin on doping on Ge (Ref.4)	~$1x10^6$	$1x10^{-4}$
Gas phase doping on Ge (Ref.27)	~$5x10^4$	$3x10^{-3}$
P ion implantation/ twice RTA on Ge (Ref.28)	~$2x10^5$	$5x10^{-5}$
Phosphorous Layer Doping of epi-Ge (This work)	**~$1.5 x10^5$**	**$4x10^{-5}$**

Reference

[1] Chi On Chui, L. Kulig, J. Moran, W. Tsai, and K. C. Saraswat, " Germanium n-type shallow junction activation dependences," Appl. Phys. Lett., Vol. 87, 091909, Aug. 2005.

[2] J. Kim, S. W. Bedell, and D. K. Sadana, "Improved germanium n^+/p junction diodes formed by coimplantation of antimony and phosphorus," Appl. Phys. Lett., Vol. 98, 082112, Feb. 2011.

[3] Yong Seok Suh, Malcolm S. Carroll, Roland A. Levy, Gabriele Bisognin, D. De Salvador, M. Alper Sahiner, and Clifford A. King, "Implantation and Activation of High Concentrations of Boron in Germanium," IEEE Trans. on Electron Devices, Vol. 52, no. 11, pp. 2416-2421, Nov. 2005.

[4] M. Jamil, J. Mantey, E. U. Onyegam, G. D. Carpenter, E. Tutuc, and S. K. Banerjee, "High-Performance Ge nMOSFETs With n+-p Junctions Formed by "Spin-On Dopant, " IEEE Electron Device Lett., Vol.32, no. 1203, pp.1203-1205, Sep. 2011.

[5] Yuji Yamamoto, Klaus Köpke, Rainer Kurps, Junichi Murota, and Bernd Tillack, "B atomic layer doping of Ge," Thin Solid Films, Vol. 518, issue 6 pp. S44~S47, Jan. 2010.

[6] Yuji Yamamoto, Rainer Kurps, Christian Mai, Ioan Costina, Junichi Murota, Bernd Tillack, "Phosphorus atomic layer doping in Ge using RPCVD," Solid-State Electronics, Vol. 83, pp. 25-29, May 2013.

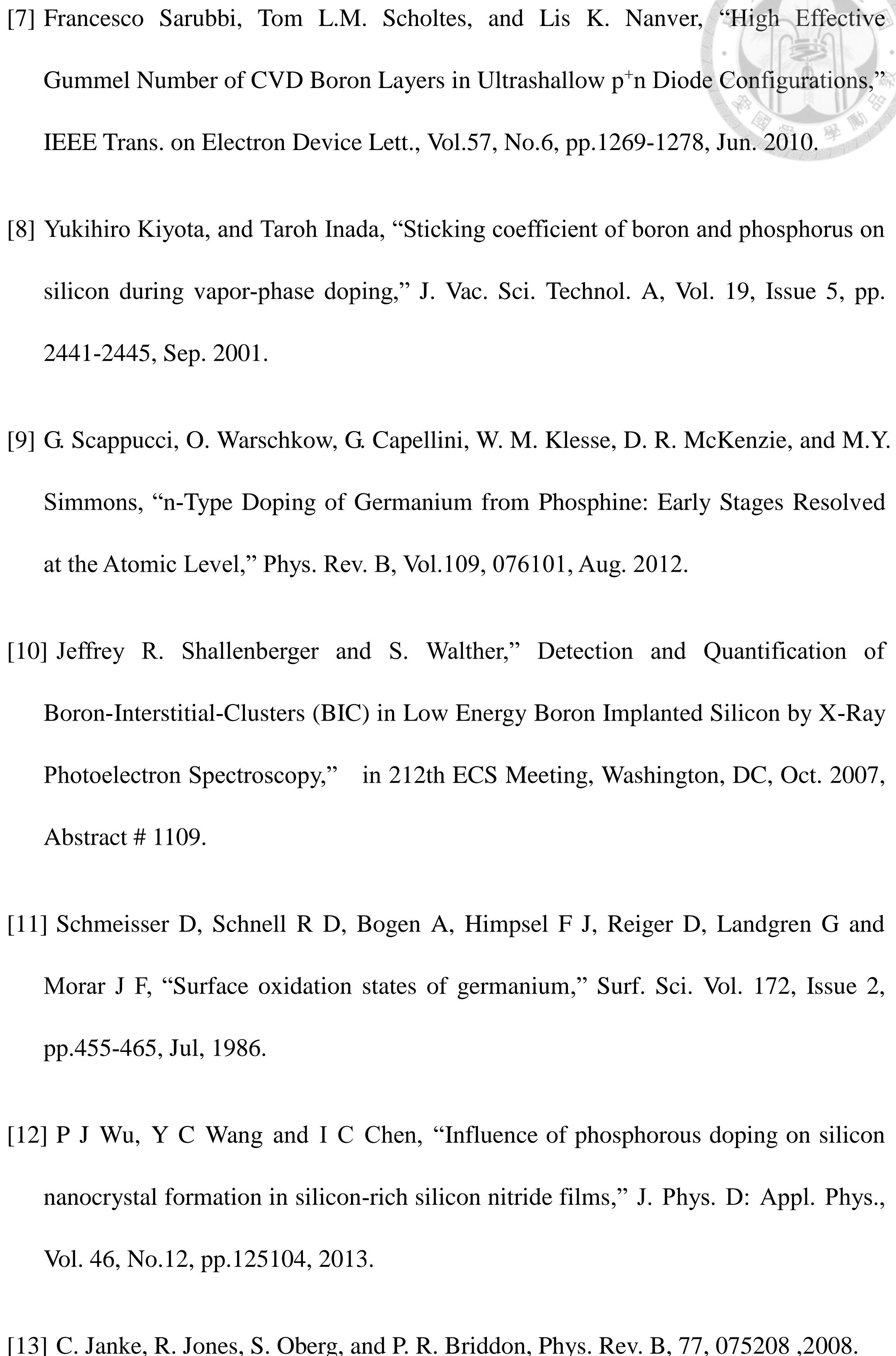

[7] Francesco Sarubbi, Tom L.M. Scholtes, and Lis K. Nanver, “High Effective Gummel Number of CVD Boron Layers in Ultrashallow p^+n Diode Configurations,” IEEE Trans. on Electron Device Lett., Vol.57, No.6, pp.1269-1278, Jun. 2010.

[8] Yukihiro Kiyota, and Taroh Inada, “Sticking coefficient of boron and phosphorus on silicon during vapor-phase doping,” J. Vac. Sci. Technol. A, Vol. 19, Issue 5, pp. 2441-2445, Sep. 2001.

[9] G. Scappucci, O. Warschkow, G. Capellini, W. M. Klesse, D. R. McKenzie, and M.Y. Simmons, “n-Type Doping of Germanium from Phosphine: Early Stages Resolved at the Atomic Level,” Phys. Rev. B, Vol.109, 076101, Aug. 2012.

[10] Jeffrey R. Shallenberger and S. Walther,” Detection and Quantification of Boron-Interstitial-Clusters (BIC) in Low Energy Boron Implanted Silicon by X-Ray Photoelectron Spectroscopy,” in 212th ECS Meeting, Washington, DC, Oct. 2007, Abstract # 1109.

[11] Schmeisser D, Schnell R D, Bogen A, Himpsel F J, Reiger D, Landgren G and Morar J F, “Surface oxidation states of germanium,” Surf. Sci. Vol. 172, Issue 2, pp.455-465, Jul, 1986.

[12] P J Wu, Y C Wang and I C Chen, “Influence of phosphorous doping on silicon nanocrystal formation in silicon-rich silicon nitride films,” J. Phys. D: Appl. Phys., Vol. 46, No.12, pp.125104, 2013.

[13] C. Janke, R. Jones, S. Oberg, and P. R. Briddon, Phys. Rev. B, 77, 075208 ,2008.

[14] J. Adey, J. P. Goss, and R. Jones, Phys. Rev. B, 67, 245325, 2003.

[15] Johnny C. Ho, Roie Yerushalmi, Zachery A. Jacobson, Zhiyong Fan, Robrt L. Alley, and Ali Javey, “Controlled nanoscale doping of semiconductors via molecular monolayers,” Nat. Materials Vol.7, pp.62-67,Jan. 2008.

[16] K.-W. Ang, J. Barnett, W.-Y. Loh, J. Huang, B.-G. Min, P. Y. Hung, I. Ok, J. H. Yum, G. Bersuker, M. Rodgers, V. Kaushik, S. Gausepohl, C. Hobbs, P. D. Kirsch, and R. Jammy, “300mm FinFET Results Utilizing Conformal, Damage Free, Ultra Shallow Junctions (Xj~5nm) Formed with Molecular Monolayer Doping Technique,” IEDM Tech. Dig., pp.35.5.1-35.5.4 (2011).

[17] Akio Hiraki, “Experimental Determination of Diffusion and Formation Energies of Thermal Vacancies in Germanium,”J. Phys. Soc. of Jpn. Vol. 21, No.1, pp.34-41, Jan. 1966.

[18] Chi On Chui, Kailash Gopalakrishnan, Peter B. Griffin, James D. Plummer, and Krishna C. Saraswat, “Activation and diffusion studies of ion-implanted p and n dopants in germanium,” Appl. Phys. Lett., Vol.83, pp.3575-3277, Oct. 2003.

[19] Suresh Uppal, Arthur F. W. Willoughby, Janet M. Bonar, Nick E. B. Cowern, Tim Grasby, Richard J. H. Morris, and Mark G. Dowset,” Diffusion of boron in germanium at 800 – 900 ° C,” J. Appl. Phys. Vol. 96, pp.1376-1380, Aug. 2004.

[20] J. Vanhellemont and E. Simoen, J. Electrochem. Soc. 154, H572, 2007.

[21] S.M.Sze, Physics of Semiconductor Device 2nd Edition, Bell Laboratories

incorporated, 1981.

[22] Chao-Ching Cheng, Chao-Hsin Chien, Guang-Li Luo, Ching-Lun Lin, Hung-Sen Chen, Jun-Cheng Liu, Chi-Chung Kei, Chien-Nan Hsiao, and Chun-Yen Chang," Junction and Device Characteristics of Gate-Last Ge p- and n-MOSFETs With ALD-Al_2O_3 Gate Dielectric," IEEE Trans. Electron Devices, Vol.56, no.8, pp.1681-1689, Aug. 2009.

[23] V. Ioannou-Sougleridis, S.F. Galata, E. Golias, T. Speliotis, A. Dimoulas, D. Giubertoni, S. Gennaro, M. Barozzi, "High performance n^+/p and p^+/n germanium diodes at low-temperature activation annealing,"Microelectronic Engineering Vol.88, issue 3, pp.254-261, Mar. 2011.

[24] Hyun-Yong Yu, Masato Ishibashi, Jin-Hong Park, Masaharu Kobayashi, and Krishna C. Saraswat, "p-Channel Ge MOSFET by Selectively Heteroepitaxially Grown Ge on Si,"IEEE Electron Device Lett.,"," Vol. 30, no. 6, pp.675-677, Jun. 2009.

[25] G. Thareja, S. Chopra, B. Adams, Y. Kim, S. Moffatt, K. Saraswat,, and Y. Nishi," High n-Type Antimony Dopant Activation in Germanium Using Laser Annealing for n^+/p Junction Diode," IEEE Electron Device Lett., Vol. 32, no.7 pp.838-840 Jul. 2011.

[26] Hyun-Yong Yu, Szu-Lin Cheng, Peter B. Griffin, Yoshio Nishi, and Krishna C. Saraswat, "Germanium In Situ Doped Epitaxial Growth on Si for High-Performance

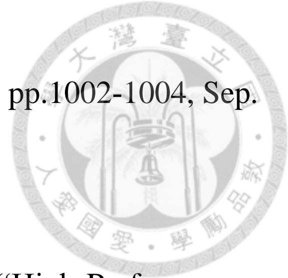

n^+/p-Junction Diode," IEEE Electron Device Lett., Vol. 30, no. 9, pp.1002-1004, Sep. 2009.

[27] K. Morii, T. Iwasaki, R. Nakane, M. Takenaka, and S. Takagi, "High-Performance GeO_2/Ge nMOSFETs With Source/Drain Junctions Formed by Gas-Phase Doping," IEEE Electron Device Lett., Vol. 31, no. 10, pp.1092-1094, Oct. 2010.

[28] Yen-Chun Fu, William Hsu, Yen-Ting Chen, Huang-Siang Lan, Cheng-Han Lee, Hung-Chih Chang, Hou-Yun Lee, Guang-Li Luo, Chao-Hsin Chien, C. W. Liu, Chenming Hu and Fu-Liang Yang, "High mobility high on/off ratio C-V dispersion-free Ge n-MOSFETs and their strain response," IEDM Tech. Dig., pp.18.5.1-18.5.4, 2010.

[29] J. Liu, Ph.D. thesis, Massachusetts Institute of Technology (2007).

Chapter 6

In-situ Doping of Ge by Chemical Vapor Deposition

6.1 Introduction

The solid phase doping by diffusion techniques, which can avoid transient enhanced diffusion (TED) and extended defect formation, has be introduced in Chapter 5 to form shallow junction without damage. However, for p-type doping, low solid solubility of boron (~$5x10^{18}$ cm^{-3}) in Ge limits the activated carrier concentration. For n-type doping, high temperature annealing is needed to activate and diffuse n-type dopant [1]. The dopant incorporation by ion-implantation causes point defects [2], such as Ge vacancy, and leads to fast diffusion [3, 4]. Moreover, Ge vacancy acts as an acceptor-like trap [5] and subsequently compensates with n-type dopants, leading to low dopant activation. The *in-situ* doped Ge has recently gained interest due to the potential to form an ultra-shallow junction with high level of dopant activation without any ion implantation damage and subsequent dopant deactivation [6-10]. Even by *in-situ* doping technique, the Ge $n^{+/}$p junction performance could be degraded during the post thermal process because dopant diffusion and loss [11]. To have better selectivity growth, Ge growth within surface reaction limited region is used to grown all the in-situ doped Ge. To have better crystalline quality doped Ge films, material and electrical characteristics of *in-situ*

p-type and n-type doped Ge with proper post annealing will also study. The abrupt and box-shape *in-situ* doped p^+Ge and n^+Ge on Si(001) with high level activation by chemical vapor deposition will be demonstrated in this chapter.

6.2 Experiments

The samples were grown in the ASM Episilon RTCVD industrial cluster tool. The growth pressure was for the majority of the samples 40 Torr. The flow of H_2 carrier gas was set at 15 standard liters per minute. Germane (GeH_4) diluted at 10% in H_2 was used as the source of Ge. Diborane (B_2H_6) or phosphine (PH_3) diluted both at 1% in H_2 are used as the sources of B and P atoms, respectively. After clean, a hydrogen bake at 1100°C in hydrogen for 2 minutes is used to carry out and ensures that no native oxide remained on the Si surface. The epitaxial Ge film is grown in Si (001) in two steps, which is discussed in Chapter.4. Before *in-situ* doped layer growth, the dopant gas baseline is purged with diluted B_2H_6 or PH_3 to avoid the dopant cross-contamination at the stabilization step. The initial doped Ge layer grown at 320°C and 40torr as seed layer and 375°C for growth rate. To *in-situ* dope Ge film with boron or phosphorus, B_2H_6 or PH_3 precursor gas is introduced in the both steps of the Ge growth. The chemical concentration profiles of boron or phosphorous in the deposited layers were measured by secondary ion mass spectroscopy (SIMS) using Cs^+ and O_2^+ analyzing beam, respectively. Designated implanted Ge standards were used for calibration. Electrically active carrier concentrations were deduced from both the hall concentration by van der pawu measurement and spreading resistance profiling (SRP).

To consider the metal work function to form the ohmic contact when doing the van der pawu measurement, the metal Pt (ϕ_m~5.65eV) and Al (ϕ_m~4.08eV) as contact electrode is used for p-type Ge and n-type Ge, respectively.

6.3 *In-situ* Boron Doped Ge by Chemical Vapor Deposition

In the Fig.6-1, the average boron concentration at ~6.8x10^{18}cm^{-3} by *in-situ* boron doped Ge grown 375°C with the mass flow ratio F(B_2H_6)/F(GeH_4)=0.0004. Boron peak near the Ge/Si interface indicates the gettering of boron by exist dislocation loops. With the post annealing in H_2 at 825°C for 10 minutes, the gettering is annihilated and closely 100% activated carrier concentration can reach near the surface. The Hall concentration extracted by van der pawu is 5x10^{18}cm^{-3}. However, the activation is dramatically reduced near the Ge/Si interface (Fig,6-2(a)), where lots of misfit dislocations exist (Fig.6-2(b)).

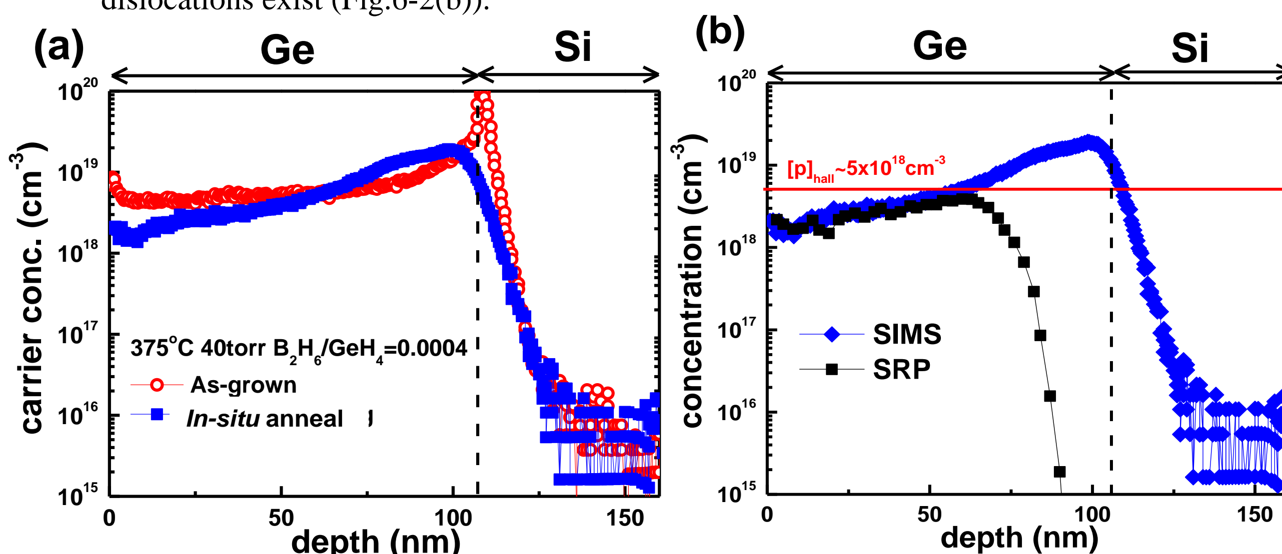

Fig.6-1 (a)SIMS of *in-situ* boron doped Ge with and without 825°C post H_2 annealing, and (b) SIMS depth profile comparing with SRP and hole concentration at ~5x10^{18}cm^{-3} by van der pawu measurment of *in-situ* boron doped Ge with 825°C post H_2 annealing

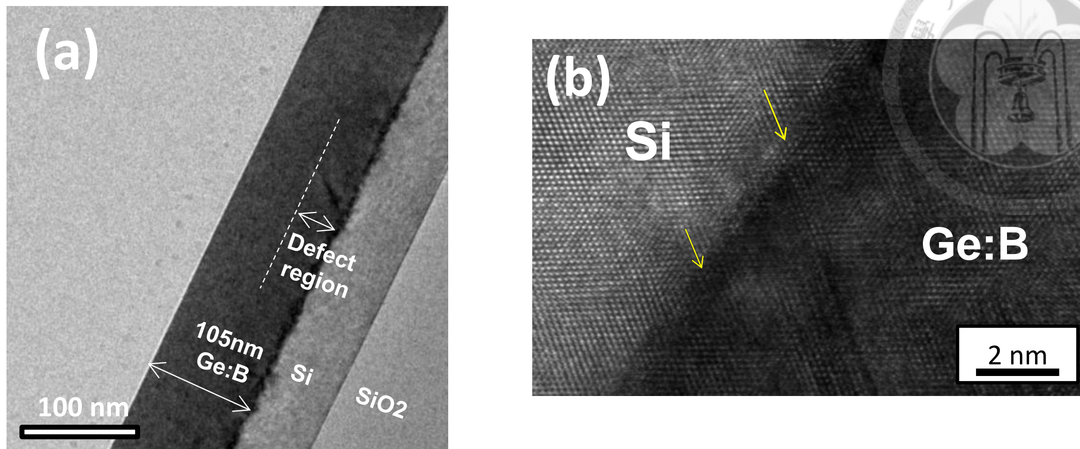

Fig.6-2 (a) The cross-sectional TEM images of 105nm *in-situ* boron doped Ge. Defect region within ~40nm defect region near the Ge/Si interface causes low activation region in Fig.6-1(b). (b) The misfit dislocation defects found at Ge/Si interface.

The van der pawu measurements are also taken to get the activated hall hole concentration in B-doped Ge grown at different mass flow ratio. The hall hole concentration increases monotonically with increasing $F(B_2H_6)/F(GeH_4)$ ratio. The total B atoms concentration in Ge has been demonstrated by Kim and Greene to increase first of all linearly (up to 10^{20} cm^{-3}) then superlinearly by gas-source molecular beam epitaxy with Ge_2H_6 [12] . In the Fig. 6-3(a), the hall hole concentration at $3x10^{20}$ cm^{-3} with the conductivity at 936 /Ω.cm can reach with $F(B_2H_6)/F(GeH_4)=0.08$. Higher concentration could be expected. However, poly-crystalline *in-situ* boron doped Ge could reduce the hole mobility and apparent carrier concentration reduction with too much boron incorporation [13]. Little thickness enhanced occurs for increasing B_2H_6 mass flow. B_2H_6 could promote the nucleation of the H-terminated surface could be the reason for increasing growth rate [14] (Fig. 6-3(b)).

(a)

375°C 40torr GeH_4=250sccm
with *In-situ* 825°C 10mins anneal

Hole Hall conc. (cm^{-3})

10^{20}
10^{19}
10^{18}

0.1 1 10

B_2H_6 flow rate (sccm)

(b)

375°C 40torr GeH_4=250sccm
with *In-situ* 825°C 10mins anneal

Growth rate (nm/min)

14.5
14.0
13.5
13.0

0.1 1 10

B_2H_6 flow rate (sccm)

Fig.6-3 (a) The hole hall concentration and (b) the growth rate obtained from *in-situ* boron doped Ge layers grown at 375°C as a function of the $F(B_2H_6)/F(GeH_4)$ mass flow ratio.

6.4 *In-situ* Phosphorous Doped Ge by Chemical Vapor Deposition

From the PH_3 adsorption behavior on Si in UHV/CVD system [15], it is found that the adsorbed phosphorus on Si at room temperature to 200°C is from the non-dissociated PH_3. The adsorbed PH_3 becomes dissociated at the temperature above 200 °C and the coverage of phosphorus does not change and could be increase if the hydrogen coverage reduced. Above 580 °C phosphorus itself starts to thermally desorb from the surface thus the coverage dramatically decreases. To avoid the desorption of phosphorous, the 375°C is also used to grow *in-situ* phosphorous doped Ge. The SIMS profile and SRP profile in Fig,6-4 show the average phosphorous concentration at ~$2x10^{20}cm^{-3}$ and the average activated carrier concentration is only ~$3x10^{18}cm^{-3}$ by *in-situ* phosphorus doped Ge grown 375°C with the mass flow ratio $F(PH_3)/F(GeH_4)$=0.08. the activation level is only 1%.

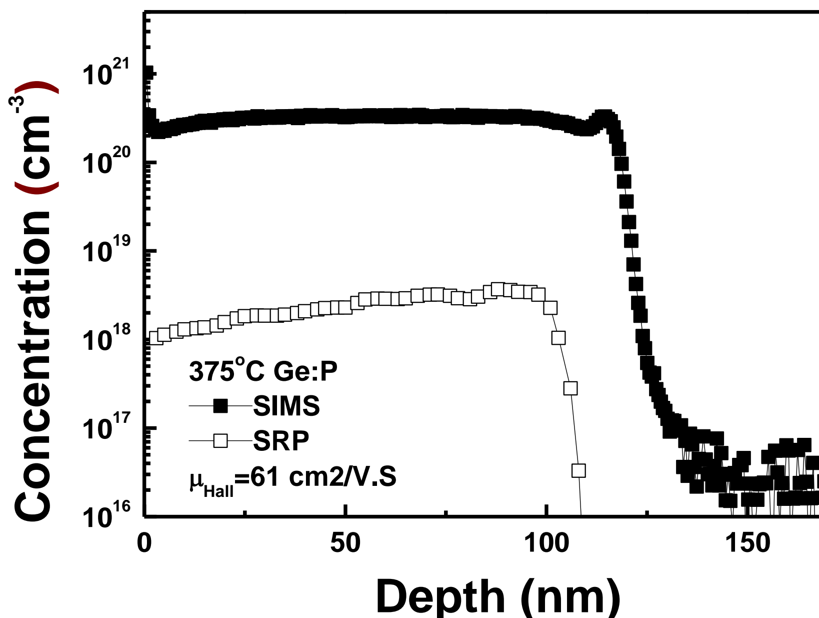

Fig.6-4 SIMS and SRP depth profile of *in-situ* phosphorous doped Ge at 375°C.

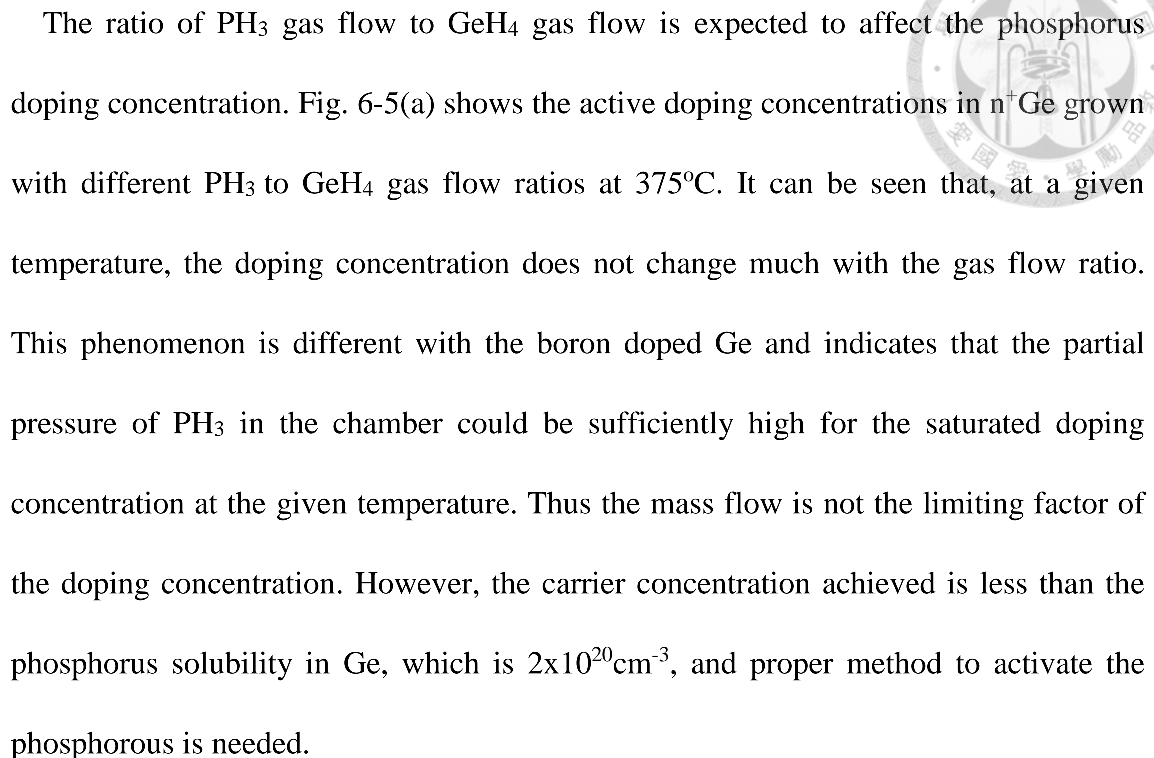

The ratio of PH_3 gas flow to GeH_4 gas flow is expected to affect the phosphorus doping concentration. Fig. 6-5(a) shows the active doping concentrations in n^+Ge grown with different PH_3 to GeH_4 gas flow ratios at 375ºC. It can be seen that, at a given temperature, the doping concentration does not change much with the gas flow ratio. This phenomenon is different with the boron doped Ge and indicates that the partial pressure of PH_3 in the chamber could be sufficiently high for the saturated doping concentration at the given temperature. Thus the mass flow is not the limiting factor of the doping concentration. However, the carrier concentration achieved is less than the phosphorus solubility in Ge, which is $2x10^{20}cm^{-3}$, and proper method to activate the phosphorous is needed.

Besides, lower growth rate when increasing PH_3 mass flow (Fig.6-5(b)). It is known that as the phosphorous coverage increases, possibly initially as a result of the ‘poisoning’ of growth sites by phosphorous complexes (in the case of Si growth the presence of phosphorous dimers at growth sites is implicated [16, 17], and later due to the presence of a more continuous P-rich layer. The observed behavior is an increasing density of phosphorous atoms on the Ge surface [18]: first isolated monomers which incorporate substitutionally and do not impact significantly on the Ge growth rate, then dimers or other phosphorous complexes which incorporate as electrically inactive or compensating defects, and finally larger assemblies of phosphorous atoms which may impede the growth rate, and further phosphorous incorporation owing to their increased stability on the Ge surface.

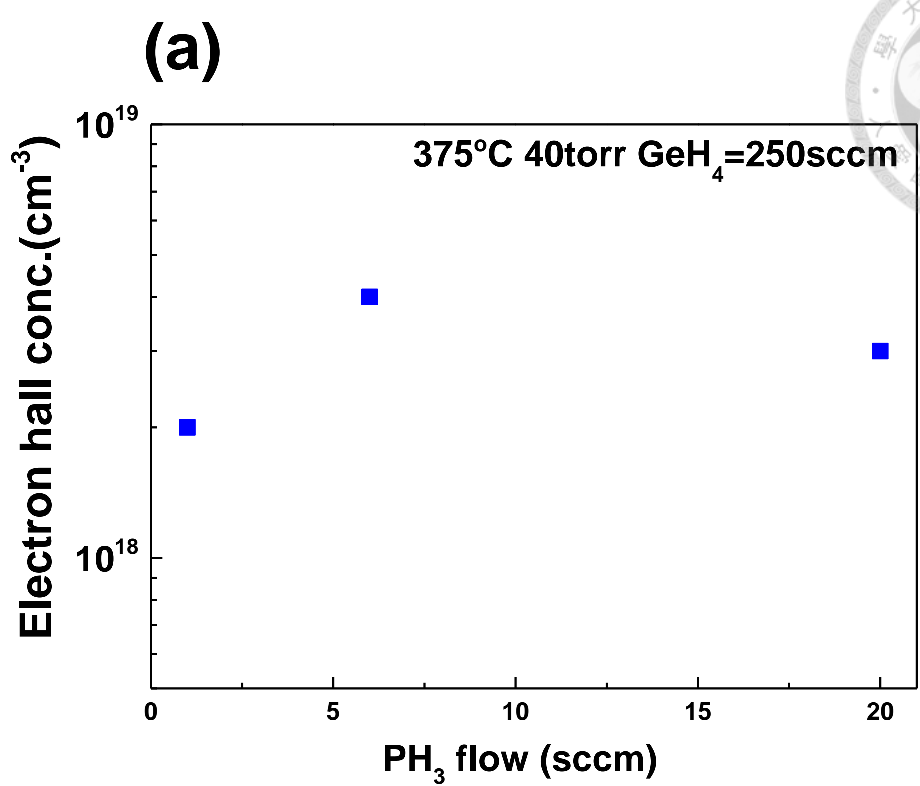

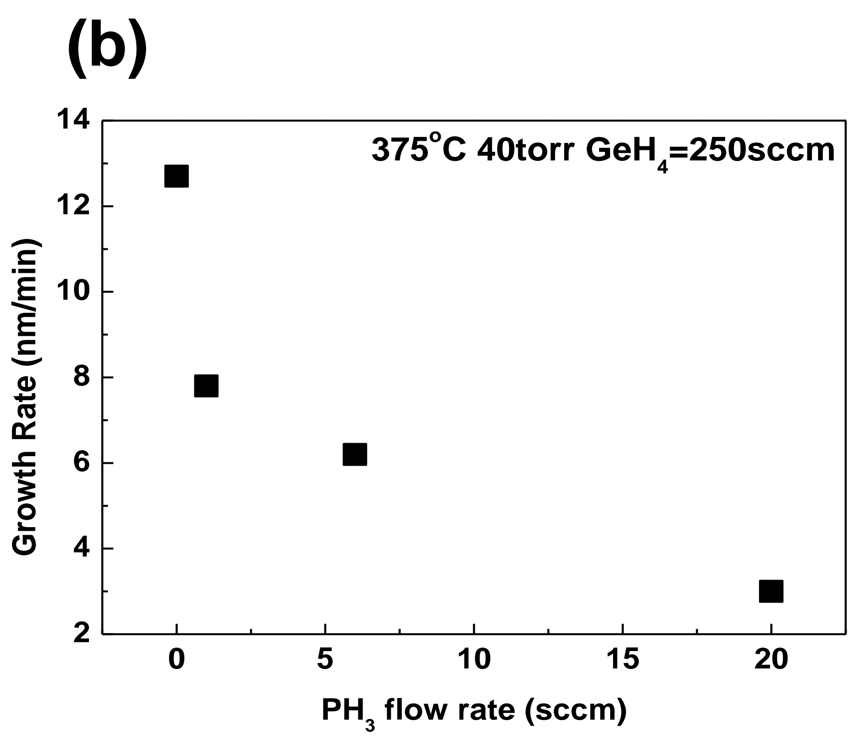

Fig.6-5 (a)The electron hall concentration and (b) the growth rate obtained *in-situ* phosphorous doped Ge layers grown at 375°C as a function of the $F(PH_3)/F(GeH_4)$ mass flow ratio.

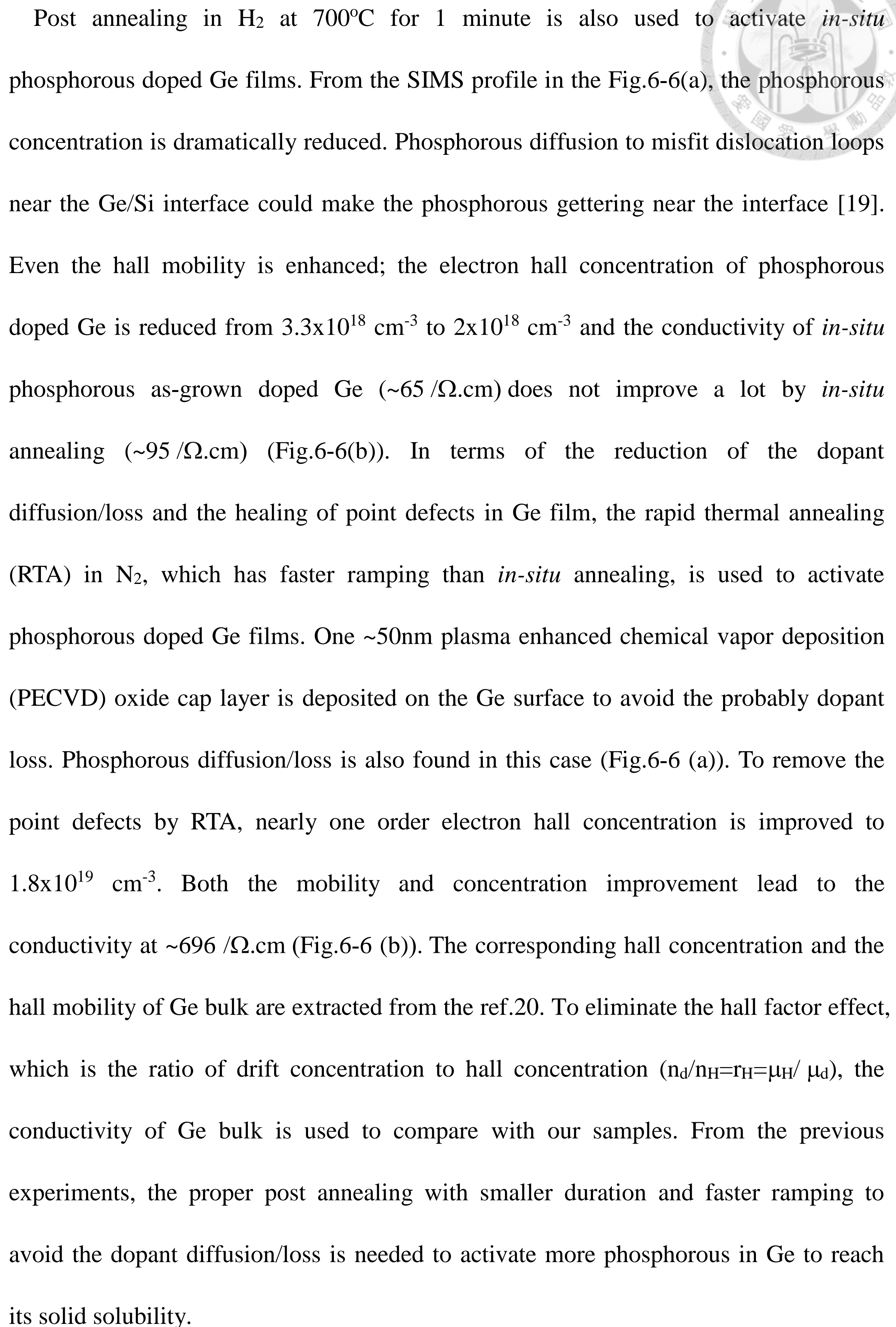

Post annealing in H_2 at 700°C for 1 minute is also used to activate *in-situ* phosphorous doped Ge films. From the SIMS profile in the Fig.6-6(a), the phosphorous concentration is dramatically reduced. Phosphorous diffusion to misfit dislocation loops near the Ge/Si interface could make the phosphorous gettering near the interface [19]. Even the hall mobility is enhanced; the electron hall concentration of phosphorous doped Ge is reduced from 3.3×10^{18} cm^{-3} to 2×10^{18} cm^{-3} and the conductivity of *in-situ* phosphorous as-grown doped Ge (~65 /Ω.cm) does not improve a lot by *in-situ* annealing (~95 /Ω.cm) (Fig.6-6(b)). In terms of the reduction of the dopant diffusion/loss and the healing of point defects in Ge film, the rapid thermal annealing (RTA) in N_2, which has faster ramping than *in-situ* annealing, is used to activate phosphorous doped Ge films. One ~50nm plasma enhanced chemical vapor deposition (PECVD) oxide cap layer is deposited on the Ge surface to avoid the probably dopant loss. Phosphorous diffusion/loss is also found in this case (Fig.6-6 (a)). To remove the point defects by RTA, nearly one order electron hall concentration is improved to 1.8×10^{19} cm^{-3}. Both the mobility and concentration improvement lead to the conductivity at ~696 /Ω.cm (Fig.6-6 (b)). The corresponding hall concentration and the hall mobility of Ge bulk are extracted from the ref.20. To eliminate the hall factor effect, which is the ratio of drift concentration to hall concentration ($n_d/n_H=r_H=\mu_H/\mu_d$), the conductivity of Ge bulk is used to compare with our samples. From the previous experiments, the proper post annealing with smaller duration and faster ramping to avoid the dopant diffusion/loss is needed to activate more phosphorous in Ge to reach its solid solubility.

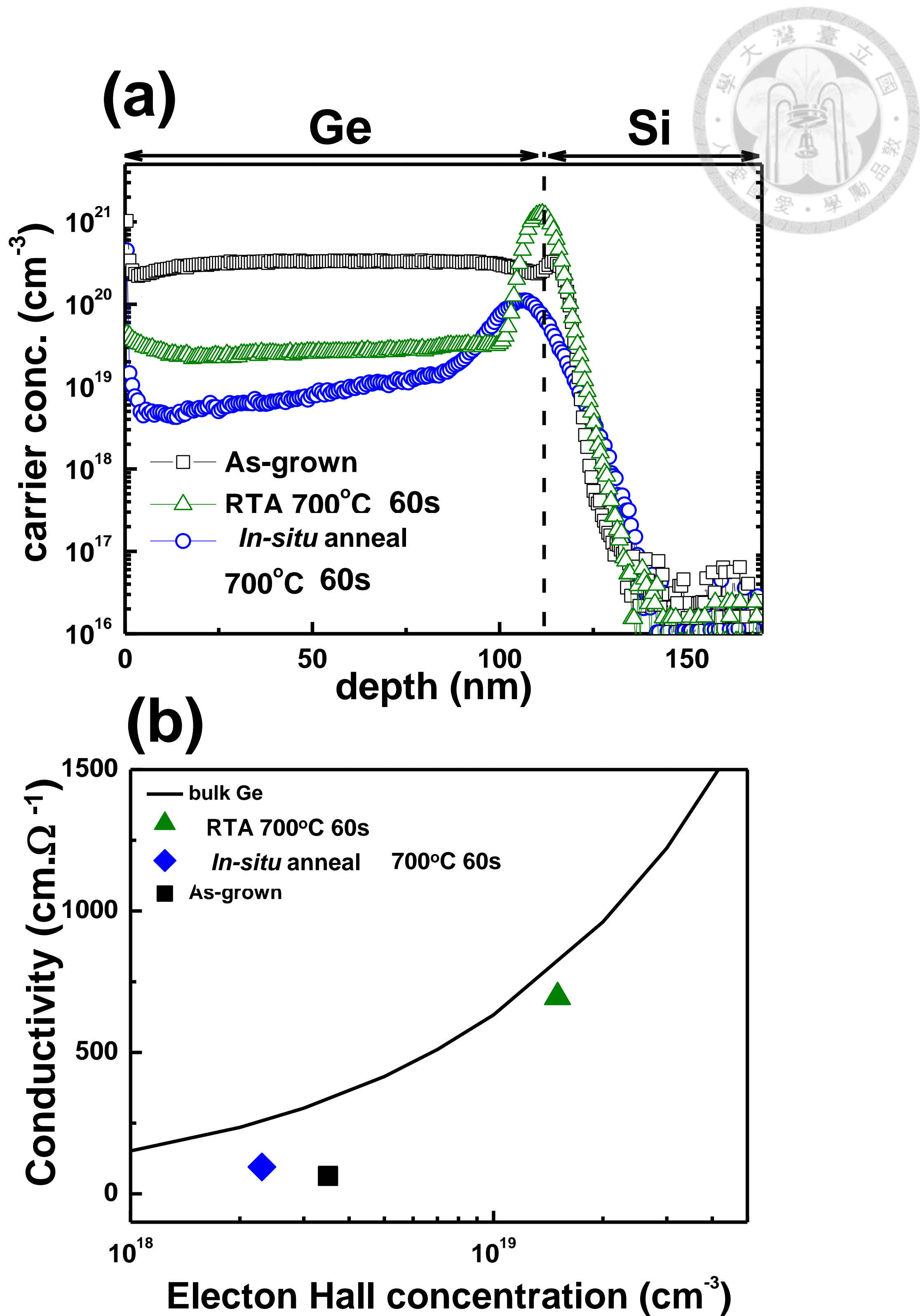

Fig.6-6 (a) SIMS depth profiles of the *in-situ* phosphorous doped Ge received *in-situ* annealing in H_2, RTA in N_2, and (b) The conductivity as a function of the electron hall concentration by the van der pawu measurement.

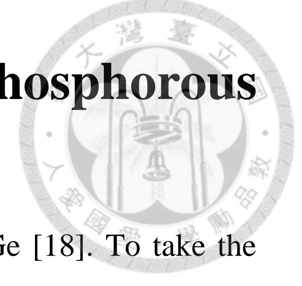

6.5 Laser Annealing of *In-situ* Phosphorous Doped Ge

The laser annealing has been used in antimony ion-implanted Ge [18]. To take the both advantages of technologies, the *in-situ* doping and laser annealing are recombined to have heavily activated n^+Ge for the first time here.

The laser annealing is performed on *in-situ* doped Ge using a pulsed 532-nm laser with the energy density of 0.5J/cm^2 at a single pulse. Like the case with RTA, Ooe ~50nm PECVD oxide cap layer is also deposited on the Ge surface. From the SIMS in the Fig.6-7, no phosphorous diffusion/loss is found and maximum 2x10^{20} cm^{-3} chemical concentrations can reach. The Ge adsorption behavior of 532nm laser can be described by the Beer–Lambert law

$$I(x_i,t) = (1-R)\times I_0(t)\exp(-x_i/\lambda)$$
$$P(x_i,t) = I(x_i,t) - I(x_i+\Delta x,t) \tag{6.1}$$

I(x) is the light power density pass through the Ge at length of x, P(x) is the adsorbed energy by Ge at length.

The adsorbed energy by Ge can diffuse by the thermal conduction. Using finite element technique with adding a power source term, the temperature of Ge by irradiated by laser can be described by the thermal conductivity [21]:

$$\frac{C_i[T(x_i,t+\Delta t)-T(x_i,t)]}{\Delta t} = P(x_i,t)+h_i[T_c-T(x_i,t)]+\sum_{j=x,y,z}K_{x_i}[T(x_i+\Delta x_j,t)-T(x_i,t)+\sum_{j=x,y,z}K_{x_i}[T(x_i-\Delta x_j,t)-T(x_i,t)] \tag{6.2}$$

Here x_i stands for the position of ith node, Δx_i stands for the finite increment of x,y,z directions, c_i is the heat capacitance, $p(x_i,t)$ is the power input , k_{xi} is the thermal conductivity and h_i is the heat dissipation of ith node at instant t. The Ge temperature

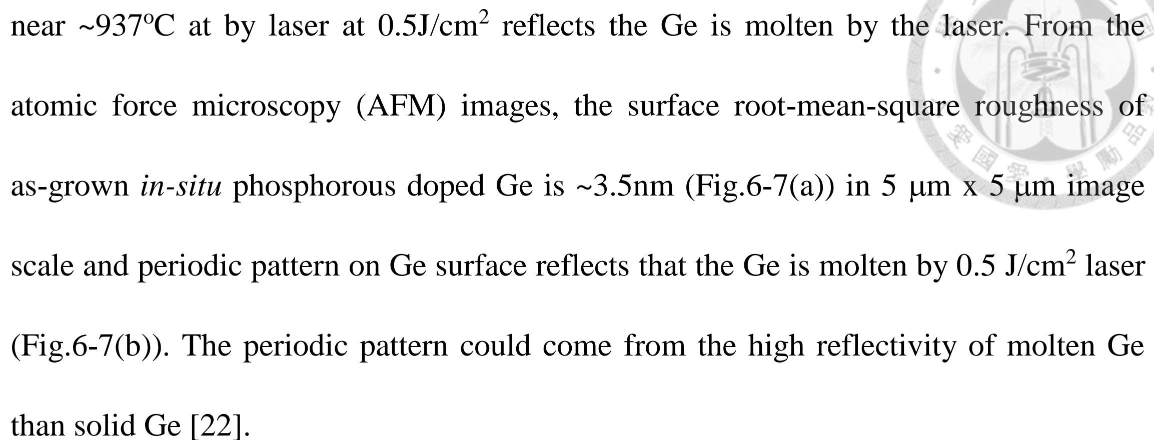

near ~937°C at by laser at 0.5J/cm^2 reflects the Ge is molten by the laser. From the atomic force microscopy (AFM) images, the surface root-mean-square roughness of as-grown *in-situ* phosphorous doped Ge is ~3.5nm (Fig.6-7(a)) in 5 μm x 5 μm image scale and periodic pattern on Ge surface reflects that the Ge is molten by 0.5 J/cm^2 laser (Fig.6-7(b)). The periodic pattern could come from the high reflectivity of molten Ge than solid Ge [22].

The cross-sectional transmission electron microscopy (TEM) in Fig.6-8 (a) shows lots of misfit dislocations and twin defects appear in the as-grown Ge films. These defects in the Ge, like implantation damages, could act as acceptor like defects and compensate n-type doping [2]. These defects could also act as high conductance paths which is the major cause for the leakage current in diodes .While the sample is annealed by laser, twin defects are annihilated and dislocation density is about 7x10^8 cm^{-3} (Fig. 6-8(b)). By laser annealing, Ge can be molten, which is discovered using AFM, and recrystallize defects in Ge to enhance the doping activation [23].

Higher laser annealing power could make the pealing of the capping oxide layer and the electron hall concentration saturation or even degradation is found.

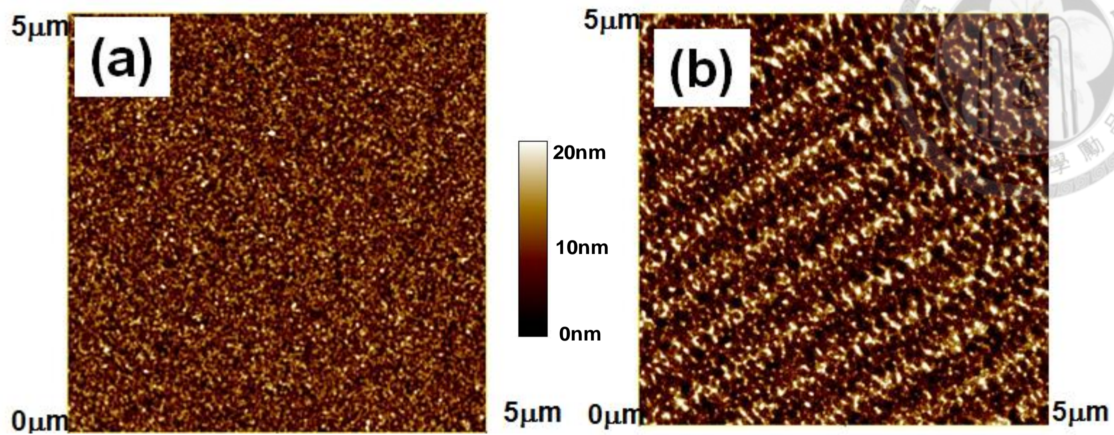

Fig.6-7 AFM images of the *in-situ* phosphorous doped Ge (a) without and (b) with the 0.5J/cm^2 laser annealing. The periodic pattern shown in (b) reflects the Ge melting.

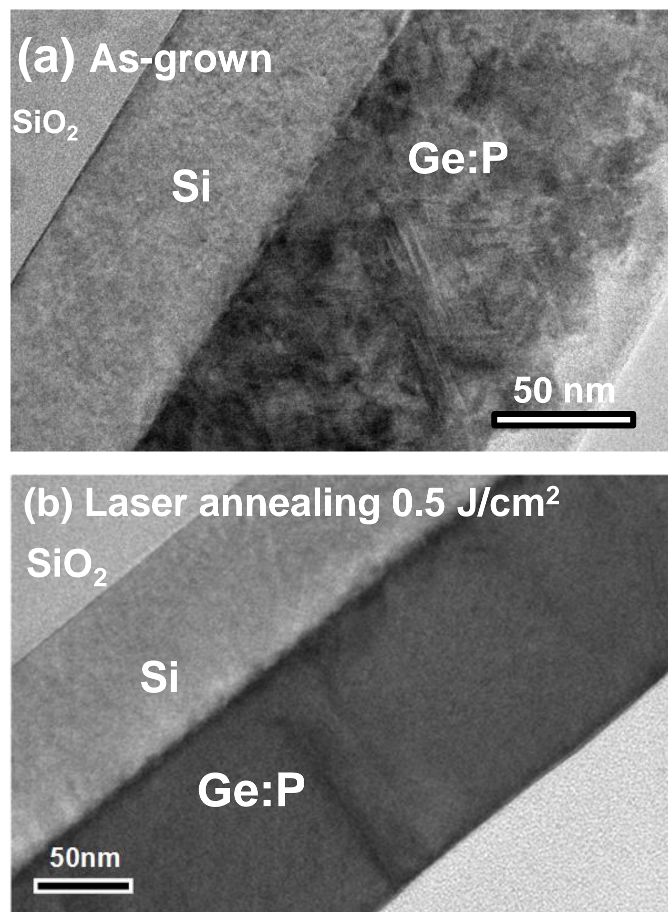

Fig.6-8 The cross section TEM images of the *in-situ* phosphorous doped Ge (a) without and (b) with the 0.5J/cm^2 laser annealing. Note the twin defects in the as-grown TEM images disappeared by laser.

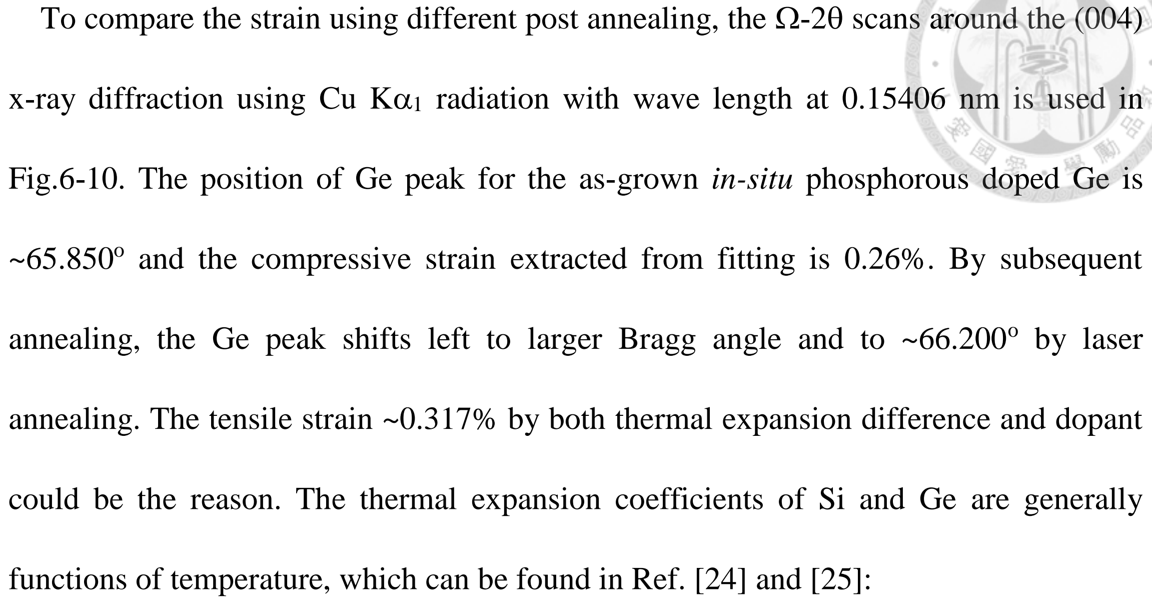

To compare the strain using different post annealing, the Ω-2θ scans around the (004) x-ray diffraction using Cu Kα_1 radiation with wave length at 0.15406 nm is used in Fig.6-10. The position of Ge peak for the as-grown *in-situ* phosphorous doped Ge is ~65.850^o and the compressive strain extracted from fitting is 0.26%. By subsequent annealing, the Ge peak shifts left to larger Bragg angle and to ~66.200^o by laser annealing. The tensile strain ~0.317% by both thermal expansion difference and dopant could be the reason. The thermal expansion coefficients of Si and Ge are generally functions of temperature, which can be found in Ref. [24] and [25]:

$$\alpha_{Si}(T)=3.725x10^{-6}x[1-exp(-5.88x10^{-3}x(T+149.5))]+5.548x10^{-10}T(^oC^{-1})$$

$$\alpha_{Ge}(T)=6.050x10^{6}+3.60x10^{9}T-0.35x10^{-12}T^{2}(^oC^{-1}) \quad (6.1)$$

By the post-growth laser annealing, the Ge film is relaxed and recrystallized at the Ge melting point at 937°C and the theoretical tensile strain at ~0.355% formed at room temperature is expected. Phosphorous incorporation can decrease the Ge lattice constant and reduce the relatively tensile strain [26]. Including the dopant concentration at $2x10^{20}$ cm^{-3} and the estimated tensile strain from thermal expansion effect is 0.317%.

Besides, the scattering of x-ray can result broaden of the Bragg peak, the full-width-at-half-maximum (FWHM) of Ge (004) peak extracted by omega scan is used to analyze the Ge crystalline (Fig. 6-11). The FWHM of the as-grown sample is 0.881^o and is dramatically reduced by *in-situ* anneal and RTA to 0.217^o and 0.224^o, respectively. By laser annealing at 0.5J/cm^2, the FWHM at ~0.140^o indicates the best

crystalline of Ge by laser than the as-grown Ge and that with other annealing. Not only tensile strain but also best crystalline quality of *in-situ* phosphorous Ge is improved by post laser annealing.

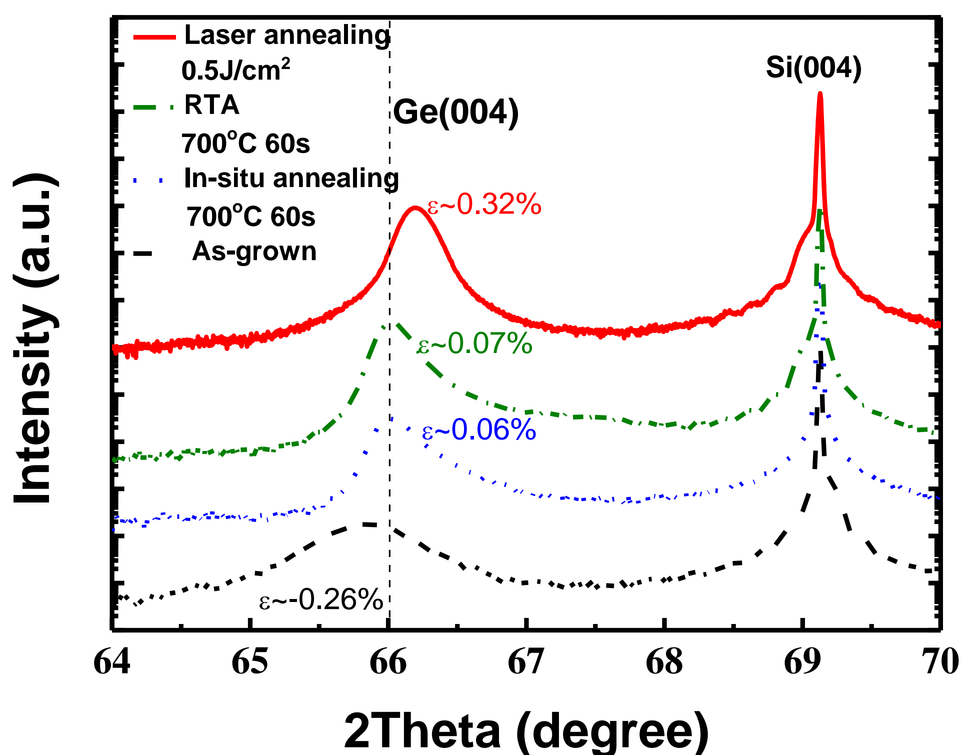

Fig.6-9 The XRD spectroscopy of *in-situ* phosphorous doped Ge received *in-situ* annealing in H_2, RTA in N_2 and laser in ambient. Note that the Ge(004) peak shift to larger Bragger angle reflect the induced tensile strain by laser annealing.

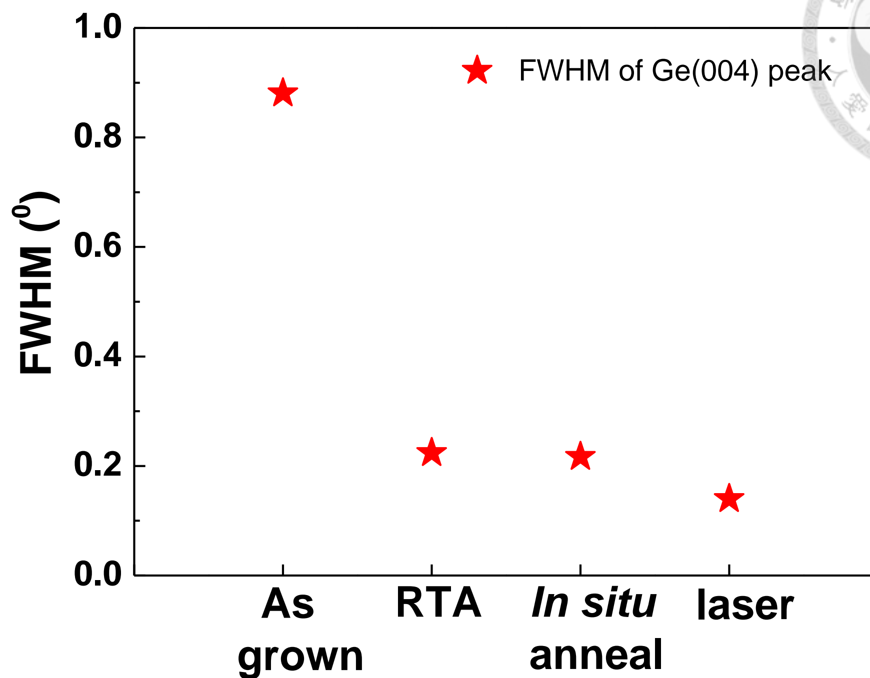

Fig.6-10 The FWHM of Ge (004) Bragg peak by omega scan of *in-situ* phosphorous doped Ge received *in-situ* annealing in H_2, RTA in N_2 and laser in ambient. Note that the FWHM decreases with annealing and reduces mostly by laser.

The SIMS profiles comparing with the SRP of the *in-situ* phosphorous doped Ge with laser annealing is shown in Fig.6-11. For the as-grown sample, only ~2.5×10^{18} with the activation level at ~1% can have (Fig. 6-14). High carrier concentration at 2×10^{20} cm^{-3} with the activation level at 100% is achieved by $0.5 J/cm^2$ laser annealing (Fig. 6-12). Twin annihilation and dislocation reduction by laser annealing, which is found in the Fig.6-8(b), is the main reason for high activation of *in-situ* phosphorous doped Ge. Note the activation of phosphorous near the Ge/Si interface is also improved by laser.

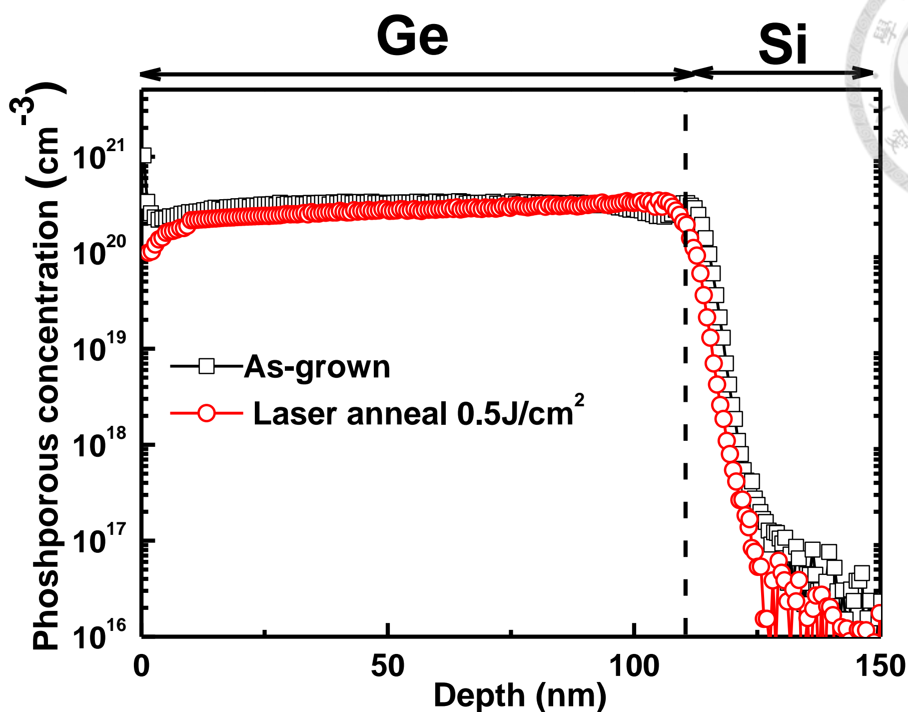

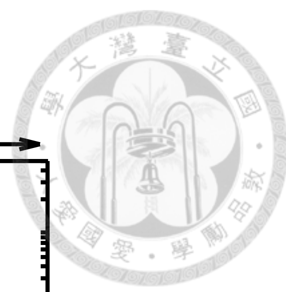

Fig.6-11 The SIMS depth profiles of the *in-situ* phosphorous doped Ge received laser in ambient. Note there is no phosphorous loss/diffusion happened by laser.

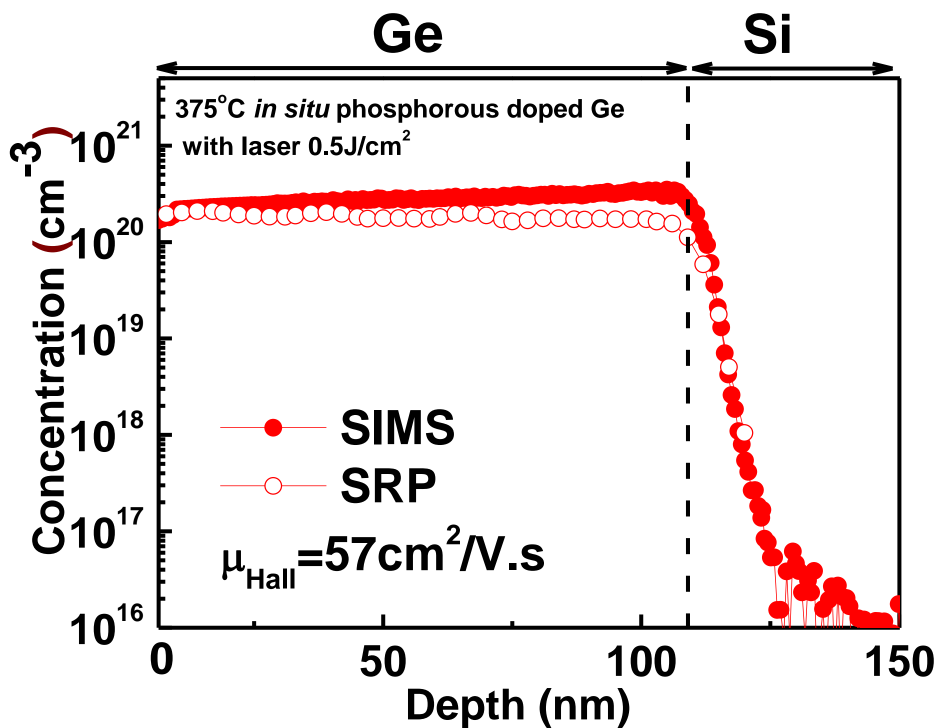

Fig.6-12 The SIMS and SRP depth profile of *in-situ* phosphorous doped Ge received laser annealing 0.5J/cm^2.

The conductivity as a function of the electron hall concentration for n-type Ge bulk comparing to *in-situ* phosphorous doped Ge with different anneals, including *in-situ* annealing in H_2, RTA in N_2 and laser in ambient is shown in Fig.6-13. It is found that the conductivity of phosphorous doped Ge can be improved mostly by laser annealing. When *in-situ* phosphorous doped Ge is annealed by 0.5J/cm^2 laser, the electron Hall concentration of ~2x10^{20} cm^{-3} with the conductivity of 2121 /Ω.cm can achieve. The J-V characteristic of n$^+$/p diode with *in-situ* phosphorous doped Ge annealed by laser with the energy density from 0.3 J/cm^2 ~0.5J/cm^2 is shown in Fig. 6-14. Reduction in off current for the diode is observed as increasing laser energy density. The reduction of as-grown defects by laser leading to smaller generation current contributes to ~10^3 leakage current lowering. By the 0.5J/cm^2 laser, the diode characteristics having a 1x10^6 on/off ratio and a low reverse current density (2x10^{-5} A/cm^2 at 1.5V). The ideality factor estimated from the forward current in the n$^+$/p diode with laser annealing is ~1.3.

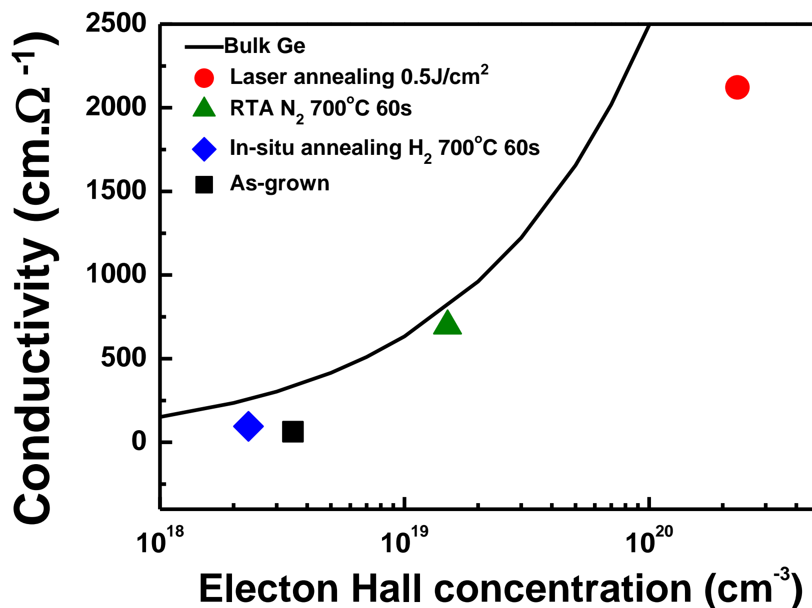

Fig.6-13 The conductivity as a function of the electron hall concentration by the van der pawu measurement. Note that the conductivity and electron hall concentration are improved mostly by laser annealing.

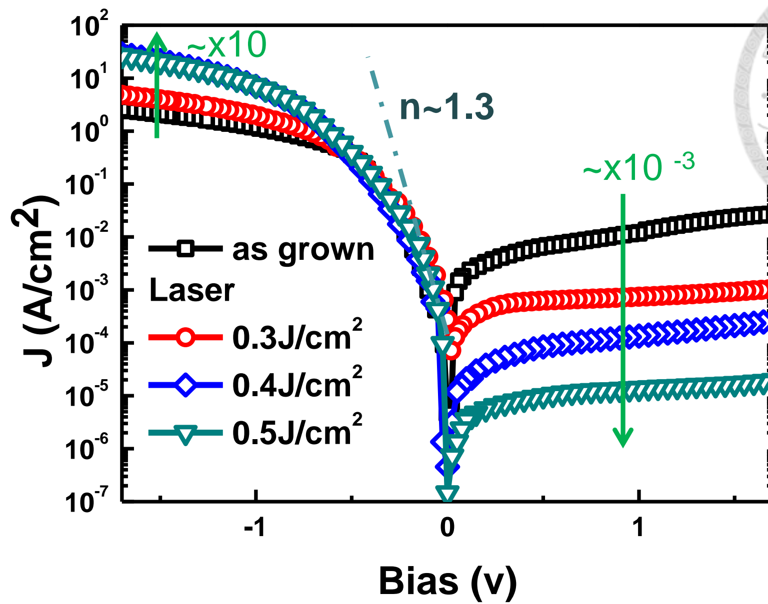

Fig.6-14 Junction currents density of n^+/p diodes using *in situ* phosphorous doping and laser annealing with energy density of 0.3J/cm^2 to 0.5J/cm^2.

6.6 Summary

In the summary, high carrier concentration of *in-situ* doped Ge can have by RTCVD and proper post annealing. For p-type Ge, 3x10^{20}cm^{-3} with the conductivity at 936 cm/Ω can have using *in-situ* annealing. For n-type Ge, 2x10^{20}cm^{-3} with the conductivity at 2121 cm/Ω can have using laser annealing. To eliminate the desorption of boron or phosphorous, the low growth temperature during *in-situ* doping leads to high chemical concentration and post annealing to activate the dopants. For n-type dopant with larger diffusivity than p-type dopant [27], laser annealing with nanosecond duration instead of *in-situ* annealing. Nearly 100% carrier activation along with small dopant lost can achieve by laser. Defective region with twin defects and misfit dislocations in the epitaxial Ge removed by laser annealing is the figures of merits of 2x10^{20}cm^{-3} n-type carrier concentration. The *in-situ* doped Ge with laser annealing is potential for high carrier concentration n^+Ge integrated with Si process.

Reference

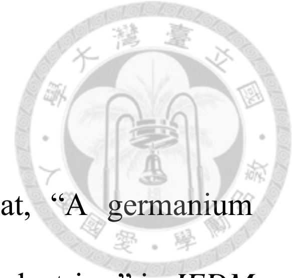

[1] C. O. Chui, H. Kim, P. C. McIntyre, and K. C. Saraswat, “A germanium NMOSFET process integrating metal gate and improved hi-*κ* dielectrics,” in *IEDM Tech. Dig.*, 2003, pp. 18.3.1–18.3.4.

[2] J. Kim, S. W. Bedell, and D. K. Sadana, *Appl. Phys. Lett.*, **98**, 082112 (2011).

[3] C. O. Chui, K. Gopalakrishnan, P. B. Griffin, J. D. Plummer, and K. C. Sarawat, *Appl. Phys. Lett.*, **83,** 3275 (2003).

[4] C. O. Chui, L. Kulig, J. Moran, W. Tsai, and K. C. Saraswat, *Appl. Phys. Lett.*, **87**, 091 (2005).

[5] V. P. Markevich, I. D. Hawkins, and A. R. Peaker, *Phys. Rev. B*, **70**, 213 (2004).

[6] J. M. Hartmann, L. Clavelier, C. Jahan, P. Holliger, G. Rolland, T. Billon, and C. Defranoux, *J. Cryst. Growth*, vol. 264, no. 1–3, pp. 36–47, Mar. 2004.

[7] J. M. Hartmann, J.-F. Damlencourt, Y. Bogumilowicz, P. Holliger, G. Rolland, and T. Billon, *J. Cryst. Growth*, vol. 274, no. 1/2, pp. 90–99, Jan. 2005.

[8] J. Wilhelm, W. Wegscheider, and G. Abstreiter, *Surf. Sci.*, vol. 267, no. 1–3, pp. 90–93, 1992.

[9] G. Scappucci, G. Capellini,W. C. T. Lee, andM. Y. Simmons, *Appl. Phys. Lett.*, vol. 94, no. 16, p. 162 106, Apr. 2009.

[10] G. D. Dilliway, R. van den Boom, B. van Daele, F. E. Leys, T. Clarysse, B. Parmentier, A. Moussa, C. Defranoux, A. Benedetti, O. Richard, H. Bender, E.

Simoen, and M. Meuris, *ECS Trans.*, vol. 3, no. 7, p. 599, 2006.

[11] H. Kim, J.E. Greene, J. Vac. Sci. Technol. A 17 354, (1999).

[12] Jaewoo Shim, I. Song, W.-S. Jung, J. Nam, J. W. Leem, J. S. Yu, D. E. Kim, W. J. Cho, Y. S. Kim,D.-H. Jun, J. Heo, W. Park, Jin-Hong Park, and K. C. Saraswat, *IEEE Electron Device Lett.,* **34**, 15 (2013).

[13] J.M. Hartmann, J.-F. Damlencourt, Y. Bogumilowicz, P. Holliger, G. Rolland, T. Billon, “Reduced pressure-chemical vapor deposition of intrinsic and_doped Ge layers on Si(0 0 1) for microelectronics and_optoelectronics purposes”, *J. Cryst. Growth*, 274, 90–99, (2005).

[14] D. Grüutzmacher, *J. Cryst. Growth*, vol. 182, pp. 53, 1997.

[15] M. L. Yu, D. J. Vitkavage, and B. S. Meyerson, J. Appl. Phys. 59, 4032{4037 (1986).

[16] S.M. Jang, K. Liao, R. Reif, *Appl. Phys. Lett.* **63**, 1675 (1993).

[17] M. Yang, M. Carroll, J.C. Sturm, T. Bűyűklimanli, *J. Electrochem. Soc.* **147**,_3541 (2000).

[18] G.D. Dilliway, R. van den Boom, B. van Daele, F.E. Leys, T. Clarysse, B. Parmentier, A. Moussa, C. Defranoux, A. Benedetti, O. Richard, H. Bender, E. Simoen, M. Meuris, ECS Transactions, 3 (7) 599-609 (2006)

[19] M. Servidori, S. Solmi, P. Zaumseil, U. Winter, and M. Anderle, *J. Appl. Phys.*, **65**,

98 (1989).

[20] D. B. Cuttriss, *Bell Syst. Tech. J.*, **40**, 509 (1961).

[21] P. Baeri, S. U. Campisano, G. Foti, and E. Rimini, J. Appl. Phys. 50(2), (1979).

[22] J. S. Preston, H. M. van Driel, and J. E. Sipe, *Phys. Rev. Lett*, **58**, 69 (1987).

[23] P. Tsouroutas, D. Tsoukalas, A. Florakis, I. Zergioti, A.A. Serafetinides, N. Cherkashin, B. Marty, and A. Claverie, Materials Science in Semiconductor Processing **9** 644 (2006).

[24] H. P. Singh, Acta Crystallogr., Sect. A: Cryst. Phys., Diffr., Theor. Gen. Crystallogr. 24, 469~471 (1968).

[25] Y. Okada and Y. Tokumaru, J. Appl. Phys. 56, 314 (1984).

[26] T. H. Yeh and M. L. Joshi, *J. Electrochem. Soc.:* SOLID STATE SCIENCE,74 (1969)

[27] A. Chroneos and H. Bracht, *Appl. Phys. Lett.*, **1**, 011301 (2014).

Chapter 7

Summary and Future Work

7.1 Summary

In this dissertation, the Ge and Si growth and dopant incorporation are studied in the previous experiments. Using ultra-high vacuum chemical vapor depositon (UHV/CVD) system, the Ge surface diffusion and segregation behavior in different ambient has been investigated. Take the advantage of low surface contamination in UHVCVD system, the solid phase doping layer has been grown for dopant source of Ge. To develop advanced device applications with scaling cost, ASM Episilon 2000 rapid thermal chemical vapor deposition (RTCVD) have also been used to have higher SiGe and Ge growth rate and dopant incoporation.

The growth mechanism of Ge(Si) nanoring, which indicates the Ge out-diffusion, was discussed in different growth and *in-situ* annealing conditions. Capping layer using SiH_4/H_2 cannot cover the whole dots and leads Ge out-diffusion easier than its using SiH_4/He. Besides, the *in-situ* annealing in vacuum or in He instead of with H_2 is also essential to make Ge out-diffusion. Hydrogen passivation is the crucial role to reduce capping layer growth and Ge out-diffusion. For the SiGe p-type channel metal oxide semiconductor field effect transistors, the methods to avoid Ge out-diffusion by capping layer and annealing in H_2 can prohibit Ge out-diffusion and good for gate oxide deposition.

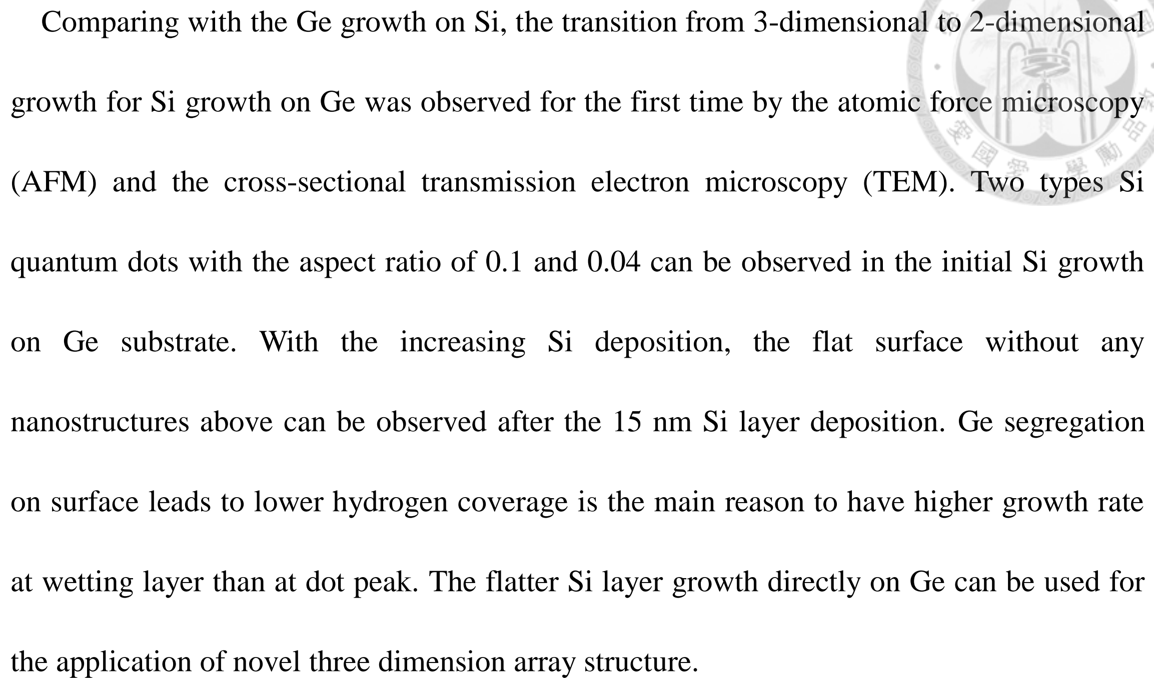

Comparing with the Ge growth on Si, the transition from 3-dimensional to 2-dimensional growth for Si growth on Ge was observed for the first time by the atomic force microscopy (AFM) and the cross-sectional transmission electron microscopy (TEM). Two types Si quantum dots with the aspect ratio of 0.1 and 0.04 can be observed in the initial Si growth on Ge substrate. With the increasing Si deposition, the flat surface without any nanostructures above can be observed after the 15 nm Si layer deposition. Ge segregation on surface leads to lower hydrogen coverage is the main reason to have higher growth rate at wetting layer than at dot peak. The flatter Si layer growth directly on Ge can be used for the application of novel three dimension array structure.

Using the previous experience, it is found that the growth rate enhanced could be enhanced by the hydrogen coverage and precursor adsorption. $Si_{1-x}Ge_x$ film with x~0.5 can have using dichlorosilane (DCS) and germane (GeH_4). With increasing Ge incorporation, which leads to hydrogen desorption easier, growth rate can be enhanced simultaneously. However, nitrogen instead of hydrogen can not enhance the SiGe using DCS/GeH_4 due to the harder Si adsorbed with less $SiCl_2$* desorption in less hydrogen ambient. SiGe using silane (SiH_4) and GeH_4 can enhance the growth rate using nitrogen instead of hydrogen. Besides, Ge directly growth on Si with the threading dislocation pits density growth ~2.7×10^6 cm^{-2} has been demonstrated. From its photoluminescence, the existing defects in the Ge film leads to larger direct band transition to indirect transition. Moreover, nitrogen instead of hydrogen can also enhance the Ge growth rate.

Dopant incoporation by solid phase deposition on epitaxial Ge on Si with low threading dislocation has been demonstrated. To avoid the implantation damage, which

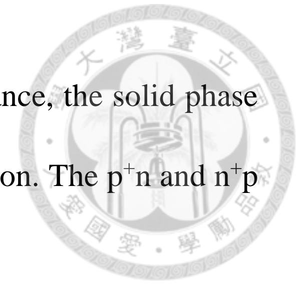

can compensate the n-type dopants and degrade the diode performance, the solid phase doping is one of method to have implantation damage free Ge junction. The p^+n and n^+p diodes with on/off ratio at ~10^5 with the Ioff ~$x10^{-5}$ A/cm^2 can have.

To have shallow and abrupt junction with lower thermal budget, the *in-situ* doped Ge is developed. Low growth temperature to eliminate the boron or phosphorous desorption. The post *in-situ* annealing and laser annealing is used to activate the incorporate dopants. $3x10^{20}cm^{-3}$ p-type Ge with the conductivity at 936 cm/Ω can and $2x10^{20}$ cm^{-3} n-type Ge with the conductivity at 2121 cm/Ω can reach by *in-situ* doping and proper post annealing. Laser annealing with nanosection duration can reduce the dopant loss/diffusion is the crucial role to have high n-type concentration Ge.

7.2 Future Work

To face the more than Moore's law, the material with better transport properties and higher carrier mobility is the key components of future ultra-scale transistor. SiGe has been used in p-type channel metal oxide semiconductor field effect transistors and stressor induced compressive strain. Ge, with is compromise with Si process, has also been the most promising solution. Higher dopant incorporation with adequately growth rate is needed for industry. Higher order silane precursors, like Si_2H_6, and Si_3H_8, allowing Si growth at very low temperatures (down to 350℃). Concerning germanium, growth temperatures as low as 350℃ is already achievable with GeH_4. However, even lower temperatures are necessary for various Ge growth processes of interest. Therefore, digermane (Ge_2H_6) has been recently suggested as low temperature precursor. The lowest possible Ge growth temperature (275℃) using Ge_2H_6 as precursor is promising

in the future research.

Other promising study using GeSn as channel material having high hole mobility is needed for novel transistor. Low Sn solubility (<1%) in the Ge matrix and the instability of Sn precursor make it difficult to study. Take the advantage of using a stable $SnCl_4$ liquid source and lower growth temperature using Ge_2H_6, GeSn using $SnCl_4$ as the Sn precursor and Ge_2H_6 as the Ge source to realize a high quality GeSn epilayer for high mobility GeSn three-dimensional and ultra-thin body devices will be fabricated.

To realize Ge n-type channel transistor, the gate stack preparations, and the source/drain pn junction tuning with proper thermal budget is needed. Dopant incorporation using B_2H_6 and PH_3 *in-situ* doping has reached high carrier concentration. However, the phosphorous coverage will be saturated and limit the incoporation. Novel precursor, like $P(GeH_3)_3$ or $As(GeH_3)_3$ could be the promising solution to surpass the adsorption limitation.

All the works we have done are on the blanket wafers. However, all these structures have not been grown on the patterned wafers yet. The selectively epitaxial growth can localize the SiGe nanostructures, and more physics can be investigated. We have discussed the growth mechanism of the Si and Ge, and this can help us for all other kinds of epitaxial structure in the future. With all these further researches effort, the Ge epitaxial growth can be much more potential the Ge MOSFET technology is expected to realize in sub-10 nm node.